

# Electric-field control of magnetism in multiferroic composites

Ding, Hui

2015

Ding, H. (2015). Electric-field control of magnetism in multiferroic composites. Doctoral thesis, Nanyang Technological University, Singapore.

<https://hdl.handle.net/10356/65405>

<https://doi.org/10.32657/10356/65405>



**ELECTRIC-FIELD CONTROL OF MAGNETISM IN  
MULTIFERROIC COMPOSITES**

**DING HUI**

**SCHOOL OF MATERIALS SCIENCE & ENGINEERING**

**2015**

# **ELECTRIC-FIELD CONTROL OF MAGNETISM IN MULTIFERROIC COMPOSITES**

**DING HUI**

School of Materials Science & Engineering

A thesis submitted to the Nanyang Technological University  
in partial fulfillment of the requirement for the degree of  
Doctor of Philosophy

**2015**

## ACKNOWLEDGEMENTS

The author wishes to express her most sincere appreciation to Associate Professor Thirumany Sritharan and Associate Professor Wang Junling for their patience, guidance and recommendation during the course of this project. The insights gained from those discussions helped to achieve greater understanding of the aim of this investigation.

Special thanks to Dr. Long Yi and Prof. Wang's group members, Dr. You Lu, Dr. Ong Hock Guan, Dr. Chen Weigang, Dr. Chua Ngeah Theng, Dr Yang Pang, Dr Qi Yajun, Dr. Zou Xi, and especially Dr. Cheah Jun Wei Jason for their valuable suggestions. Also, without their constant encouragement, this path would not have been possible.

Her sincere gratitude to all staff of Nanomaterials, Ceramic and Polymer Laboratory (NTU) for their patient teaching, technical support and other forms of help in one way or another. With their guidance, expertise and help, this investigation was successfully carried out.

Last but importantly, the author would like to thank her immediate family members, Dad and Mum, Husband (Dr. Cheah Jun Wei Jason), parents-in-law, daughter (Ms. Candice Cheah), for all their generous spiritual support and also the financial support. Without their encouragement, sacrifice and help rendered during this long and tedious path, the author will not be where she is today.

The author also acknowledges the support from Nanyang Technological University and Ministry of Education of Singapore under project number AcRF RG30/06 and ARC 16/08.

# ABSTRACT

Multiferroic materials have at least two of the ferroic properties, namely ferroelectricity, ferro (antiferro) magnetism and ferroelasticity. The term usually refers to materials that possess both ferroelectric and magnetic orders. An interesting and important consequence of the coexistence of multiple orders is the possible coupling between them, which is named magnetoelectric coupling. It implies that the magnetization could be modulated by an electric field and vice versa. We aim to understand the magnetoelectric coupling phenomenon in multiferroic composite systems in this project.

Single-phase multiferroic materials are scarce in nature. However, by combining ferroelectric and ferro (ferri) magnetic materials together, we could design composites with multiferroic properties with much more flexibility. In such a composite, magnetoelectric coupling is achieved through interface-mediated strain effect. There are different ways to combine ferroic phases to form composites. In this project, we focus our effort on the two types of composite systems that would exhibit minimal clamping effect, such as the bulk composites and a magnetic film on a piezoelectric substrate.

First, the bulk composites consisting barium titanate ( $\text{BaTiO}_3$ ) and cobalt ferrite ( $\text{CoFe}_2\text{O}_4$ ) were synthesized using conventional and spark plasma sintering (SPS) techniques. Dense  $\text{BaTiO}_3$ - $\text{CoFe}_2\text{O}_4$  ceramics were obtained at high temperatures in both cases. SPS has the advantage of producing samples with higher density without any secondary phases. Ferroelectric and magnetic properties of the bulk composites were investigated which shows

enhanced properties as density of the composite increased. Unfortunately, due to the high leakage current and the small magnetoelectric coupling effect in bulk ceramics, we were not able to achieve electric-field control of magnetism.

Subsequently, we investigated a composite where a magnetic film was deposited on a piezoelectric substrate, which had a well-defined, high-quality interface between the two phases, and was totally free of substrate clamping effect. . Magnetic  $\text{CoFe}_2\text{O}_4$  films were deposited on piezoelectric  $\text{Pb}(\text{Mg}_{1/3}\text{Nb}_{2/3})\text{O}_3\text{-PbTiO}_3$  (PMN-PT) single crystal substrates by pulsed laser deposition. Using an active piezoelectric substrate not only eliminates the clamping effect which is prevalent in the conventional composite film systems on passive substrates, but also facilitates effective strain coupling at the interface. Accurate crystal structure investigation confirms the strain transfer between the PMN-PT substrate and the  $\text{CoFe}_2\text{O}_4$  film. When an electric field was applied to the PMN-PT substrate, the magnetic response of the  $\text{CoFe}_2\text{O}_4$  film clearly altered as revealed by both their magnetic hysteresis loops and domain structures. The demonstrates magnetoelectric coupling between the substrate and the film, which can be explained using a strain transfer model.

Our work has provided experimental evidence for the strain mediated magnetoelectric coupling in this composites where a magnetic  $\text{CoFe}_2\text{O}_4$  film is on a ferroelectric substrate and offer valuable information for their potential applications.

## List of Figures

Figure 1.1: A schematic diagram showing material properties with various magnetic and electric properties. Note the partial overlap of magnetoelectric zone with multiferroic zone. <sup>2</sup>	2
Figure 1.2: The interrelationship between electrical, magnetic and strain phenomenon in materials. <sup>3</sup>	3
Figure 1.3: Two types of epitaxial thin film composites. (A) and (B) Superlattice structure of a spinel (top) and a perovskite (middle) on a perovskite substrate (bottom). (C) Epitaxial alignment of a spinel (top left) and a perovskite (top right) on a perovskite substrate (bottom). (D) A self-assembled nanostructure thin film formed on the substrate. <sup>12</sup>	7
Figure 1.4: Dependence of magnetization on temperature for (a) the 1-3 type composite film (top red) and (b) 2-2 type multilayer film (bottom black). <sup>18</sup>	10
Figure 1.5: Schematics of the perovskite-spinel nanostructures on (100) and (111) oriented substrates: (a) Winter bottom construction. $\Delta\gamma$ is the wetting strength. $\gamma_2$ is the surface energy for the epitaxial phase. (b) Equilibrium shapes of the perovskite and spinel phases; and Self-assembled perovskite-spinel thin film on (c) (001) and (d) (111) substrate surface. <sup>21</sup>	11
Figure 2.1: Schematic of the spark plasma sintering system: A: Punch Electrode, B: Punch, C: Sample, D: Graphite Die, E: Vacuum and Water Cooling Chamber, F: Optical pyrometer. <sup>29</sup>	17
Figure 2.2: Schematic diagram of a pulsed laser deposition system.	18



Figure 2.3: The schematic diagram showing how the $\theta$ -2 $\theta$ scanning works. ....	21
Figure 2.4: Geometry of the reciprocal space mapping measurement. ....	23
Figure 2.5: The two basic operation modes of a TEM: diffraction mode (left) and imaging mode (right). <sup>34</sup> .....	25
Figure 2.6: A typical ferroelectric hysteresis loop. Ps: spontaneous polarization; Pr: remanent polarization; Ec: coercive field. <sup>35</sup> .....	27
Figure 2.7: Schematic of the typical butterfly Stain-Electric field loop. <sup>36</sup> .....	28
Figure 2.8: The schematic diagram of VSM systems. ....	29
Figure 2.9: Various components of an AFM system. ....	31
Figure 3.1: XRD patterns of the as-milled, conventionally sintered, and SPS sintered bulk composites.....	36
Figure 3.2: The composite density vs sintering temperature for both the conventional technique and SPS.....	37
Figure 3.3: SEM micrographs of the surfaces of the composites. (a) and (b) conventionally sintered at 1200 °C, (c) and (d) SPS sintered at 1000 °C near the surface, (e) and (f) SPS sintered at 1000 °C at the center.....	39
Figure 3.4: (a) Backscattered electrons image of the sample conventionally sintered at 1200°C with three zones of contrasts. (b) EDS spectrum at point 001 with the brightest contrast, (c) EDS spectrum point 002 with intermediate gray contrast. (d) EDS spectrum at point 003 with the darkest contrast, .....	41
Figure 3.5: The typical Hysteresis loops of composites that are (a) before and after sintering, (b) synthesized in different techniques, and (c) SPS in different temperature. ....	44

Figure 3.6: AFM topography and MFM images of the BaTiO <sub>3</sub> -CoFe <sub>2</sub> O <sub>4</sub> composites: (a) shows typical topography of the polished surface. (b) and (c) are MFM phase images of the SPS produced and conventionally sintered samples, respectively; Bright and dark contrasts in these MFM images indicate up and down magnetization directions at the respective locations in these samples. ....	47
Figure 3.7: Ferroelectric hysteresis loops of the samples which are (a) conventionally sintered at 1200°C and (b) SPS sintered at 1000°C, respectively. ....	49
Figure 4.1: Large and sharp magnetic response due to an applied electric field. Each data sweep was carried out in 20 Oe, after an excursion in 8,000 Oe from 470 K, to 70 K, to the measurement temperature. The electric field was manually ramped over a period of approx10 s while visually monitoring the VSM output in real time. The films were biased positive relative to the substrates, but reverse bias was used for sample 5 at 157 K. Transitions were recorded at 4 kV cm <sup>-1</sup> (sample 3), 10 kV cm <sup>-1</sup> (sample 4) and 6 kV cm <sup>-1</sup> (sample 5 at both 89 K and 157 K). <sup>51</sup> .....	54
Figure 4.2: (a) Scheme of the sample and experimental configuration. (b) In-plane magnetic hysteresis loops under electric fields of +8 kVcm <sup>-1</sup> (circle) and -8 kVcm <sup>-1</sup> (square). (c) Electric-field tuning of the in-plane magnetization (square) and polarization current (open circle) recorded at the same time. (d) The repeatable high/low magnetization states (open circle) switched by pulsed electric fields (blue line). <sup>57</sup> .....	56
Figure 4.3: (a) Magnetic hysteresis loops measured at 290, 270, 200, and 180 K with the external magnetic field applied along BTO (100). (b) Illustration of the different orientations of the external field. In panels (c)–(f), hysteresis loops at specific temperatures for different orientations of the external magnetic field are shown. <sup>24</sup> .....	58

Figure 4.4: Phase diagram of PMN-xPT around the MPB. The solid line indicating the transition to the cubic phase is the average of the two temperatures from dielectric measurements. The symbols separating the <i>MC</i> and <i>T</i> phases represent the temperatures at which the MC-T phase transition begins to take place. <sup>63</sup> .....	60
Figure 4.5: X-ray diffraction pattern of the as-grown CoFe <sub>2</sub> O <sub>4</sub> /PMN-PT heterostructure; the inset is the schematic description of the sample. ....	63
Figure 4.6: Reciprocal space mapping of the epitaxial CoFe <sub>2</sub> O <sub>4</sub> film on (001) - cut PMN-PT substrate around the (202) peak. ....	64
Figure 4.7: (a) Cross-section view TEM image taken from the PMN-PT\CoFe <sub>2</sub> O <sub>4</sub> sample. (b) Selected area diffraction pattern from the same sample. (c) High resolution TEM image of the interface area between the PMN-PT and CoFe <sub>2</sub> O <sub>4</sub> . ....	66
Figure 4.8: Polarization vs. electric field hysteresis loop of the PMN-PT substrate before and after CoFe <sub>2</sub> O <sub>4</sub> deposition. ....	67
Figure 4.9: The strain vs. electric field hysteresis loop of the PMN-PT substrate before and after CoFe <sub>2</sub> O <sub>4</sub> deposition. ....	68
Figure 4.10: The in-plane and out-of-plane magnetization-field hysteresis loops of CoFe <sub>2</sub> O <sub>4</sub> film on PMN-PT. ....	69
Figure 4.11: Schematic description of the experimental setup for plan view MFM imaging of the substrate on heating stage. ....	71
Figure 4.12: (a) and (c) Topography and magnetic domain structures of the CoFe <sub>2</sub> O <sub>4</sub> film before heating treatment, respectively.( b) and (d) The Topography and magnetic domain structures of the CoFe <sub>2</sub> O <sub>4</sub> film at the same location after heat treatment, respectively. ....	72

Figure 4.13: Schematic description of the experimental setup for plan view MFM imaging after various electric fields are applied to the substrate. ....	73
Figure 4.14: (a-e) Topography and magnetic domain structures looking from the x-axis of $\text{CoFe}_2\text{O}_4$ thin film at different states of the ferroelectric switching of the PMN-PT substrate. (a) Initial state; (b) positive remnant state; (c) depolarized state; (d) negative remnant state and (e) depolarized state. (f) The polarization vs. electric field hysteresis loops of the PMN-PT substrate.....	76
Figure 4.15: Schematic description of the experimental setup for cross section view measurements.....	77
Figure 4.16: (a-e) Topography and magnetic domain structures of the cross section surface (z-axis) of $\text{CoFe}_2\text{O}_4$ (The thin film thickness=200 nm) at different states of the ferroelectric switching of the PMN-PT substrate. (a) Initial state; (b) positive remnant state; (c) depolarized state; (d) negative remnant state and (e) depolarized state. (f) The polarization vs. electric field hysteresis loops of the PMN-PT substrate. ....	80
Figure 4.17: (a) Schematic description of the sample orientation. (b-d) The magnetization-field hysteresis loops of the $\text{CoFe}_2\text{O}_4$ film on PMN-PT substrate along the x (b), y (c) and z (d) directions at different polarization states. ....	82
Figure 4.18: (a), (b) and (d) Schematic diagrams of proposed effect when the substrate is at different states along the P-E hysteresis loop. (c) The orientation of the sample with respect to the previous experiments. ....	84

*\*Permission has been sought from the authors for use of their pictures and diagrams.\**

## List of Tables

Table 1. Magnetic Properties of ferrites <sup>42</sup> .....	34
Table 2: Important magnetic data of samples obtained from Figure 3.5 .....	45

# Table of Contents

<b>ACKNOWLEDGEMENTS .....</b>	<b>i</b>
<b>ABSTRACT.....</b>	<b>iii</b>
<b>LIST OF FIGURES .....</b>	<b>v</b>
<b>LIST OF TABLES .....</b>	<b>x</b>
<b>CHAPTER 1 : INTRODUCTION.....</b>	<b>1</b>
1.1 DEFINITION OF MULTIFERROIC MATERIALS.....	1
1.2 COMPOSITES MULTIFERROIC.....	5
1.3 APPLICATION OF MULTIFERROIC MATERIALS .....	13
1.4 SCOPE AND OBJECTIVES .....	14
<b>CHAPTER 2 : EXPERIMENTAL TECHNIQUES .....</b>	<b>16</b>
2.1 COMPOSITE SYNTHESIS .....	16
2.1.1 Spark Plasma Sintering.....	16
2.1.2 Pulsed Laser Deposition.....	18
2.2 STRUCTURAL CHARACTERIZATIONS .....	21
2.2.1 X-Ray Diffraction.....	21
2.2.2 Transmission Electron Microscopy .....	23
2.3 ELECTRICAL MEASUREMENTS .....	26
2.4 MAGNETIC MEASUREMENTS .....	29
2.4.1 Vibration Sample Magnetometer .....	29
2.4.2 Magnetic Force Microscopy.....	30

## **CHAPTER 3 : MULTIFERROIC $\text{BaTiO}_3$ - $\text{CoFe}_2\text{O}_4$ BULK COMPOSITES ..... 32**

3.1 INTRODUCTION.....	32
<i>BaTiO<sub>3</sub> (BTO)</i> .....	33
<i>CoFe<sub>2</sub>O<sub>4</sub> (CFO)</i> .....	34
3.2 COMPOSITE SYNTHESIS .....	35
3.3 PHASE IDENTIFICATION .....	36
3.3 EFFICIENCY OF SINTERING .....	37
3.4 MICROSTRUCTURE .....	38
3.5 MAGNETIC AND FERROELECTRIC PROPERTIES OF THE BULK COMPOSITES .....	42
3.5.1 <i>Magnetic Properties</i> .....	42
3.5.2 <i>Ferroelectric Properties</i> .....	48
3.6 CONCLUSIONS .....	50

## **CHAPTER 4 : MULTIFERROIC THIN FILM COMPOSITES- $\text{CoFe}_2\text{O}_4$ FILM ON $\text{Pb}(\text{Mg}_{1/3}\text{Nb}_{2/3})\text{O}_3$ - $\text{PbTiO}_3$ SINGLE CRYSTAL SUBSTRATE..... 52**

4.1 INTRODUCTION.....	52
<i>Pb(Mg<sub>1/3</sub>Nb<sub>2/3</sub>)O<sub>3</sub>-PbTiO<sub>3</sub> (PMN-PT)</i> .....	59
4.2 GROWTH AND CHARACTERIZATIONS OF THE EPITAXIAL THIN FILMS ON ACTIVE SUBSTRATES .....	61
4.2.1 <i>Experimental Procedure for the Film Growth</i> .....	61
4.2.2 <i>The structure of <math>\text{CoFe}_2\text{O}_4</math> thin film on PMN-PT single crystal substrate</i> .....	62
4.3 ELECTRICAL AND MAGNETIC PROPERTIES OF THE $\text{CoFe}_2\text{O}_4$ /PMN-PT COMPOSITE .....	67
4.3.1 <i>Ferroelectric properties of <math>\text{CoFe}_2\text{O}_4</math> /PMN-PT thin film composite</i> .....	67





4.3.2 Piezoelectric properties of the PMN-PT after $\text{CoFe}_2\text{O}_4$ deposition .....	68
4.3.3 Magnetic properties of the $\text{CoFe}_2\text{O}_4$ /PMN-PT composite.....	69
4. 4 MAGETOELECTRIC COUPLING IN THE $\text{CoFe}_2\text{O}_4$ /PMN-PT COMPOSITE.....	70
4.4.1 Strain effect on the magnetic domains of the composite.....	70
4.4.2 Magetoelectric coupling effect in the composite .....	81
4.4.3 Proposed model of magnetoelectric coupling effect in the composite.....	83
<b>CHAPTER 5 : SUMMARY AND FUTURE WORK .....</b>	<b>85</b>
<b>REFERENCE .....</b>	<b>90</b>

# Chapter 1 : Introduction

## 1.1 Definition of Multiferroic Materials

Multiferroic materials possess at least two of the ‘ferroic’ properties, i.e. ferroelectricity, ferromagnetism and ferroelasticity, simultaneously. In a broader definition, ‘antiferroic’ properties are also considered. Ferroelectricity refers to materials showing spontaneous polarization which can be switched between equivalent states by the application of an external electric field. The spontaneous polarization (electric dipoles) is physically tied to the crystal lattice. Force or temperature can both change the crystal lattice and the strength of the dipole, leading to the so-called piezoelectric and pyroelectric effects<sup>1</sup>. The term ferroelectricity is used in analogy to ferromagnetism, which refers to materials possessing a permanent magnetic moment that is stable and can be switched by an applied magnetic field.

Early studies in this field began with magnetoelectric materials, which are different from multiferroic materials, though there are overlaps. Magnetoelectric materials are magnetically and electrically polarizable. They don’t necessarily possess spontaneous polarization or magnetization. However, there must be coupling between magnetic and electric orders, showing magnetoelectric (ME) coupling effect. According to such definitions, there will be a partial overlap between ‘magnetoelectric’ and ‘multiferroic’ zones, as shown in Figure 1.1<sup>2</sup>.

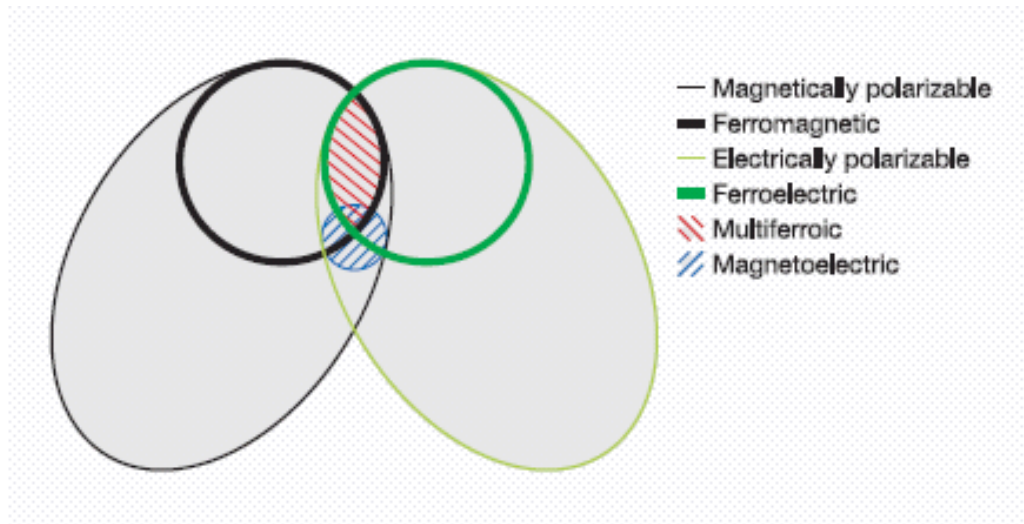


Figure 1.1: A schematic diagram showing material properties with various magnetic and electric properties. Note the partial overlap of magnetoelectric zone with multiferroic zone.<sup>2</sup>

Multiferroic materials may possess the ME coupling effect. Under an external magnetic field, the material will show a corresponding change in electric polarization, or vice versa. Such effect can arise directly between the two order parameters, or indirectly via strain (Figure 1.2)<sup>3</sup>.

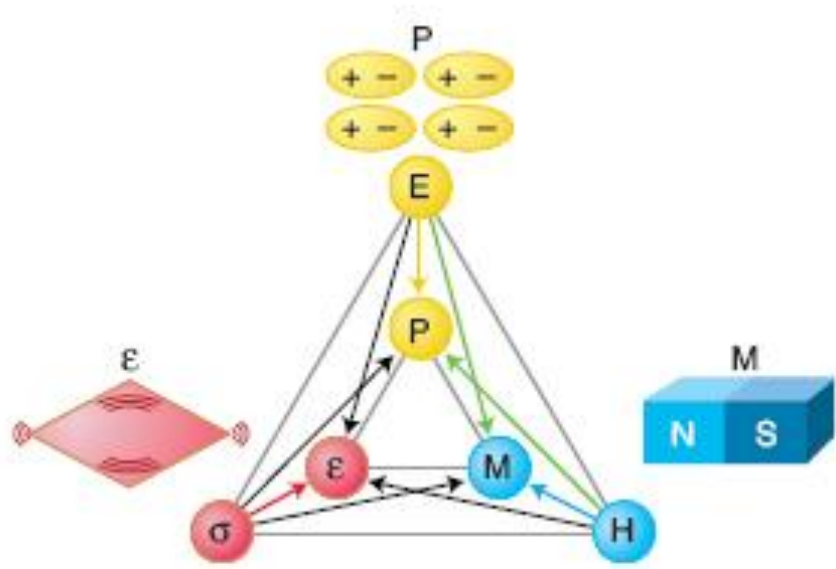


Figure 1.2: The interrelationship between electrical, magnetic and strain phenomenon in materials.<sup>3</sup>

The total free energy of such a material can be expressed as<sup>4</sup>:

$$F(E, H) = F_o - P_i^s E_i - M_i^s H_i - \frac{1}{2} \epsilon_o \epsilon_{ij} E_i E_j - \frac{1}{2} \mu_o \mu_{ij} H_i H_j - \alpha_{ij} E_i H_j - \frac{1}{2} \beta_{ijk} E_i H_j H_k - \frac{1}{2} \gamma_{ijk} H_i E_j E_k \dots$$

Eq1.1

Where E and H stand for the electric and magnetic fields, respectively.  $P^s$  and  $M^s$  denote the spontaneous polarization and magnetization, and  $\epsilon$  and  $\mu$  are the electric and magnetic susceptibilities, respectively. The tensor  $\alpha$  corresponds to the induction of polarization by a magnetic field or magnetization by an electric field which is designated as the linear ME

effect. It is supplemented by higher-order terms like those parameterized by the tensors  $\beta$  and  $\gamma$ . Differentiating the total energy with respect to electric or magnetic field leads to the electrical polarization (P) or the magnetization (M):

$$P_i(E, H) = -\partial F / \partial E_i = P_i^s + \varepsilon_o \varepsilon_{ii} E_j + \alpha_{ij} H_j + \frac{1}{2} \beta_{ijk} H_j H_k + \gamma_{ijk} H_i E_j + \dots \quad \text{Eq1.2}$$

$$M_i(E, H) = -\partial F / \partial H_i = M_i^s + \mu_o \mu_{jj} H_j + \alpha_{ij} E_j + \beta_{ijk} E_i H_j + \frac{1}{2} \gamma_{ijk} E_j E_k + \dots \quad \text{Eq1.3}$$

The ME coefficient is limited by the relation:

$$\alpha_{ij}^2 \leq \varepsilon_o \mu_o \varepsilon_{ii} \mu_{jj} \quad \text{Eq1.4}$$

Where  $\varepsilon_o$  and  $\mu_o$  are the permittivity and the permeability of free space,  $\varepsilon_{ii}$  (T) and  $\mu_{jj}$ (T) are the relative parameters.

A multiferroic material that is simultaneously ferromagnetic and ferroelectric should display a large linear ME coefficient as these materials often possess large permittivity and permeability. Equation 1.4 is obtained by ignoring higher-order coupling terms<sup>2</sup>. In reality, many materials have small values of either  $\varepsilon_{ij}$  or  $\mu_{ij}$  or both, so that the linear ME coefficient is also small as shown by Equation 1.4. Therefore, in order to achieve large ME coefficient through the higher-order terms, materials with reduced dimensionality are suggested, since two-dimensional spin order associated with  $\beta$ (T) can persist to a high temperatures at which three-dimensional spin order associated with  $\alpha$ (T) disappears.<sup>2</sup> However, in two-phase composite materials, where the ME coupling effect is strain mediated, the indirect coupling effect need not to follow Equation 1.4. Therefore, it was predicted that two-phase composite systems may exhibit significantly enhanced ME effect over single-phase systems<sup>5</sup>.

## 1.2 Composites Multiferroic

For practical applications, it would be ideal to combine the ferroelectric and ferromagnetic properties together in one material. However, such single-phase multiferroic materials are very rare.  $\text{BiFeO}_3$  is the only one that is currently well known and studied<sup>6</sup>. In its perovskite-structure, the stereochemical activity of the lone pair electrons of the large (A-site) cation provides the ferroelectricity, while the small (B-site) cation provides magnetic moment<sup>6</sup>. It has good ferroelectric property at room temperature, but net magnetic moment is small due to the intrinsic G-type antiferromagnetic order.  $\text{BiFeO}_3$  thin films show a significant enhancement of magnetization. Thin film  $\text{BiFeO}_3$  usually undergoes transformation from rhombohedra to the lower symmetry monoclinic phase, and enhanced ME effect can be expected qualitatively<sup>6</sup>. However, the intrinsic antiferromagnetic order always limits its potential applications.

Many researchers turn to composite materials to obtain both large ferroelectric polarization and magnetization together as well as enhanced ME coupling effect. There are different ways to prepare bulk and thin film multiferroic composites, for example, solid-state synthesis<sup>7</sup>, vacuum base deposition and sol-gel processing<sup>8</sup>.

The first artificial multiferroic composite was synthesized by unidirectional solidification of the eutectic bulk composite of ferroelectric  $\text{BaTiO}_3$  and magnetic  $\text{CoFe}_2\text{O}_4$ . A high ME coefficient of 130 mV/cm Oe was achieved<sup>9</sup>. This unidirectional solidification requires strict control over the composition, cooling rate and temperature. In comparison, ceramic sintering process is much easier and cheaper to obtain multiferroic composites. It has more freedoms

in the selection of constituent phases and processing parameters and provides the opportunity to introduce a wide range of materials into the composite system. Recently, hot pressing and spark plasma sintering (SPS) techniques have been employed to achieve sufficiently dense bulk composites while avoiding the formation of secondary phases during sintering. Especially, SPS is an efficient sintering method that allows rapid processing (e.g. 5 min) at relatively low temperatures.

Other than the 1-3 composite discussed above, there are other types of bulk composites, such as the 2-2 laminates. The advantage of this type of composites is that the magnetic phase can be insulated to solve the leakage problem. A typical example is the sandwich multiferroic composites PZT/CFO/PZT, which can be prepared via a conventional ceramic sintering process<sup>10</sup>. However, the inter diffusion across the interfaces between different layers during high temperature processing usually reduces the saturation magnetostriction and also alters the properties of the PZT layer. Nan C. et al have also reported a pseudo-1-3-type multiferroic composite prepared by the dice-and-fill technique<sup>11</sup>. It consists of  $\text{Pb}(\text{Zr,Ti})\text{O}_3$  (PZT) rod array (with base) and Terfenol-D/epoxy matrix, and exhibits large ME coefficient of over 300 mV/cm Oe below 40 kHz and over 4500 mV/ cm Oe at resonant frequency.

Compared with bulk composites, nanostructured multiferroic thin films offers some unique advantages, such as (a) significantly enhanced strain transfer due to the reduced dimension; and (b) the possibility of producing compact thin-film magnetoelectric devices. Various methods, such as pulsed laser deposition (PLD), sputtering and spin-coating have been used

to fabricate multiferroic nanocomposite thin films. There are mainly two types of thin film composites that have been reported (shown in Figure 1.3)<sup>12</sup>: the 2-2 heteroepitaxial multilayer system and the 1-3 vertical heterostructures.

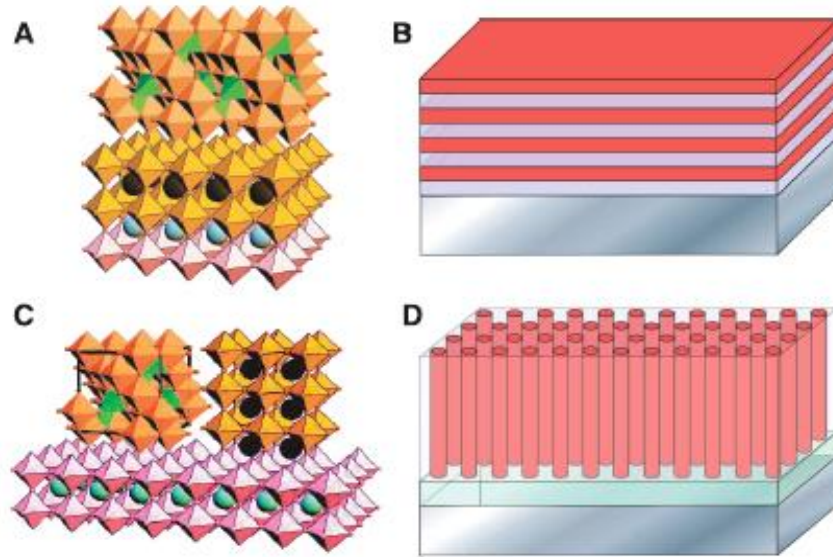


Figure 1.3: Two types of epitaxial thin film composites. (A) and (B) Superlattice structure of a spinel (top) and a perovskite (middle) on a perovskite substrate (bottom). (C) Epitaxial alignment of a spinel (top left) and a perovskite (top right) on a perovskite substrate (bottom). (D) A self-assembled nanostructure thin film formed on the substrate.<sup>12</sup>

Ortega et al have synthesized PZT/CoFe<sub>2</sub>O<sub>4</sub> thin film composites on Pt-coated Si substrate using pulsed laser deposition. The film thickness is ~350 nm<sup>13</sup>. The thin film composites exhibit both magnetic and ferroelectric hysteresis at room temperature. They also confirmed the multiferroic nature of the composite through the reduction of measured ferroelectric polarization with the application of an external magnetic field. More 2-2 type multilayers



composite films were reported subsequently, such as  $\text{NiFe}_2\text{O}_4/\text{BaTiO}_3$  and  $\text{CoFe}_2\text{O}_4/\text{PZT}$  grown on  $\text{SrTiO}_3$  substrate<sup>14,15</sup>.  $\text{BaTiO}_3$  was first epitaxially grown on the  $\text{SrTiO}_3$  substrate as the bottom layer which also acts as a buffer layer between the ferrite and the  $\text{SrTiO}_3$  substrate. It also helps to prevent the leakage problems. The lattice matching assures a coherent epitaxial interface between the layers, which is essential for the strain-mediated ME coupling effect. By replacing  $\text{NiFe}_2\text{O}_4$  with  $\text{CoFe}_2\text{O}_4$  in the ferrite/  $\text{BaTiO}_3$ /  $\text{SrTiO}_3$  heterostructure, a significant enhancement of ME response (from 12.1 out-of-plane and 7.9 mV/cm Oe in-plane to 104 and 66 mV/cm Oe, respectively) was observed<sup>16</sup>. The enhancement was attributed to the smaller constraint strain and larger magnetostriction of the  $\text{CoFe}_2\text{O}_4$ . These ME coefficients are comparable to those reported for the bulk ceramic composites. It was also found that the ME coupling effect also depends on the ordering of each layer<sup>17</sup>. Theoretically, the ferroelectric layer can generate strains of the order of 1% in magnetic layers owing to the structural phase transition. However, in the heterostructure-on-substrate system, both the  $\text{NiFe}_2\text{O}_4$  and  $\text{BaTiO}_3$  suffer a large constraint from the stiff passive substrate. This will restrict the ME coefficient when an external field is applied. Therefore, for 2-2 type thin film composite, many factors including the layer thickness and interfacial roughness will affect the ferroic properties and ME coupling effect.

To eliminate the substrate clamping effect in the 2-2 composites, 1-3 type vertical heterostructures such as the nanopillar embedded in matrix geometry have been developed. They offer numerous advantages over the 2-2 type heterostructures. First, they have a larger interfacial area and are intrinsically heteroepitaxial in three dimensions, which allows for stronger coupling. Secondly, substrate-imposed constraint which could suppress both the

piezoelectric and magnetostrictive effect has less effect in this geometry since the effective interface is vertical.

A typical 1-3 type multiferroic composite thin film consists of a magnetic spinel-phase epitaxially embedded in the ferroelectric matrix. The most well-known example contains  $\text{CoFe}_2\text{O}_4$  pillars in the  $\text{BaTiO}_3$  matrix, which were synthesized using epitaxial self-assembly on single crystal (001)  $\text{SrTiO}_3$  substrates<sup>18</sup>. These films were shown to possess substantial ME coupling effect through the temperature-dependent magnetization measurement as compared to the corresponding 2-2 heterostructures (Figure 1.4). A distinct drop in magnetization was observed at the ferroelectric Curie temperature for the vertically self-assembled nanostructure, whereas the multilayered nanostructure showed negligible change in magnetization. This was attributed to a significantly reduced constrain of the substrate and efficient strain coupling resulting from the nanometer scale of the component phases and coherency of the interfaces. However, the synthesis of these 1-3 type nanocomposite films is not easy. It was reported that the phases in  $\text{CoFe}_2\text{O}_4$  -  $\text{BaTiO}_3$  system cannot be separated at temperatures lower than 700 °C even though they are essentially line compounds in bulk phase diagram, since the formulation of the self-assembly is controlled by both thermodynamic equilibrium and kinetic diffusion<sup>19</sup>.

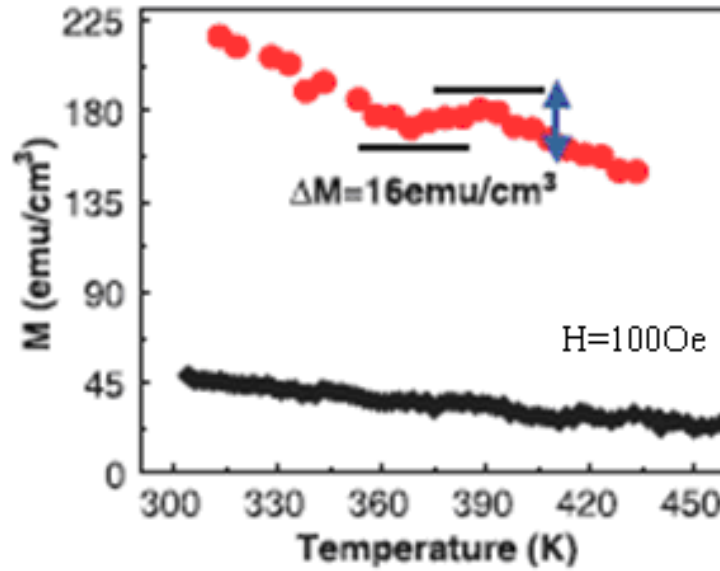


Figure 1.4: Dependence of magnetization on temperature for (a) the 1-3 type composite film (top red) and (b) 2-2 type multilayer film (bottom black).<sup>18</sup>

Similar self-assembled nanostructures have been obtained for  $\text{CoFe}_2\text{O}_4\text{-PbTiO}_3$ <sup>20</sup> and  $\text{CoFe}_2\text{O}_4\text{-BiFeO}_3$  composite films<sup>21</sup>. The  $\text{CoFe}_2\text{O}_4\text{-BiFeO}_3$  system aroused more interest since  $\text{BiFeO}_3$  itself is a single-phase multiferroic material. It has been demonstrated that the substrate orientation controls the morphology of 1-3 composite nanostructures (Figure 1.5). Application of an electric field to a columnar ferroelectric/ferrimagnetic epitaxial nanocomposite could reverse the induced magnetization with the help of a small magnetic field. However, no obvious switching of the ferroelectric polarization was observed upon the application of a magnetic field to the  $\text{CoFe}_2\text{O}_4$  matrix. This was explained as higher strain energy is needed to switch the ferroelectric polarization in  $\text{BiFeO}_3$  nanopillars than the magnetoelastic energy that is available from the  $\text{CoFe}_2\text{O}_4$  matrix. The structure and interface

chemistry of  $\text{BiFeO}_3$  - $\text{NiFe}_2\text{O}_4$  composite thin films were also studied<sup>22</sup>. Rectangular spinel nanopillars were distributed homogeneously in the  $\text{BiFeO}_3$  matrix, with the semicoherent interface lying along the (110) planes. The Bi-Fe-O layer in the  $\text{BiFeO}_3$  matrix was found to bond to the O-Ni-Fe-O layer of the  $\text{NiFe}_2\text{O}_4$  pillars, leading to minimized interface charging and maximized structure continuity across the interface, which should result in strong elastic coupling.

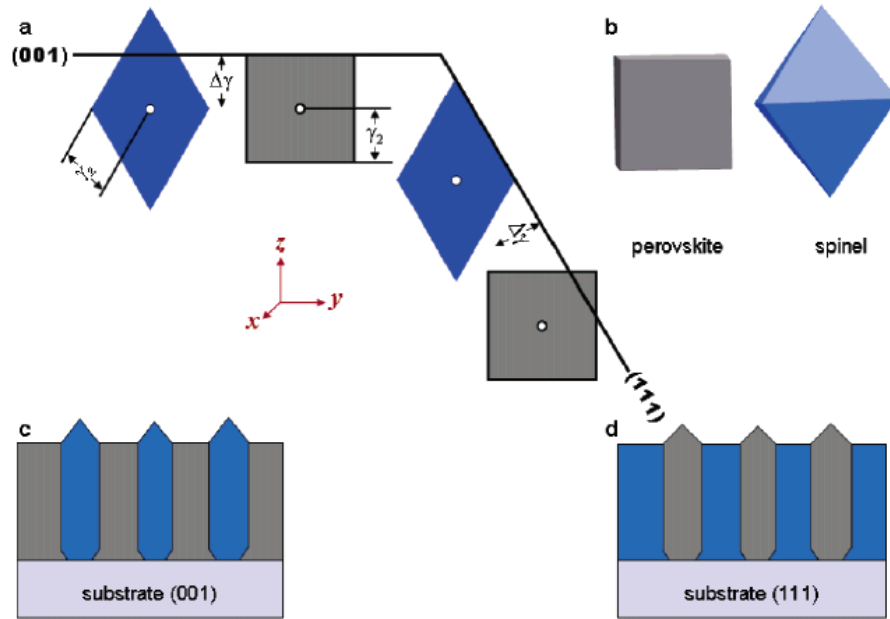


Figure 1.5: Schematics of the perovskite-spinel nanostructures on (100) and (111) oriented substrates: (a) Winter bottom construction.  $\Delta\gamma$  is the wetting strength.  $\gamma_2$  is the surface energy for the epitaxial phase. (b) Equilibrium shapes of the perovskite and spinel phases; and Self-assembled perovskite-spinel thin film on (c) (001) and (d) (111) substrate surface.<sup>21</sup>

The strength of the coupling in nanostructures suggests the key role of heteroepitaxy. However, no controllable switching of the magnetization was observed, unless an additional weak magnetic field was superimposed to lift the symmetry for magnetization. Much research is still needed to understand the nature of the heteroepitaxy as well as the coupling mechanisms in these systems.<sup>23</sup> The formation of self-assembled, vertical nanostructures with long-range ordering will undoubtedly have a great impact on, not only the field of multiferroics, but a broad range of applications.

Besides these two main types of composites, recently a new approach to obtain multiferroic composite with single interface has attracted much attention. It is well known that the in-plane constrain from substrates prevent the 2-2 type multiferroic composites from exhibiting a high ME coupling effect. However, the easy fabrication of such systems is a great advantage. Moreover, in this system, horizontal layers can effectively solve the leakage problem and provide usable ME coupling effect. To eliminate the substrate clamping effect in this system, active piezoelectric substrate has been used recently, on which the magnetic layer is deposited. The substrate materials used are usually the commercially produced single crystals, such as  $\text{BaTiO}_3$ <sup>24</sup>, PZN-PT<sup>25</sup> and PMN-PT<sup>26</sup>. A detailed review on this topic will be provided in Chapter 4.

### **1.3 Application of Multiferroic Materials**

In the past few years, significant progress has been made in the understanding of the fundamental physics of multiferroic and magnetoelectric materials. They have attracted much attention not only because of the rich physics involved but also the potential applications in memory, spintronic devices and other active devices<sup>27</sup>.

It remains an important focus to obtain dense, fast, and nonvolatile random access memories with reduced energy consumption. From the technological perspective, a good approach to achieve this goal is to control and manipulate the magnetism by electric field<sup>28</sup>. Multiferroic materials are among the top candidates for such applications because of the simultaneous ferroelectric and ferromagnetic properties as well as the ME coupling effect they can exhibit. The challenge and opportunity for solid-state physicists is to identify mechanisms that generate large and robust ME coupling effect all at room temperature.

## 1.4 Scope and Objectives

The motivation for our study is the potential application of multiferroic materials and the interest in understanding the fundamental principles behind the magneto-electric coupling in composite systems. Consequently, we choose to examine two different composite systems; one is a zero dimensional system of a bulk composite of BaTiO<sub>3</sub> and CoFe<sub>2</sub>O<sub>4</sub>; and another is a two-dimensional system of a film of CoFe<sub>2</sub>O<sub>4</sub> on a ferroelectric, single crystal PMN-PT substrate. The choice of the active ferroelectric PMN-PT substrate eliminates the substrate constraint inherent in double layers systems on a passive substrate. The objective of this project is to investigate the coexistence of multiple orders and ME coupling effect in these composite systems. If coupling exists, the magnetization could be modulated by an electric field and vice versa opening the possibility of electric-field control of magnetism in electronic devices.

### **The outline of thesis:**

- Chapter 1: Introduction

In this chapter, we will introduce multiferroic materials and review the literature for the state-of-the-art in multiferroic material systems.

- Chapter 2: Experimental Techniques

In this chapter, we will review the experimental techniques used in our work to synthesis, characterize and investigate the materials.

- Chapter 3: Multiferroic BaTiO<sub>3</sub>-CoFe<sub>2</sub>O<sub>4</sub> Bulk Composites

In this chapter, we will describe the synthesis techniques used for the bulk composites:

BaTiO<sub>3</sub>-CoFe<sub>2</sub>O<sub>4</sub>. Two types of synthesis techniques - conventional sintering and spark plasma sintering - are used and compared to study the composites system. The properties of the synthesized products will be presented.

- Chapter 4: Multiferroic Thin Film Composites- CoFe<sub>2</sub>O<sub>4</sub> film on Pb(Mg<sub>1/3</sub>Nb<sub>2/3</sub>)O<sub>3</sub>-PbTiO<sub>3</sub> single crystal substrate

In this chapter, we will describe the film deposition details and will present the properties of the composite. As this was a suitable system for detailed investigation of ME coupling effect, this was attempted and the results will be presented and discussed.

- Chapter 5: Conclusions and Future Work

In this chapter, we will summarize the study in this thesis and suggest some possible future work to further understanding this system.



## Chapter 2 : Experimental Techniques

### 2.1 Composite Synthesis

#### 2.1.1 Spark Plasma Sintering

Spark Plasma Sintering is a fast ceramic sintering technique. In a SPS system (Figure 2.1), a pulsed DC current passes through the graphite die, as well as the powder compact. The SPS process proceeds through three stages: plasma heating, joule heating and plastic deformation.<sup>29</sup> Due to joule heating, powder compacts will achieve near theoretical density at lower sintering temperature compared to conventional sintering techniques<sup>30</sup>. Different from the conventional hot pressing, the heat generation is internal in SPS. This sintering technique also has a very high heating or cooling rate (up to 1000 K/min); hence the sintering process is generally very fast. The high speed of the process promises the potential density of sample while avoiding coarsening of powders, which accompanies standard densification routes<sup>31</sup>. Actually, current plays the main role in densification without spark or plasma presenting in the process. The die used here acts as a heating source without the need of an external furnace, giving rise to very high heating rates. The advantages of SPS include high speed, uniformity and good purity, while the disadvantages include high cost and simple symmetrical shapes, which limit the application of this technique.

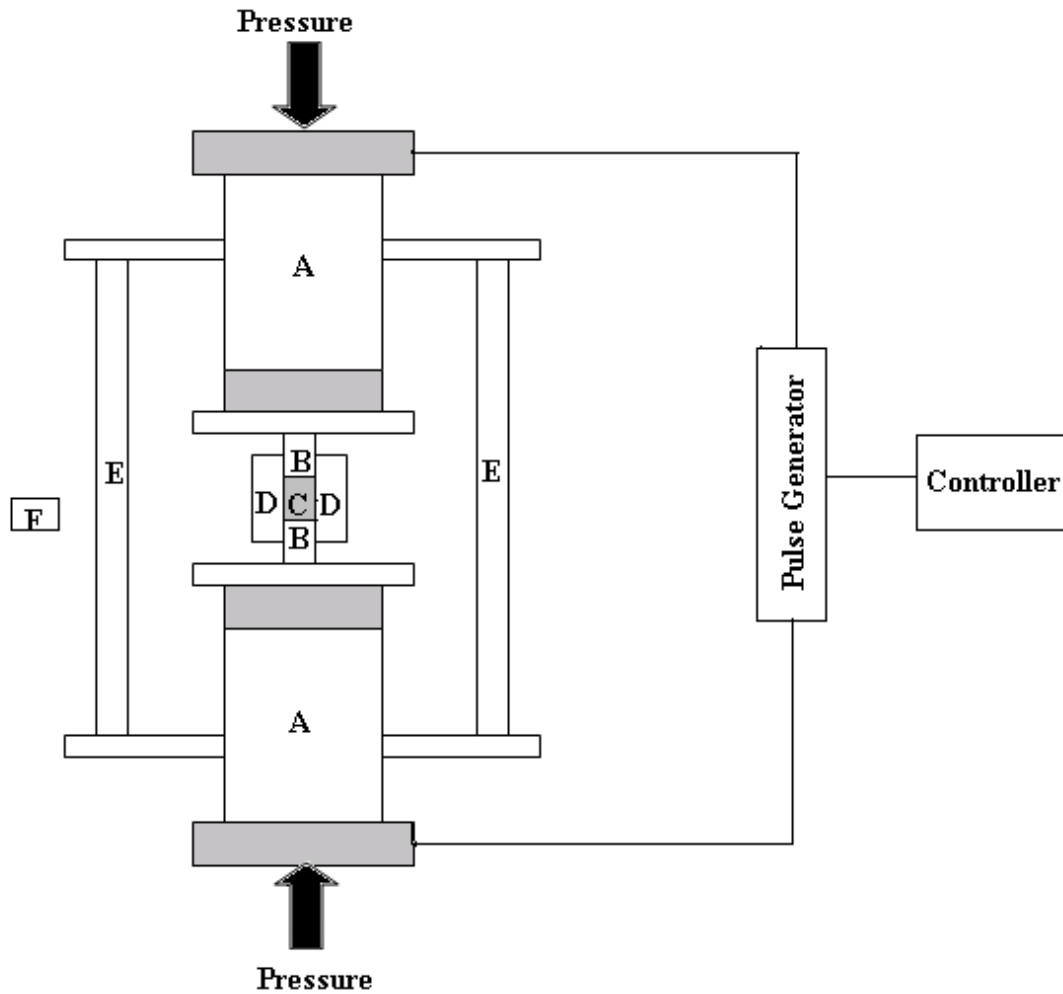


Figure 2.1: Schematic of the spark plasma sintering system: A: Punch Electrode, B: Punch, C: Sample, D: Graphite Die, E: Vacuum and Water Cooling Chamber, F: Optical pyrometer.<sup>29</sup>

### 2.1.2 Pulsed Laser Deposition

Pulsed laser deposition (PLD) is used as the film growth technique in this work. The schematic diagram of a typical PLD system is shown in Figure 2.2. It includes a laser source and a stainless steel vacuum chamber. During the deposition, a pulsed laser is produced and focused onto the target in the chamber by a lens. Typically, the energy of the laser pulses can change from  $0.01 \text{ J/cm}^2$  to  $1.2 \text{ J/cm}^2$  with a frequency from 1 Hz to 20 Hz, which leads to a variety to the ablation effect of the target materials. Target materials are dissociated from the surface and moving towards the heated substrate with strong forward-direction. The substrates can be heated and kept at different temperatures (usually from  $450^\circ\text{C}$  to  $800^\circ\text{C}$  for oxides) on a heater block before the deposition started. The deposition is usually conducted with some background gas, such as oxygen for our oxide films in this work.

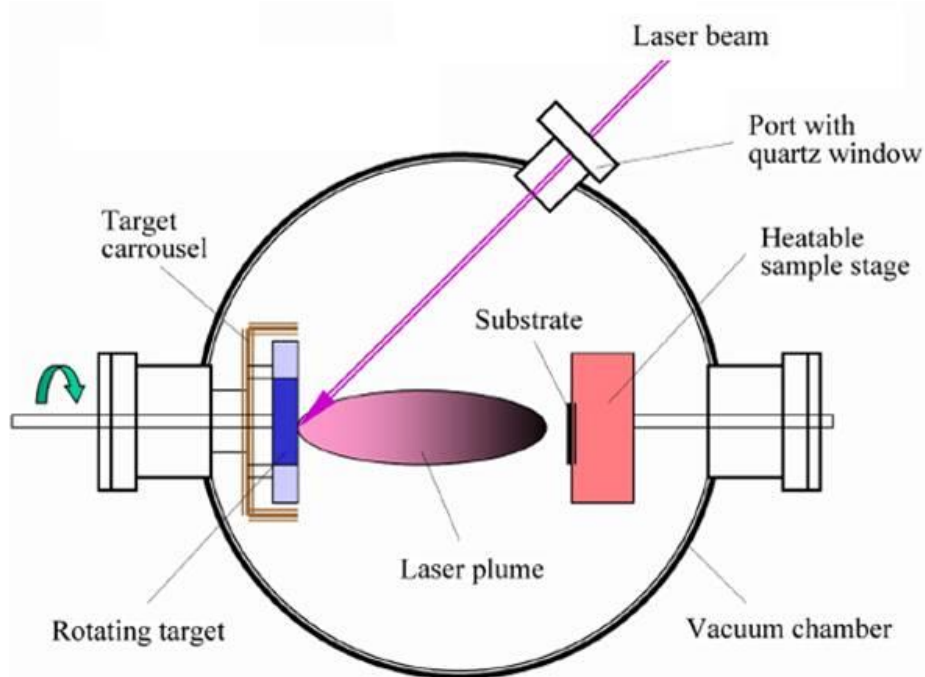


Figure 2.2: Schematic diagram of a pulsed laser deposition system.

The PLD process includes: a) the interaction between laser radiation and target; b) the dynamics of the ablated target materials; c) the deposition of the target materials on the substrate; d) the nucleation and growth of the films on the substrate. To achieve a high quality films, we need to optimize some parameters, such as: laser energy density and frequency, target-to-substrate distance, base pressure, substrate temperature and deposition gas pressure etc. Normally, the last two parameters (substrate temperature and deposition gas pressure) are most critical to the quality of the film. The substrate determines the crystallinity of the film. The film will crystallize only when the substrate temperature is above certain value. Especially for the epitaxial growth of oxide films, the temperature should be optimized for different materials. For the growth of oxide films, the oxygen partial pressure is also important to achieve the right composition of the film.

The commonly used lasers for PLD include ArF, KrF, XeF excimer lasers and Nd:YAG laser. In this study, we use KrF laser with a wavelength of 248 nm and pulsed width of 30 ns. The laser energy density used is  $\sim 1 \text{ J/cm}^2$ . The chamber is normally pumped to a base pressure of  $\sim 1 \times 10^{-5}$  Torr before deposition. The films studied in the present work are deposited under a dynamic oxygen pressure. Substrates are cleaned using a sequence of ultrasonic bath in acetone and ethanol before being loaded into the chamber.

The PLD has significant advantage in term of versatility. A lot of materials can be deposited in a wide range of gas pressures and substrate temperatures. Furthermore, this method can produce films with the same composition as the target material. It is a fast and relatively clean process, which allows us to easily deposit multilayer hetero-structures by using

different targets. However, the disadvantages of PLD are also obvious. For example, PLD has highly directional plume which leads to uniform film in a relatively small area. Therefore, the scaling up would be a problem for PLD in commercial industry development.

## 2.2 Structural Characterizations

### 2.2.1 X-Ray Diffraction

X-Ray Diffraction (XRD) is used for structural analysis and phase examine of the obtained samples. The diffraction occurs according to the Braggs' Law: <sup>32</sup>

$$n\lambda = 2d \sin \theta \quad \text{Eq.2.1}$$

in which  $n$  is an integer,  $\lambda$  is the wavelength of the X-ray (1.54056Å for copper  $K\alpha$ ),  $d$  is the lattice parameter of the crystal and  $\theta$  is the diffraction angle.  $\theta$ - $2\theta$  scanning is normally used to determine the crystalline orientation. During the measurement, the source and detector are kept at the synchronized angles to satisfy the Bragg condition. When the incident X-ray beam varies its angle, there will be a constructive interference of reflected signals while the angle ( $\theta$ ) reaches the corresponding crystalline lattice spacing of any planes of the sample ( Figure 2.3).

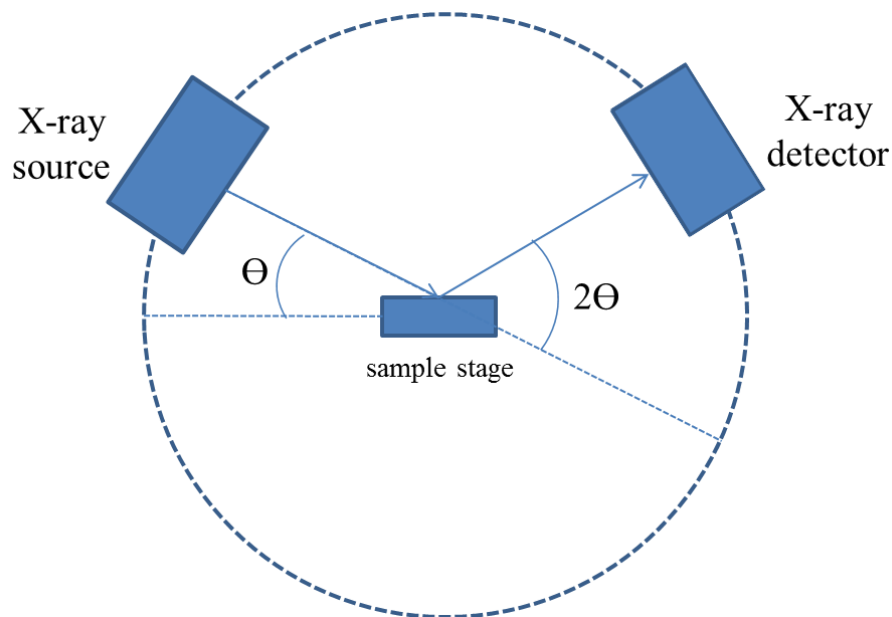


Figure 2.3: The schematic diagram showing how the  $\theta$ - $2\theta$  scanning works.

For the typical c-axis orientated films used in this study, only the (00 $l$ ) family planes will satisfy the Bragg condition and result in constructive peaks in  $\theta$ -2 $\theta$  scanning. To examine the epitaxial relationship,  $\Phi$  scan is generally performed. Since most epitaxial films are grown on single crystal substrates, high resolution XRD is conducted to provide more detail information of thin film lattice parameters. In the high resolution XRD system, the conventional high resolution  $\theta$ -2 $\theta$  scans provide the diffraction signals arising from the lattice planes parallel to the sample surface, giving the information of preferential growth axes (lattice planes). The  $\omega$ -scan rocking curve measurement is performed to evaluate the mosaic spreading of films. The in-plane XRD measurements are performed by controlling the incident angle to the sample surface plane in the accuracy of around 0.01 deg. Therefore, we can directly access and obtain the information of the lattice planes perpendicular to the film surface. Reciprocal Space Mapping (RSM) measurement and the pole figure measurements are employed to characterize the orientation relationships in the complex heteroepitaxial thin film systems (Figure 2.4). The wide range RSM data can be obtained by iterative motions of the goniometer for small  $\chi$  steps and 2 $\theta$ / $\omega$  scans. The 2D data can be shown either in the goniometer coordinates (the two coordinate axes are tilting angles ( $\chi$ ) and 2 $\theta$  angles) or in the reciprocal space coordinates.<sup>33</sup>

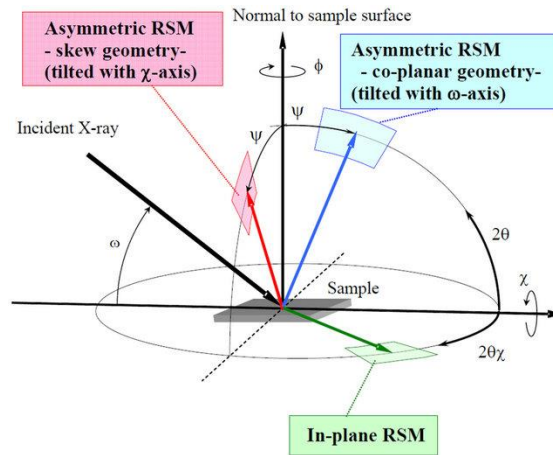


Figure 2.4: Geometry of the reciprocal space mapping measurement.<sup>33</sup>

### 2.2.2 Transmission Electron Microscopy

Transmission Electron Microscopy (TEM) is performed to characterize the microstructure of the samples. It provides information of sample structure and quality. Different from the optical microscope using light sources to form the image, TEM is a technique in which a beam of electrons is transmitted through an ultra-thin specimen, to form the images by interacting with the specimen as it passes through<sup>34</sup>. In TEM system, the electrons are emitted from a filament. They are then accelerated and focused onto the specimen. The transmitted diffracted electron beams are brought to focus on back focal plane of the objective lens to form a diffraction pattern. The final TEM images can also be produced by a series of electromagnetic lens as shown in Figure 2.5<sup>34</sup>. In selected area electron diffraction (SAED) mode, an intermediate aperture is inserted to confirm the diffraction patterns are produce by a selected area of the specimen. The separation of the diffraction spots shown on the screen can be used to calculate the interplanar spacing of the crystal<sup>34</sup>. The high resolution TEM (HRTEM) image can reveal the columns of atoms. To form the HRTEM



image, two or more diffraction beams are needed to be included in the objective aperture. The diffraction wave, as an electron wave function, is the Fourier transform of the scattering factor distribution in the specimen material. The specimen acts as a phase object to provide phase shift to the electron wavefront, which is very important to the image. The HRTEM image, also called the phase contrast image, is best understood in term of Fourier transform. The intensity at the image plane can be express as:

$$\begin{aligned}
 I(x, y) &= \varphi^*(x, y)\varphi(x, y) \\
 &= \left| 1 + iF(C(u, v))F(iF\sigma(\varphi(x, y)\Delta z))e^{i\chi(u, v)} \right|^2 \\
 &= 1 \pm f(\sigma, \Delta f, C_s, \lambda, r, \Delta z)\sigma\varphi(x, y)\Delta z
 \end{aligned}$$

Eq.2.2

From the above equation, it can be seen that the HRTEM image is a direct reflection of the projected crystal potential  $\varphi(x, y)$ . The image also depends on many parameters, such as the sample thickness  $\Delta z$  and the spherical aberration of the objective lens  $C_s$ .<sup>34</sup>

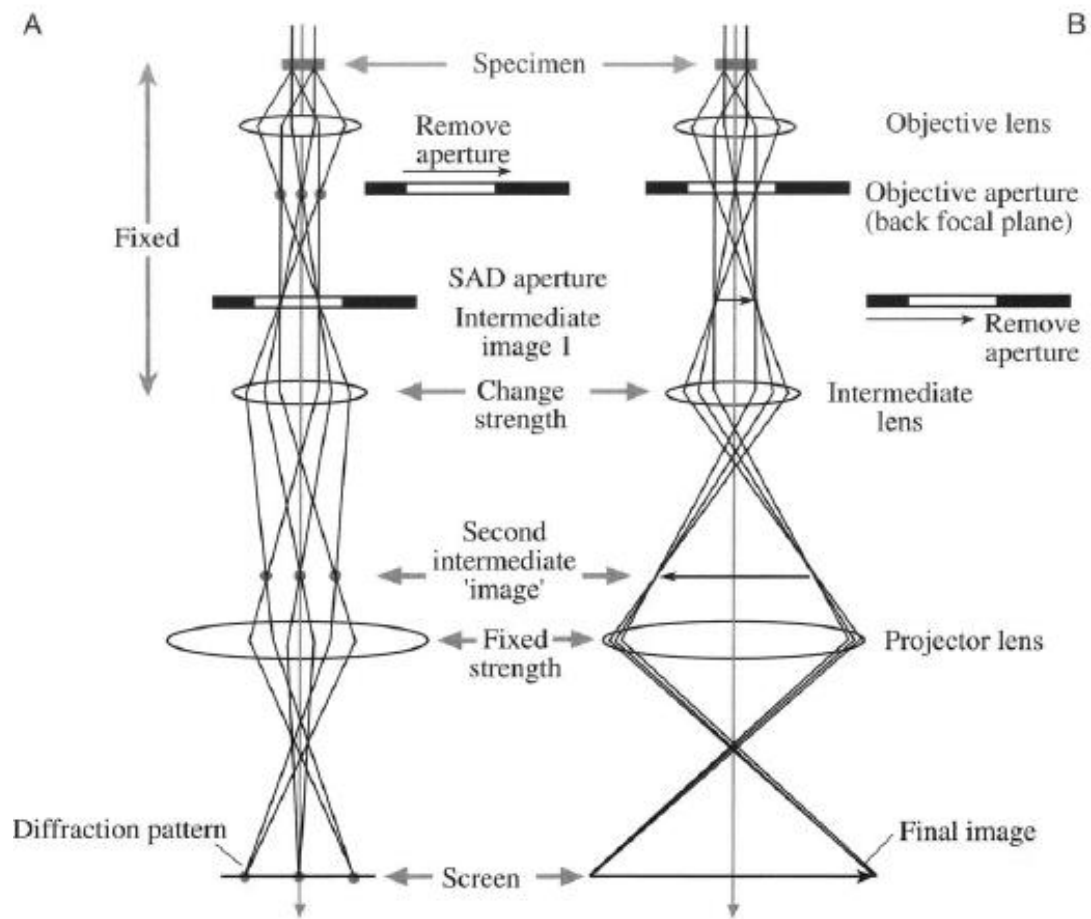


Figure 2.5: The two basic operation modes of a TEM: diffraction mode (left) and imaging mode (right).<sup>34</sup>

## 2.3 Electrical Measurements

Ferroelectric and piezoelectric properties are measured using a commercial ferroelectric testing system (Radiant Technology, Precision Premier). In this system, a series of voltage pulses is programmed from the generator and applied to the capacitor sample to form a hysteresis loop. A typical ferroelectric hysteresis loop is shown as below (Figure 2.6).<sup>35</sup> The derivative of the polarization with respect to applied voltage is given:

$$\delta P / \delta V \Rightarrow (\delta Q / \delta V) / Area \quad \text{Eq.2.3}$$

For the solid bulk samples in normal plate shape, the electrodes are provided by silver paste on the top and bottom. The area can be calculated from the plate area and the thickness is the plate's thickness. For the measurements of the ceramics with other irregular shape, we usually sputter Au electrodes with designed shadow mask. If the high voltage is needed in the testing, silicon oil is used to avoid sparking that may occur in air.

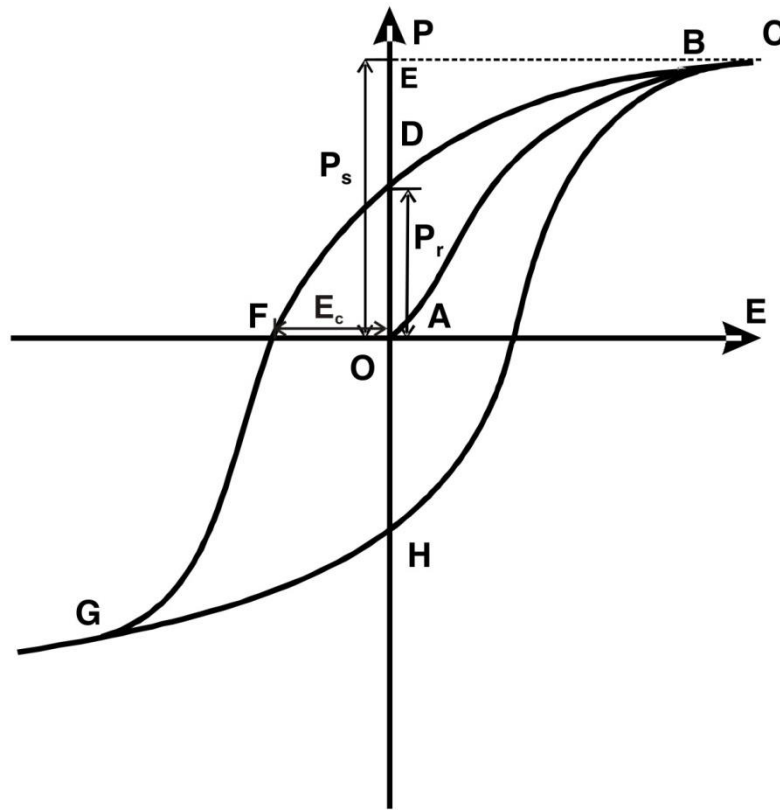


Figure 2.6: A typical ferroelectric hysteresis loop.  $P_s$ : spontaneous polarization;  $P_r$ : remanent polarization;  $E_c$ : coercive field.<sup>35</sup>

The measurement of Strain-Electrical field (S-E) loops is important for actuation applications.  $d_{33}$ , which is the slope of the S-E loop, is the piezoelectric coefficient, one of the most important parameters for actuators. The S-E loops derived by squaring the polarization data are usually shown with the appearance of the ‘butterfly loop’ (Figure 2.7).<sup>36</sup> The displacement generated by the piezoelectric effect on typical sized piezoceramic samples is as small as a few micrometres or less. Four commonly used techniques for this measurement are: fiber optic probe, capacitance probe, laser interferometry and strain

gauges<sup>36</sup>. These methods have the capability of measuring the small displacements with the necessary resolution and accuracy.

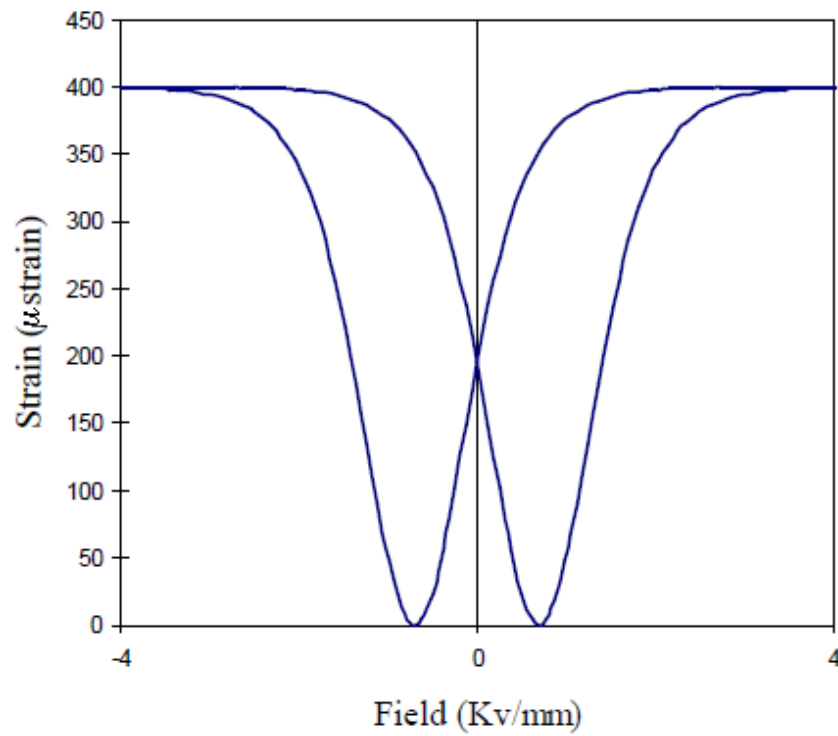


Figure 2.7: Schematic of the typical butterfly Stain-Electric field loop.<sup>36</sup>

## 2.4 Magnetic Measurements

### 2.4.1 Vibration Sample Magnetometer

The magnetic properties of the samples are measured using Vibration Sample Magnetometer (VSM). The principle is to induce a magnetic moment in the sample by placing it in a homogenous magnetic field. The vibration of sample will cause a magnetic flux change, which is converted into a voltage in the pick-up coils. In the typical VSM set up ( Figure 2.8), the sample is suspended by a non-magnetic rod which is connected to a vibrating drive head and placed in a magnetic field produced by two electromagnets. The vibrating head creates a sinusoidal vibration at a constant frequency. While the sample follows this vibration, it induces an electrical signal through the pick-up coils mounted on the faces of the electromagnets. This signal depends on the magnetic moment of the sample under the applied magnetic field. The magnetic moment of sample obtained from VSM is related to its magnetization.

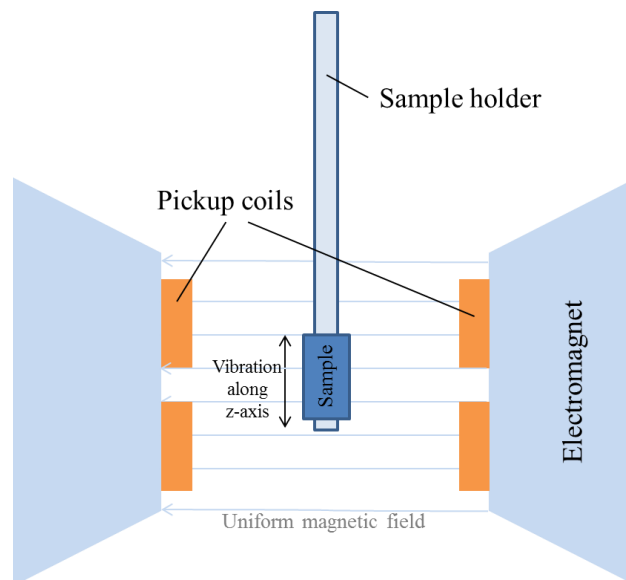


Figure 2.8: The schematic diagram of VSM systems.

In this work, magnetic properties of the samples were measured in a VSM (Lake Shore 7404) at room temperature with an applied magnetic field up to 12 kOe. The bulk samples used for the measurements were in the form of reground powder, while the thin films grown on substrates were cut into a suitable size and attached to the holder.

#### **2.4.2 Magnetic Force Microscopy**

Magnetic force microscopy (MFM) is an atomic force microscopy (AFM) based technique. As shown in Figure 2.9, in an AFM, as the tip scans along the surface of a sample, the deflection of the tip cantilever is picked up by a laser beam and reflected onto the photodiode. The laser spot on the photodiode is used as the feedback signal for the z axis piezoelectric stack. When the tip scans following the surface topography, the z axis piezoelectric stack will move the tip up and down to maintain constant oscillation amplitude. Tips of different materials are used for different purpose. In MFM, the probe used is a standard tip coated with a layer of magnetic material.

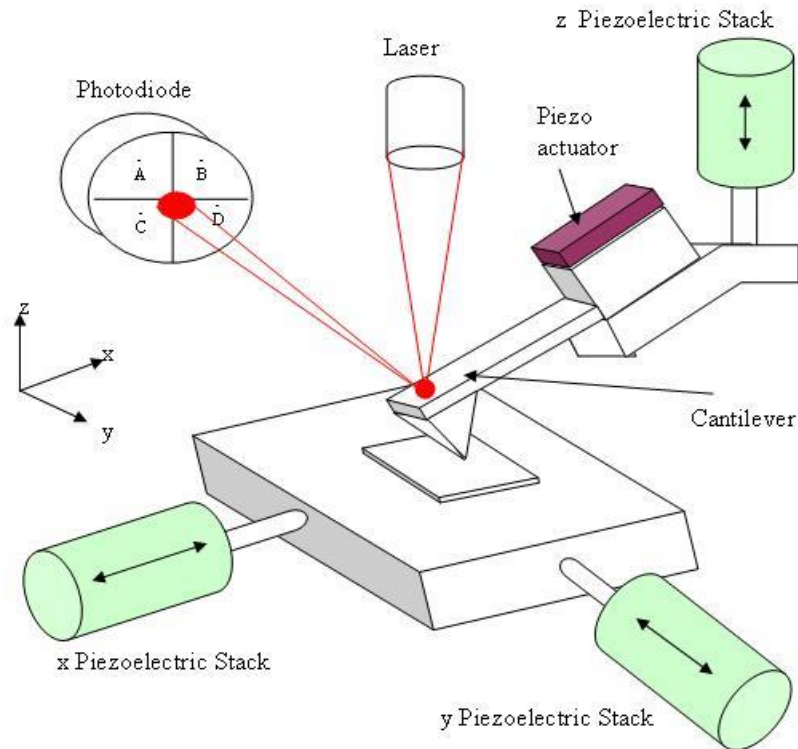


Figure 2.9: Various components of an AFM system.

Magnetic force microscopy is a powerful technique to directly observe the local magnetic domain structure of the sample. It is a dual path tapping mode (non-contact) technique. During the first scan, the tip is close to the sample surface and obtains the topography information. During the second scan, the tip is lifted by a certain distance from the sample surface and retraces the previous profile. The magnetic domain of the sample surface and the tip interact due to the magnetic force, resulting in a map of the magnetic domain of the sample. The bright and dark contrasts shown in the magnetic domain images reflect the different directions of magnetic dipoles.



# **Chapter 3 :      Multiferroic      BaTiO<sub>3</sub>-CoFe<sub>2</sub>O<sub>4</sub>      Bulk Composites**

## **3.1 Introduction**

Compared with thin films, bulk ceramic composites are easy to produce and can be scaled-up for industrial production. They are thus more relevant for practical applications. It is valuable to develop the process conditions for bulk multiferroic composites and understand the ME coupling in such systems.

To achieve a good multiferroic composite, we start with robust ferroelectric and ferro/ferrimagnetic components at room temperature. In this project, we investigated a composite consisting of BaTiO<sub>3</sub> (BTO) and CoFe<sub>2</sub>O<sub>4</sub> (CFO). BaTiO<sub>3</sub> and CoFe<sub>2</sub>O<sub>4</sub> are structurally compatible, ensuring a coherent interface between them. Their individual structure and properties have been extensively studied. Compared with Pb-based ferroelectric materials, BaTiO<sub>3</sub> has smaller polarization and piezoelectric coefficient. However, Pb is volatile and is well known to diffuse across interfaces easily at high temperatures. This may deteriorate the quality of the composite obtained as they have to be processed at high temperatures to obtain a high-quality product. Furthermore, BaTiO<sub>3</sub> does not exhibit any magnetic ordering in its pure form while CoFe<sub>2</sub>O<sub>4</sub> has no ferroelectric ordering. Thus, they form an ideal model system for examining the strain-mediated ME coupling without complications from intrinsic effects of each constituent phase.

### **BaTiO<sub>3</sub> (BTO)**

BaTiO<sub>3</sub> belongs to the perovskite family and is one of the most studied ferroelectric materials. The crystal structure of BaTiO<sub>3</sub> transforms from cubic (Pm-3m) to tetragonal (P4mm) as the temperature goes below the ferroelectric Curie temperature ( $T_c \approx 128\text{ }^\circ\text{C}$ ), and then to orthorhombic (Amm2) near  $0\text{ }^\circ\text{C}$  and finally to rhombohedral (R3m) at about  $-90\text{ }^\circ\text{C}$ <sup>37</sup>. In BaTiO<sub>3</sub>, the displacement of Ti ion within the oxygen octahedral cage leads the spontaneous polarization. BaTiO<sub>3</sub> is widely used because of its high dielectric constant and good ferroelectric properties at room temperature. According to the theoretical calculation, the ferroelectric polarization of BaTiO<sub>3</sub> should be  $23.75\text{ }\mu\text{C}/\text{cm}^2$ . A slight increase may occur in BaTiO<sub>3</sub> and SrTiO<sub>3</sub> superlattice<sup>38</sup>. In ceramics, the electrical properties of BaTiO<sub>3</sub> also depend on grain size. At room temperature, BaTiO<sub>3</sub> ceramics with fine grains show a high permittivity  $\epsilon_r$  (3500-6000) compared to that (1500-2000) in coarse-grained ceramics. This enhancement is sometimes attributed to the greater internal stress or the increased density of  $90^\circ$  domain walls<sup>39</sup>. For certain applications, polycrystalline films are thus more desirable for their high permittivity than epitaxial films<sup>40</sup>. Other processing parameters, such as the annealing temperature and substrate choice, also affect the properties of BaTiO<sub>3</sub>.<sup>41</sup> It is thus critical that the processing conditions are optimized for this project.

## CoFe<sub>2</sub>O<sub>4</sub> (CFO)

CoFe<sub>2</sub>O<sub>4</sub> is a typical ferrite with an inverse spinel structure. It is a good microwave magnetic material with large magnetization (Table 1<sup>42</sup>), relatively high resistivity and low loss at high frequency<sup>42</sup>. In the case of CoFe<sub>2</sub>O<sub>4</sub> nanoparticle systems, each particle behaves as a single domain. When an alternating magnetic field is applied to these particles, if thermal energy is large enough for the spins to overcome their blocking energy barrier they will flip with the alternating magnetic field. In the case of epitaxial films grown on SrTiO<sub>3</sub> single crystalline substrates, measurements reveal that the CoFe<sub>2</sub>O<sub>4</sub> film exhibits an increased out-of-plane magnetization (190 emu/cm<sup>3</sup>) with a large coercivity (3.8 kOe) at room temperature<sup>43</sup>. This is common in strained films and is usually attributed to the in-plane compressive strain induced by the lattice misfit between the film and substrate. This magnetic anisotropy is also found to be sensitive to film thickness<sup>44</sup>, again pointing to the misfit strain as the cause.

Table 1: Magnetic Properties of ferrites.<sup>42</sup>

Ferrites	T <sub>c</sub> in K	Saturation at 0 K in M <sub>B</sub>	Magnetization per gram gauss/cm <sup>3</sup>
CoFe <sub>2</sub> O <sub>4</sub>	790	3.7	90
NiFe <sub>2</sub> O <sub>4</sub>	858	2.2	56
MnFe <sub>2</sub> O <sub>4</sub>	585	4.6	112
CuFe <sub>2</sub> O <sub>4</sub>	720	1.3	30
Fe <sub>3</sub> O <sub>4</sub>	858	4.1	98
MgFe <sub>2</sub> O <sub>4</sub>	710	1.1	31

### 3.2 Composite Synthesis

Composites of 70%  $\text{BaTiO}_3$  and 30%  $\text{CoFe}_2\text{O}_4$  were synthesized using ball milling technique with conventional sintering and fast sintering processes. Ferromagnetic phase  $\text{CoFe}_2\text{O}_4$  was produced from high purity powders of  $\text{CoO}$  (~325 mesh, ALDRICH) and  $\text{Fe}_2\text{O}_3$  (99.9%, Alfa Aesar). Stoichiometric amount of raw powders were mixed and milled in a planetary ball mill (Fritsch PM/5) in tempered steel vials together with 10 mm diameter tempered steel milling balls. The vials were filled with argon gas and run at the speed of 250 rpm with interruptions of 5 minutes for every 10 minutes. After 40 hours milling, the powder was removed and calcined at 800 °C for 2 hours to produce  $\text{CoFe}_2\text{O}_4$ . Subsequently,  $\text{CoFe}_2\text{O}_4$  and  $\text{BaTiO}_3$  powder (99.9%, ALDRICH) in the weight ratio of 7:3 was ball milled for 50 hours under the same condition. Two sintering methods were used to produce the multiferroic composite: 1) conventional sintering of cold pressed pellets from the as-milled powder, for 4 hours at different temperatures between 700 °C and 1200 °C; and 2) Spark plasma sintering (SPS).

In the SPS process, the fine mixture of milled powders was loaded into a graphite die and sintered at a heating rate of 100 °C /min with a holding period of 3 minutes at the desired temperature by allowing a pulsed DC current to flow through the die and the specimen. Simultaneously, a pressure of 30 MPa was applied during heating up and holding periods, and was released during the cooling part of the sintering cycle. The sintering temperature was monitored by a conventional thermocouple attached at the side of the graphite die up to 1000 °C. These samples were later to evaporate any carbon contamination from the graphite die and graphite paper.

### 3.3 Phase Identification

X-ray diffraction patterns of the as-milled and sintered samples are shown in Figure 3.1. The as-milled sample shows pure  $\text{BaTiO}_3$  and  $\text{CoFe}_2\text{O}_4$  phases. Same phases are observed in the SPS-produced sample indicating that no reaction has occurred between the two components. However, the samples prepared using conventional sintering at  $1200^\circ\text{C}$  show impurity phases  $\text{BaTi}_2\text{Co}_2\text{Fe}_8\text{O}_{18}$ , indication possible reactions between the two phases. No such reaction products can be observed for samples sintered at lower temperatures.

Although  $\text{BaTiO}_3$  and  $\text{CoFe}_2\text{O}_4$  are line compounds with very little mutual solubility in the phase diagram, high temperatures appear to induce a reaction leading to a new phase<sup>45</sup>. In comparison, SPS method gives a clean composite with high density with very short processing time, which helps to prevent the formation of secondary phases.

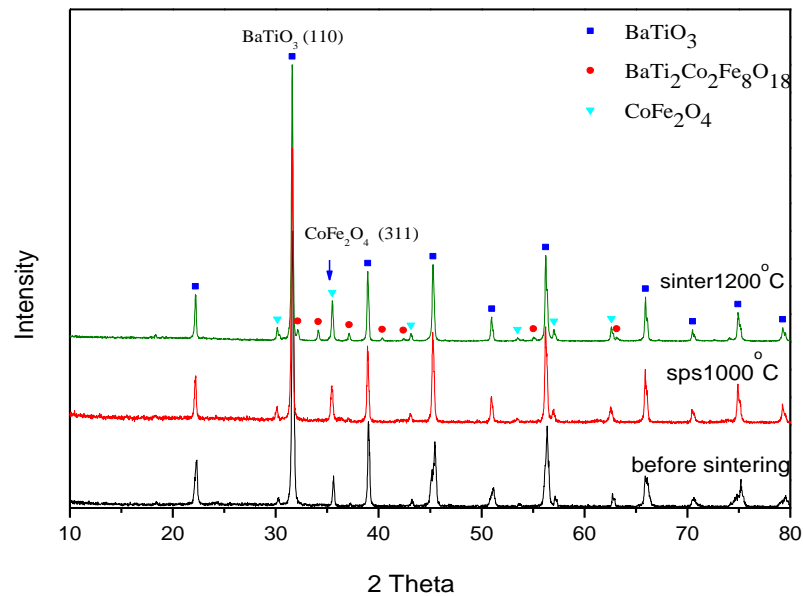


Figure 3.1: XRD patterns of the as-milled, conventionally sintered, and SPS sintered bulk composites.

### 3.3 Efficiency of Sintering

The apparent density of the obtained sample is shown in Figure 3.2 for each sintering condition. As expected, the apparent density increases with the sintering temperature for both techniques, which was also confirmed by scanning electron microscopy (SEM) investigations. The SPS process generally gives substantially higher densities compared to the conventionally sintered samples at the same temperatures. Using the theoretical densities of  $5.96 \text{ g/cm}^3$  for  $\text{BaTiO}_3$ , and  $5.32 \text{ g/cm}^3$  for  $\text{CoFe}_2\text{O}_4$ , the theoretical density of this 70% $\text{BaTiO}_3$ -30%  $\text{CoFe}_2\text{O}_4$  composite should be  $5.75 \text{ g/cm}^3$  if we ignore any strain relaxation during the formation of the composite i.e. assuming the volume to be the sum of the volumes of the individual phase.

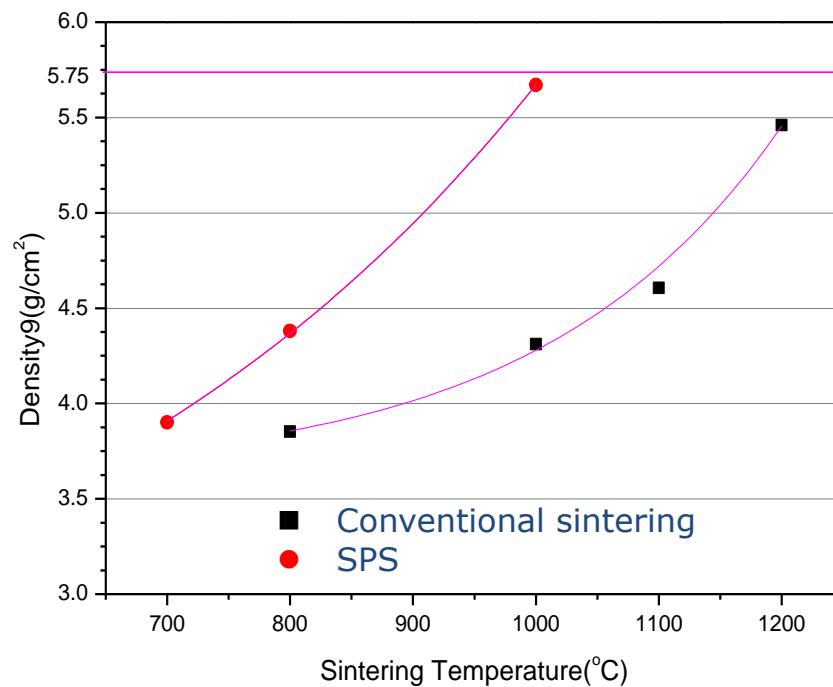


Figure 3.2: The composite density vs sintering temperature for both the conventional technique and SPS.

### 3.4 Microstructure

The microstructures of the sintered samples are shown in Figure 3.3. Note the absence of porosity and the finer grain structure in the SPS sintered samples. BaTiO<sub>3</sub> is the bright phase as seen in Figure 3.3(a, c and e) while the dark regions with rough surface (seen in Figure 3.3(d and f)) is the CoFe<sub>2</sub>O<sub>4</sub>. This was later confirmed by Energy-dispersive X-ray spectroscopy (EDS) analysis. Well sintered samples were obtained at 1200 °C (Figure 3.3) by the conventional sintering method, while such dense samples could be achieved at 1000 °C in 3 mins by the SPS processing. In the lower magnification micrographs, the phases give different contrasts. The distribution of phases appears to be uniform in conventionally sintered samples as well as in the SPS samples. Compared to the surface, the centre of the SPS sample shows a finer structure with greater uniformity and phase distribution.

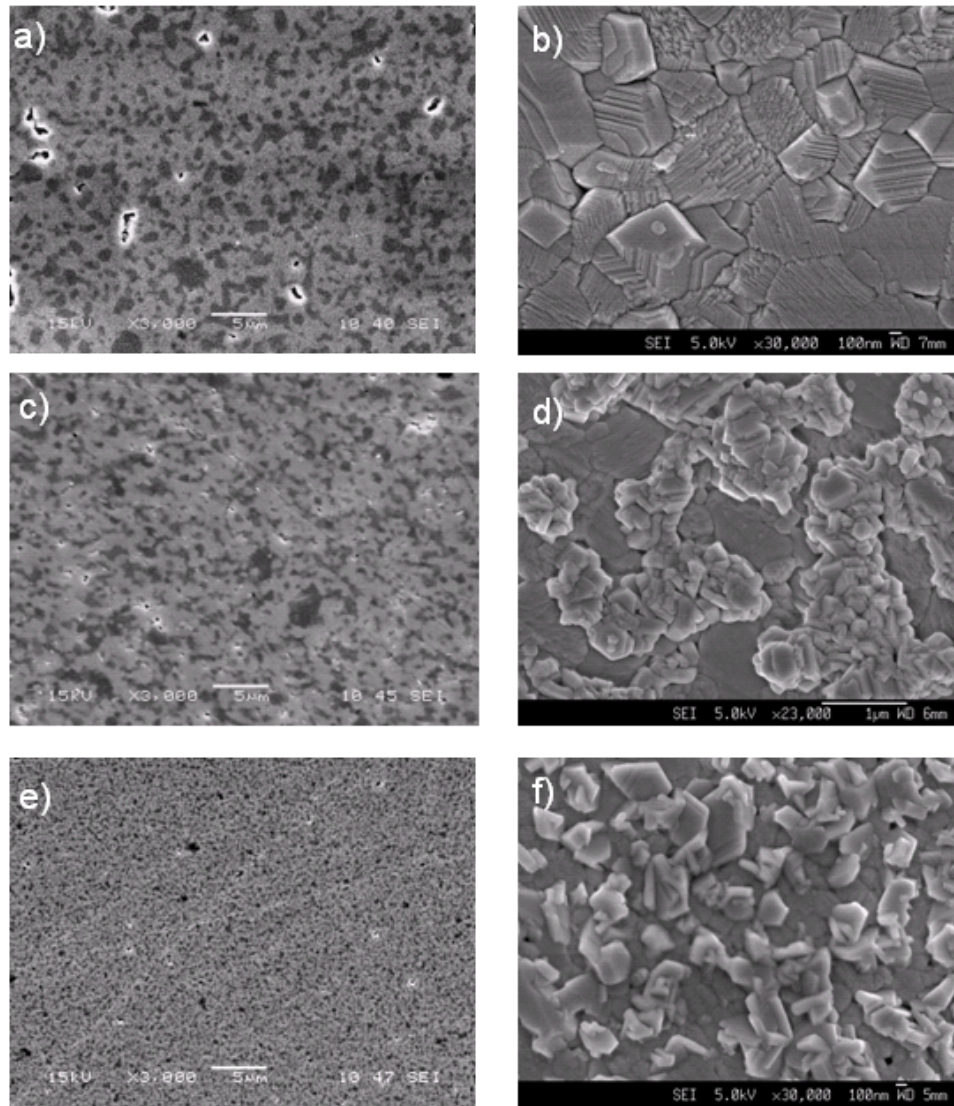


Figure 3.3: SEM micrographs of the surfaces of the composites. (a) and (b) conventionally sintered at 1200 °C, (c) and (d) SPS sintered at 1000 °C near the surface, (e) and (f) SPS sintered at 1000 °C at the center.

Note that the  $\text{CoFe}_2\text{O}_4$  phase appears to agglomerate near the surface in the SPS samples. This could be due to slight difference in the local temperature within the sample as the temperature sensor is near the surface. The rapid heating of the graphite die must have raised



the surface temperature to higher levels and the short dwelling time of 3 mins might have been insufficient for the temperature to conduct evenly across the sample. The average grain sizes determined by mean linear intercept are approximately 400 nm and 260 nm for the samples shown in Figure 3.3 (b) and (d), respectively. The samples conventionally sintered at the lower temperatures have densities typically lower than 90% and hence are not used for the subsequent electrical and magnetic measurements. However, XRD was performed and it was shown that no impurity phases formed during sintering.

The sample sintered at 1200 °C by conventional method was examined in detail by the back scatter detector to identify the presence and the distribution of the impurity phase  $\text{BaTi}_2\text{Co}_2\text{Fe}_8\text{O}_{19}$  that was detected by XRD. A back scatter electron micrograph shown in Figure 3.4 exhibits three different grey levels. The mean back scatter coefficients “ $\eta$ ” of the phases are:  $\text{BaTiO}_3 = 0.3441$ ,  $\text{CoFe}_2\text{O}_4 = 0.2379$  and  $\text{BaTi}_2\text{Co}_2\text{Fe}_8\text{O}_{19} = 0.2546$ . Consequently,  $\text{BaTiO}_3$  shows up as the brightest phase while  $\text{CoFe}_2\text{O}_4$  is the darkest and the impurity is intermediate. EDS analysis conducted at three locations with three different grey levels confirms this expectation. The relative magnitudes of Ba, Ti, Fe and the Co peaks reveal the compositions qualitatively.

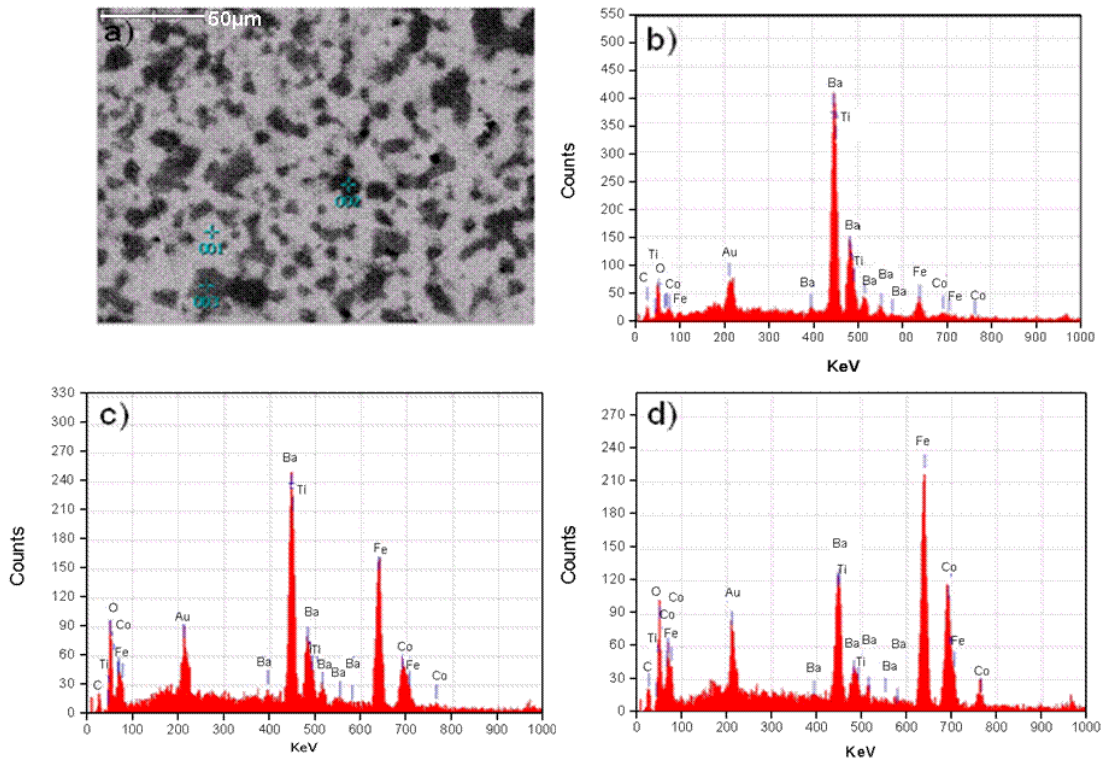


Figure 3.4: (a) Backscattered electrons image of the sample conventionally sintered at 1200°C with three zones of contrasts. (b) EDS spectrum at point 001 with the brightest contrast, (c) EDS spectrum point 002 with intermediate gray contrast. (d) EDS spectrum at point 003 with the darkest contrast,

## 3.5 Magnetic and Ferroelectric Properties of the Bulk Composites

### 3.5.1 Magnetic Properties

Hysteresis loops typical of ferromagnetic materials are observed in all samples at room temperature. Figure 3.5 shows the M-H curves for some selected samples. Figure 3.5(a) compares the as-milled powder with the composite conventionally sintered at 1200 °C. Note that the coercivity has significantly decreased after sintering but the saturation magnetization has increased. This could be attributed to the extremely high defect population expected in the as-milled material. Such defects are pinning centers for domain wall movement, which is the reason for increased coercivity. All sintered samples generally show lower coercivities and comparable saturation magnetization. In Figure 3.5(b), we compare two sintered samples with that of pure  $\text{CoFe}_2\text{O}_4$ . As expected, the saturation magnetization of pure  $\text{CoFe}_2\text{O}_4$  is much higher. The essential information in Figure 3.5 is extracted and presented in Table 2. It is clear that the saturation magnetization of the sintered samples appear to follow their densities with the densest sample showing the highest value. Although this would be expected, the actual effect on the saturation moment appears to be higher than what could be attributed to porosity alone. This is illustrated by the following calculation. The magnetic moment per mole of  $\text{CoFe}_2\text{O}_4$  can be computed from the M-H curve for pure  $\text{CoFe}_2\text{O}_4$  and is tabulated in Table 2. Since all the sintered samples contained nominally the same moles of  $\text{CoFe}_2\text{O}_4$ , they should all generate the same moment and hence the same saturation value. However, converting the experimental saturation magnetization to moment per mole of  $\text{CoFe}_2\text{O}_4$  shows that the largest molar moment of 14491 emu is obtained in SPSSintered sample at 1000°C and is 84% of the 17261 emu displayed by pure  $\text{CoFe}_2\text{O}_4$ .

Note that this is after accounting for the molar content in the composite. But the porosity in this SPS sample is only about 2% and thus we cannot attribute the loss of 16% in saturation moment totally to porosity. This implies that  $\text{CoFe}_2\text{O}_4$  in the composite has a reduced magnetization than pure sample.

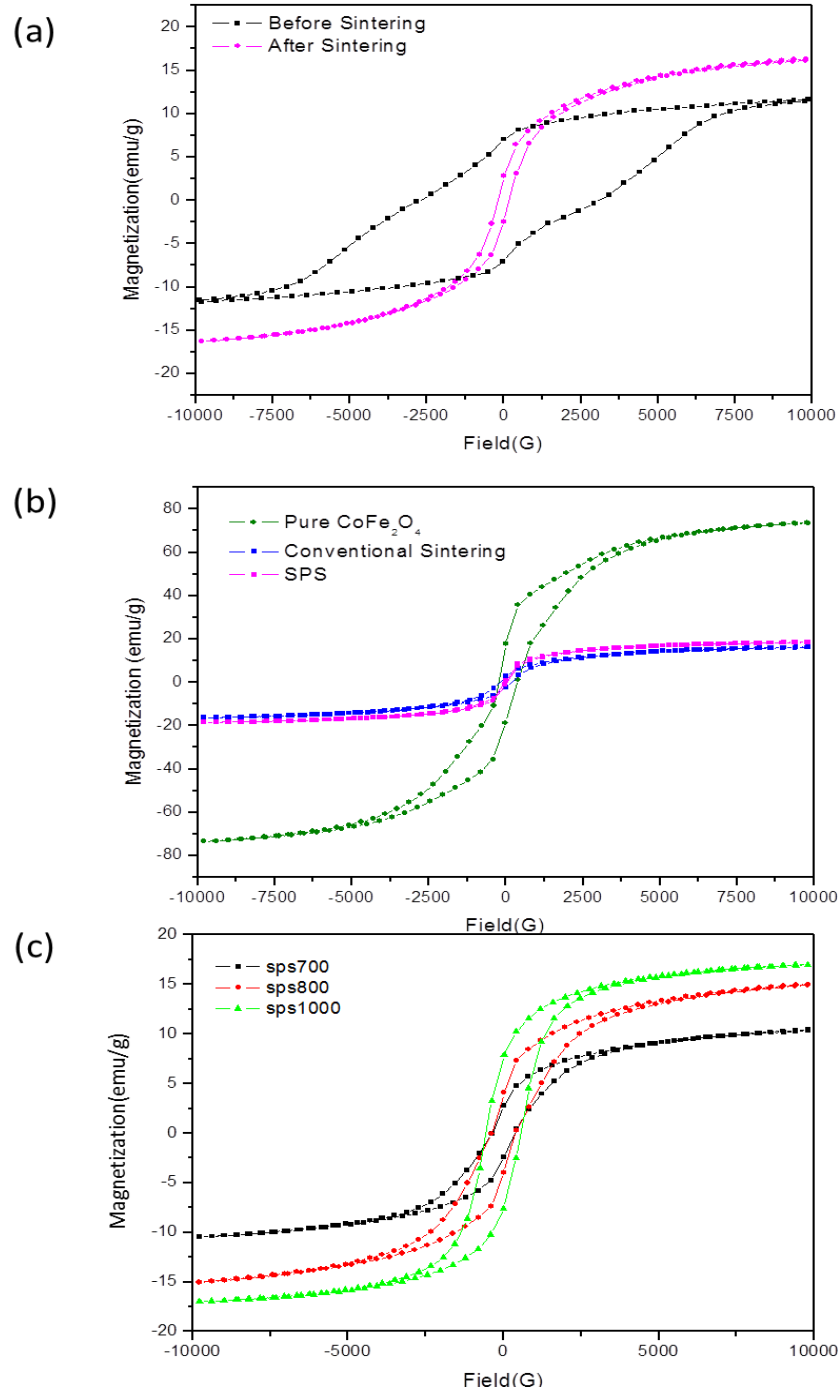


Figure 3.5: The typical Hysteresis loops of composites that are (a) before and after sintering, (b) synthesized in different techniques, and (c) SPS in different temperature.

Table 2: Important magnetic data of samples obtained from Figure 3.5

Samples	Saturation Magnetization ( $M_s$ )		Coercivity ( $H_c$ ) $G$
	$emu/g$	$emu/mol$ of $CoFe_2O_4$	
Pure $CoFe_2O_4$	73.571	17261.96	307.48
as-milled composite	11.989	9376.60	2918.6
SPS sintered 800 °C	15.033	11757.31	368.41
Conventionally sintered 1200 °C	16.297	12745.88	188.06
SPS sintered 1000 °C	18.529	14491.53	35.381

The magnetic domain structures observed by MFM are shown in Figure 3.6. Note that the domains are constrained to the  $CoFe_2O_4$  phase, and that the domain structure in the SPS sintered sample is much more obvious and complex than that in the conventionally sintered sample. This could be a consequence of the finer distribution of  $CoFe_2O_4$  phase. The finer distribution will contribute to increasing interface between  $CoFe_2O_4$  and  $BaTiO_3$  phase,

which will indicate a possibly higher ME coupling effect in the SPS sintered sample. The nonmagnetic  $\text{BaTiO}_3$  phase wouldn't interact with the magnetic tips. Thus, they are only shown as the brown color in the MFM maps. However, the absence of magnetic response in the  $\text{BaTiO}_3$  phase must have some effect to the magnetic domain structure in  $\text{CoFe}_2\text{O}_4$ . The magnetic lines have to cross this non-magnetic phase to interact with the domain in the nearest  $\text{CoFe}_2\text{O}_4$  region. A finer microstructure means that inter-  $\text{CoFe}_2\text{O}_4$  phase distance is smaller which could lead to greater reinforcement of the domains of neighboring  $\text{CoFe}_2\text{O}_4$  particles. This may be a reason for exhibiting larger emu per mole for the fine structured samples. The clear phase structures shown in these MFM images also imply that the ferroelectric properties will not be good due to the leakage problem. The defects of MFM images from the rough surface are normal due to the mechanical polish. Dark and bright contrasts in Figure 3.6(b) and (c) indicate opposite magnetization directions. The larger particles have more than one domain leading to approximately zero net moment from each particle when there is no external field while the small particles are not large enough to accommodate a multidomain structure.

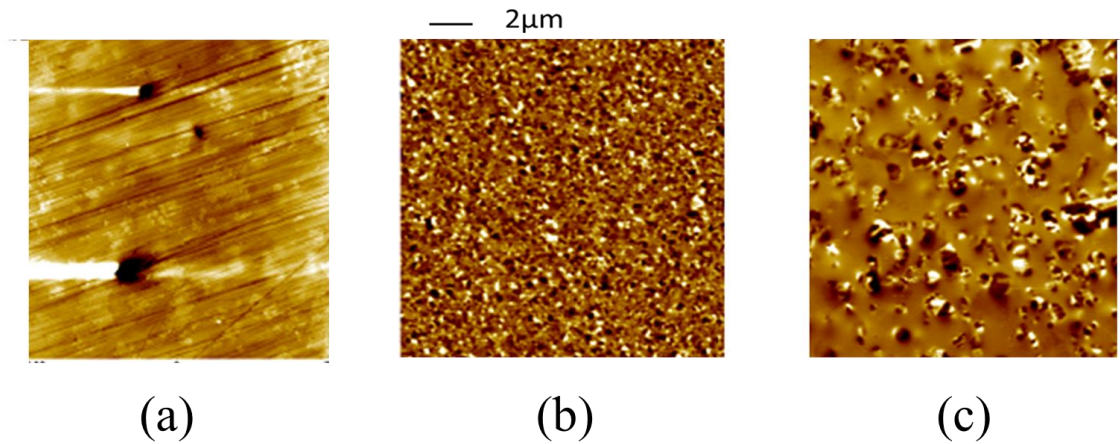


Figure 3.6: AFM topography and MFM images of the  $\text{BaTiO}_3\text{-CoFe}_2\text{O}_4$  composites: (a) shows typical topography of the polished surface. (b) and (c) are MFM phase images of the SPS produced and conventionally sintered samples, respectively; Bright and dark contrasts in these MFM images indicate up and down magnetization directions at the respective locations in these samples.



### 3.5.2 Ferroelectric Properties

The ferroelectric test is performed on the bulk composites with two silver electrodes. The samples are immersed in silicon oil to prevent arc discharging. The polarization vs electrical field (P-E) loops are shown in Figure 3.7. The hysteresis loops indicate that the composites are ferroelectric. The loops observed are typical for ferroelectric materials with relative low resistivity. We can see that the saturation polarization  $P_m$  appears near the maximum applied electric field of 35 kV/cm. Under higher electric fields leakage current becomes evident. The slimmer loops observed for the SPS sintered sample is not understood. Nevertheless, the samples exhibit both magnetic and ferroelectric ordering simultaneously, and it is likely that these composites should exhibit ME coupling effects.

When it comes to measuring the ME coefficient in a bulk composite, the direct coefficient  $\alpha$ , which describes the electric voltage (or polarization) generated under a magnetic field is usually measured. In many applications it is the reverse effect that is useful, i.e. the magnetic moment generated when an electric field is applied. Nevertheless, both measurements on our bulk composites have proven to be very challenging. This is partially because of the low resistivity of the composites, and the random orientation of the grains. Under external fields, the strain generated by various grains may cancel each other out, leading to very small overall response. After many failed attempts, we have to conclude that ME coupling coefficient of these bulk composites cannot be determined at the moment. We thus turned

our attention to the magnetic film on active piezoelectric substrate system, which will be described in details in Chapter 4.

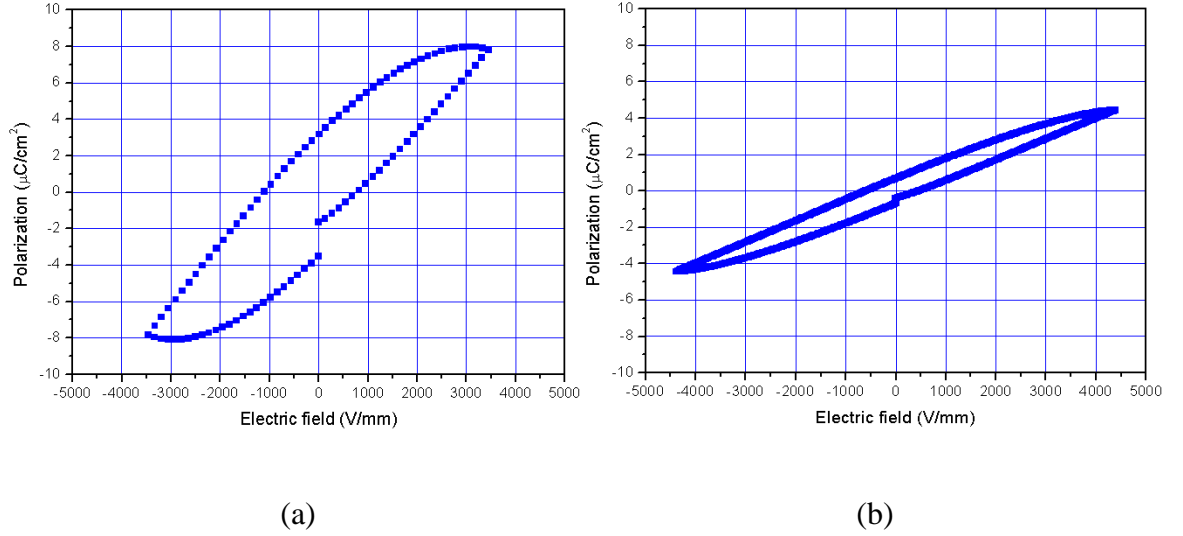


Figure 3.7: Ferroelectric hysteresis loops of the samples which are (a) conventionally sintered at 1200°C and (b) SPS sintered at 1000°C, respectively.

### 3.6 Conclusions

We have produced multiferroic bulk composites consisting nominally 70 wt% - BaTiO<sub>3</sub> and 30 wt% - CoFe<sub>2</sub>O<sub>4</sub> as the chosen FE and FM components. Ball milling was used to mix the powders thoroughly followed by sintering to synthesize and densify the samples: conventional sintering and spark plasma sintering (SPS) were both used. The following conclusions can be drawn from this work:

- Phase pure composites can be successfully synthesized by high energy ball milling of BaTiO<sub>3</sub> and CoFe<sub>2</sub>O<sub>4</sub> powders followed by high temperature sintering. There was no noticeable reaction between the two phases until 1100 °C when conventional sintering method was used. At 1200 °C, an undesirable secondary phase BaTi<sub>2</sub>Co<sub>2</sub>Fe<sub>8</sub>O<sub>18</sub> starts to appear. However, no such secondary phases were detected in SPS sintered samples up to 1200 °C.
- The density of SPS sintered samples was consistently higher than those conventionally sintered at the same temperature. The microstructure of the SPS sintered samples was much finer than that of conventionally sintered ones. Hence, SPS is recommended as the densification method to produce these composites.
- The magnetic coercivity decreases considerably upon sintering due to the elimination of the defects in the as-milled products. The saturation magnetization also increases. SPS samples consistently exhibit higher saturation magnetization than those conventionally sintered. This could be attributed to the higher density and the finer microstructure in SPS samples.

- MFM investigations clearly show magnetic domains of opposite orientations within the  $\text{CoFe}_2\text{O}_4$  phase. The samples also exhibit ferroelectric hysteresis loops but the SPS sintered samples require a very high electric field to reach saturation.
- The coexistence of both ferroelectric and magnetic properties demonstrates that the  $\text{BaTiO}_3$ - $\text{CoFe}_2\text{O}_4$  composite is multiferroic. However, attempts to quantify the ME coupling effect in this system were not successful. This could be due to the low electrical resistivity of the composites, and the random orientation of the grains. Under an external electric field, the strain fields generated by the different  $\text{BaTiO}_3$  grains may not be additive due to their random crystal orientation and, hence, may nullify each other to some extent, leading to a very small macroscopic response.

# **Chapter 4 : Multiferroic Thin Film Composites- CoFe<sub>2</sub>O<sub>4</sub> Film on Pb(Mg<sub>1/3</sub>Nb<sub>2/3</sub>)O<sub>3</sub>-PbTiO<sub>3</sub> Single Crystal Substrate**

## **4.1 Introduction**

Thin film composites were chosen as the components can be chosen from a wide range of piezoelectric and piezomagnetic (magnetostrictive) materials and could be deposited by a variety of established techniques in any sequence. Also, there are various forms of combinations in the studies of multiferroic composites, such as nanoparticulate composites<sup>46</sup>, multilayer heterostructures<sup>47</sup> and vertical nanopillar-in-matrix structures<sup>18</sup>. In all these composites, the ME coupling effect is thought to be mediated by strain transfer across the interface between the active components. It is thus imperative that these components be free to deform. In conventional laminate systems, the films are deposited on a passive substrate such as SrTiO<sub>3</sub>. The coupling in these systems was found to be weak due to the clamping effect induced by the massive substrate<sup>48</sup>. To enhance the coupling effect, researches resorted to vertical nanopillar-in-matrix composite films where the large out-of-plane interface area between the two phases could provide effective strain coupling while the small, in-plane interface with the substrate will reduce the clamping effect in the out-of-plane direction<sup>18,19,21,22</sup>. However, such composite films are confined to specific material systems and are not easy to produce<sup>49,50</sup>. As an alternative, recently some research groups introduced an alternative thin film system, in which substrates are active piezoelectric

crystals. Such formation could eliminate the substrate clamping effect all together and enhance coupling in the in-plane direction<sup>51,52,53,54,55</sup>.

Eerenstein et al. reported electrically-induced magnetic changes (up to  $2.3 \times 10^{-7} \text{ s m}^{-1}$ ) in a system in which ferromagnetic 40 nm thick  $\text{La}_{0.67}\text{Sr}_{0.33}\text{MnO}_3$  film was deposited on 0.5 mm thick ferroelectric  $\text{BaTiO}_3$  substrates<sup>51</sup>. They proved strain coupling via ferroelastic, non- $180^\circ$   $\text{BaTiO}_3$  domains by X-ray diffraction. As they showed, the film was relaxed and the substrate ferroelectric patterns were dramatically modified when an electric field of 3-10  $\text{kV cm}^{-1}$  was applied. They showed that (Figure 4.1) a large, sharp and persistent magnetic transition occurs at some threshold voltage at different temperatures. This study indicates that the ME coupling effect is non-destructive and reversible. However, because of the limitation of  $\text{La}_{0.67}\text{Sr}_{0.33}\text{MnO}_3$ , an alternative material is needed to achieve effective room-temperature coupling.

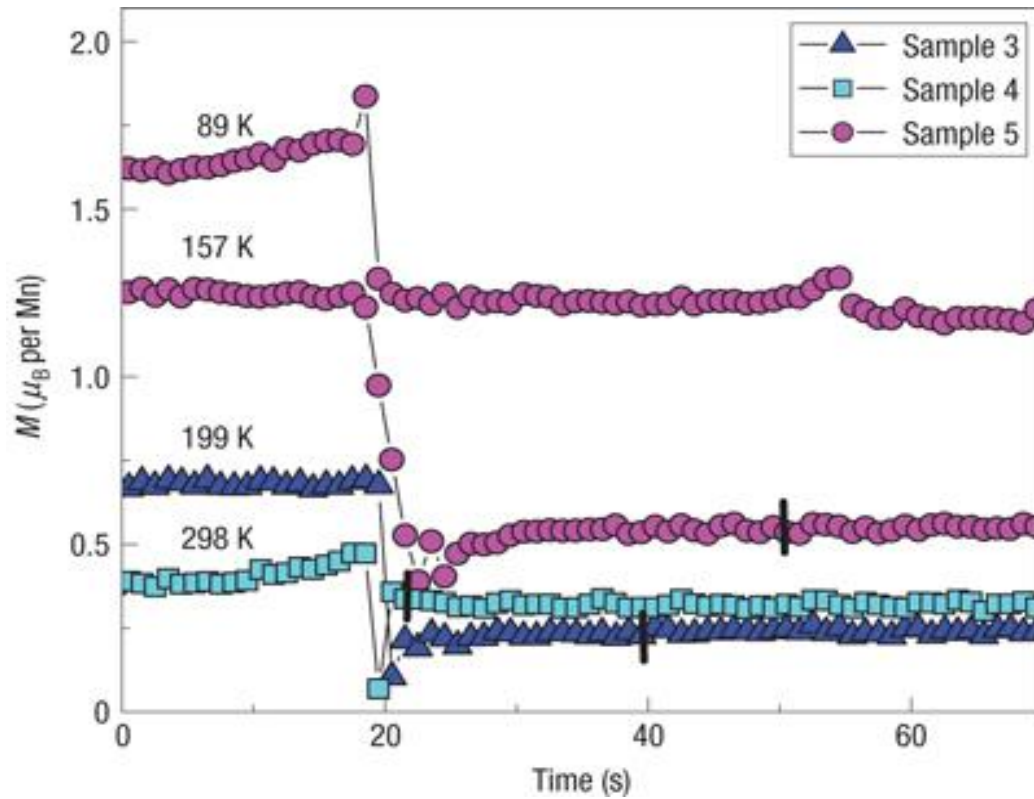


Figure 4.1: Large and sharp magnetic response due to an applied electric field. Each data sweep was carried out in 20 Oe, after an excursion in 8,000 Oe from 470 K, to 70 K, to the measurement temperature. The electric field was manually ramped over a period of approx 10 s while visually monitoring the VSM output in real time. The films were biased positive relative to the substrates, but reverse bias was used for sample 5 at 157 K. Transitions were recorded at 4 kV cm<sup>-1</sup> (sample 3), 10 kV cm<sup>-1</sup> (sample 4) and 6 kV cm<sup>-1</sup> (sample 5 at both 89 K and 157 K).<sup>51</sup>

Many other material combinations have been investigated for ME coupling effect recently. For example, Taniyama et al reported ME effect in Fe dots on BaTiO<sub>3</sub> substrates in the form

of changing magnetic domain pattern<sup>56</sup>. They observed a variation in the magnetization at the phase transition temperatures of BaTiO<sub>3</sub> substrate (from tetragonal to orthorhombic and from orthorhombic to rhombohedra structures). They found that when the sample is subjected to a thermal cycle between 300 and 150 K, the room-temperature magnetic domain structure changed significantly from an enclosed flux magnetic domain structure into a single-domain-like structure due to the strain at the Fe/BaTiO<sub>3</sub> interfaces in the heterostructures.

To study the room temperature ME coupling effect, others have explored the bipolar-electric-field control of nonvolatile magnetization in Co<sub>40</sub>Fe<sub>40</sub>B<sub>20</sub>/Pb(Mg<sub>1/3</sub>Nb<sub>2/3</sub>)<sub>0.7</sub>Ti<sub>0.3</sub>O<sub>3</sub> structure<sup>57</sup>. As reported by Zhang et al., a CoFeB film exhibited a magnetization hysteresis loop modified by an electric field (Figure 4.2) at room temperature, instead of the butterfly like curve commonly observed in piezo strain-mediated FM-FE structures<sup>58</sup>. In-situ investigations on the ferroelectric domains and crystal structures revealed that this is a combined effect of 109° ferroelastic domain switching and the absence of magnetocrystalline anisotropy in Co<sub>40</sub>Fe<sub>40</sub>B<sub>20</sub>. Other combinations of Ferromagnetic (FM)-Ferroelectric (FE) structures have also showed the coupling effect, including YIG / PMN-PT<sup>59</sup>, Terfenol-D/PMN-PT<sup>60</sup>, FeGaB/PZN-PT<sup>25</sup>, and Ni/BaTiO<sub>3</sub><sup>61</sup>. It must be noted that most of the previously reported systems are composed of a ferromagnetic metal and a piezoelectric oxide. The problem with such systems is the difficulty of achieving high quality metal-oxide interface.



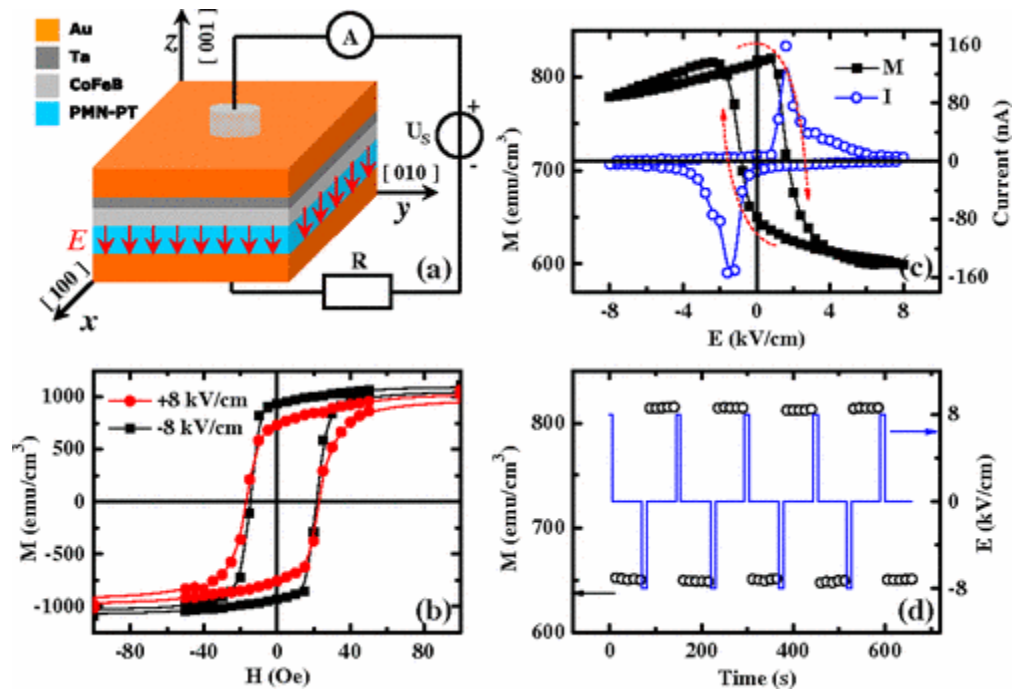


Figure 4.2: (a) Scheme of the sample and experimental configuration. (b) In-plane magnetic hysteresis loops under electric fields of  $+8 \text{ kVcm}^{-1}$  (circle) and  $-8 \text{ kVcm}^{-1}$  (square). (c) Electric-field tuning of the in-plane magnetization (square) and polarization current (open circle) recorded at the same time. (d) The repeatable high/low magnetization states (open circle) switched by pulsed electric fields (blue line).<sup>57</sup>

Therefore, all-oxide FM/FE systems with strong interface coupling are attractive for future investigation.  $\text{Sr}_2\text{CrReO}_6$  (SCRO) /  $\text{BaTiO}_3$  (BTO) (FM/FE) heterostructure is one of such system that has been investigated. Both the magnetic and transport properties of SCRO thin films under different strain conditions achieved through the phase transitions of BTO upon temperature variation have been reported<sup>24</sup>. Not only the ferroelectric constants change abruptly at these phase transitions accompanied by a thermal hysteresis, but also the

magnetic anisotropy and coercive fields of the SCRO film (Figure 4.3). There are abrupt jumps of up to 6.5% in the resistivity, as well as tremendous changes in the coercive field of more than 1.2 T as a function of temperature. These observations can be understood based on orbital ordering and the strong electronic correlations in double perovskite ferromagnets.

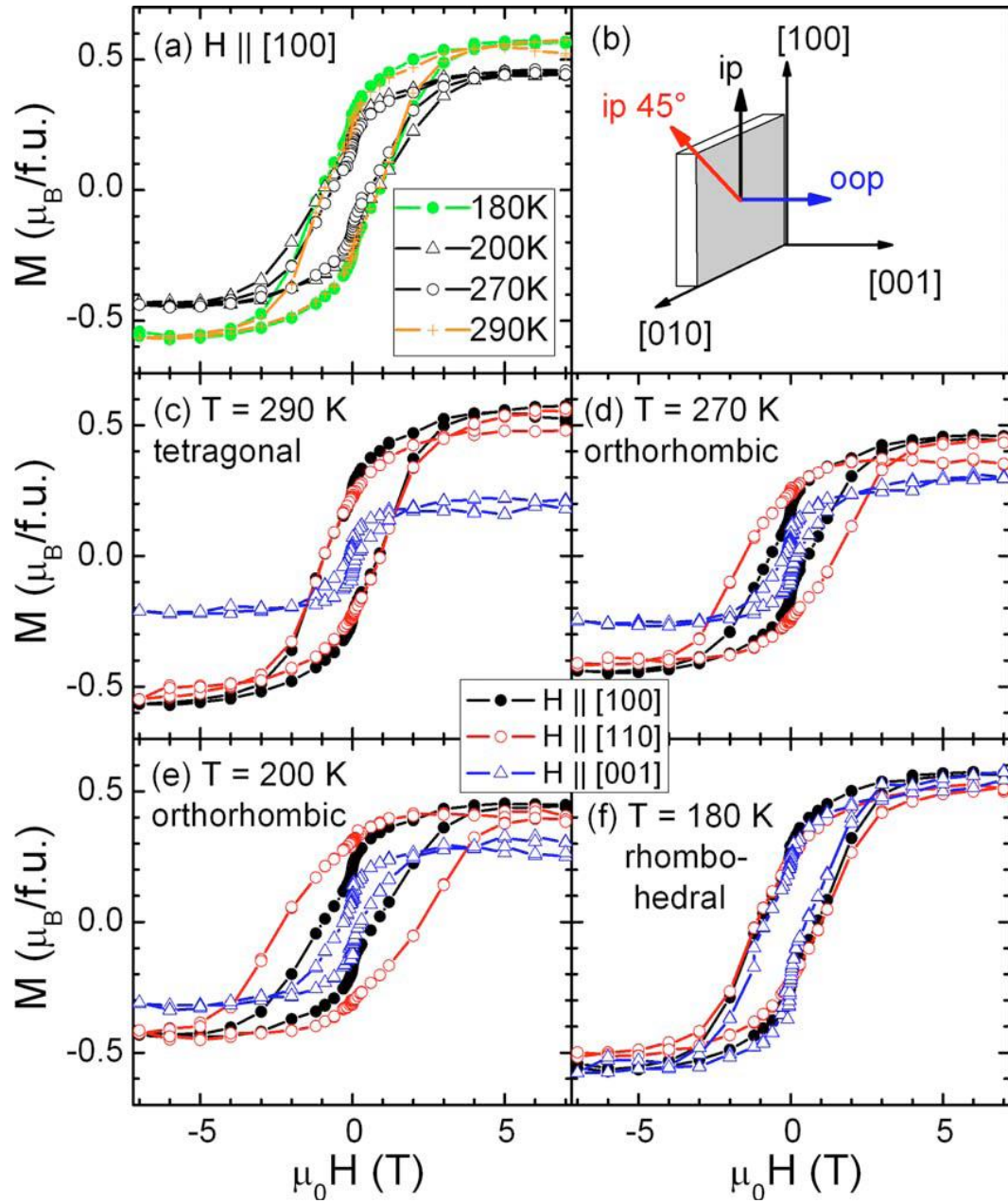


Figure 4.3: (a) Magnetic hysteresis loops measured at 290, 270, 200, and 180 K with the external magnetic field applied along BTO (100). (b) Illustration of the different orientations of the external field. In panels (c)–(f), hysteresis loops at specific temperatures for different orientations of the external magnetic field are shown.<sup>24</sup>

### **Pb(Mg<sub>1/3</sub>Nb<sub>2/3</sub>)O<sub>3</sub>-PbTiO<sub>3</sub> (PMN-PT)**

We have chosen an all-oxide FE-FM system in this study consisting of CoFe<sub>2</sub>O<sub>4</sub> and Pb(Mg<sub>1/3</sub>Nb<sub>2/3</sub>)O<sub>3</sub>-PbTiO<sub>3</sub> (PMN-PT). PMN-PT is a good piezoelectric material with extremely high piezoelectric coefficient ( $d_{33} = 2000 \text{ pC/N}$ )<sup>62</sup>. It means that the material will generate large strain under an electric field, which is important for the ME coupling effect in such a system. Moreover, PMN-PT has a relatively square ferroelectric loop, which means its remnant polarization is also large. Even after removing the electric field, PMN-PT can still maintain its strain state<sup>62</sup>. This provides the opportunity to investigate the coupling effect even without an in-situ electric field. The material we choose in our study is (1-x)Pb(Mg<sub>1/3</sub>Nb<sub>2/3</sub>)O<sub>3</sub>-xPbTiO<sub>3</sub> with  $30\% < x < 39\%$ , which is near its morphotropic phase boundary (MPB, Figure 4.4)<sup>63</sup>. It has not only an ultrahigh piezoelectric response, but also a complicated phase and ferroelectric domain structure<sup>64</sup>. According to the phase diagram, when  $x=0.32$ , the main phase in PMN-PT is a monoclinic phase of the Mc-type at the room temperature. When the temperature is raised, the tetragonal phase appears and finally turns to cubic when the temperature goes to above 410 K. It was demonstrated that when  $x$  is varied, the ferroelectric domains of PMN-xPT varies in length scale ranging from 40 nm to 0.1 mm<sup>64</sup>.

CoFe<sub>2</sub>O<sub>4</sub> is a well-known room temperature ferrimagnetic material. It was chosen as the FM component in this study because it is one of the oxides with a large magnetostriction coefficient ( $\lambda \sim -590 \times 10^{-6} \text{ kOe}^{-1}$ ) and its spinel structure is compatible with the perovskite structure<sup>65</sup>. To achieve good strain transfer, we aim to produce a coherent interface by growing an epitaxial film of CoFe<sub>2</sub>O<sub>4</sub> on single crystal PMN-PT. In this

material system, we investigate the effects of an external electric field on the magnetic properties and domain structures of  $\text{CoFe}_2\text{O}_4$ .

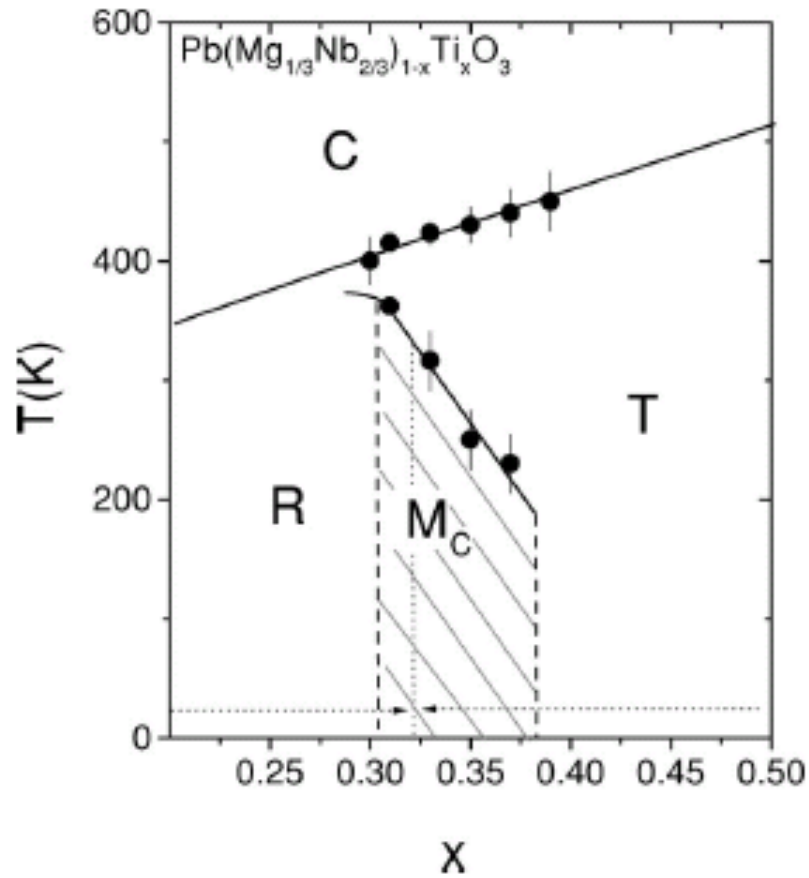


Figure 4.4: Phase diagram of PMN-xPT around the MPB. The solid line indicating the transition to the cubic phase is the average of the two temperatures from dielectric measurements. The symbols separating the  $M_c$  and  $T$  phases represent the temperatures at which the  $M_c$ - $T$  phase transition begins to take place.<sup>63</sup>

## **4.2 Growth and Characterizations of the CFO Epitaxial Thin Films on PMN-PT Substrates**

### **4.2.1 Experimental Procedure for the Film Growth**

Single crystal substrates PMN-PT with (001) orientation were used to grow  $\text{CoFe}_2\text{O}_4$  epitaxial thin films. First, the substrates were finely re-polished to reduce the roughness (to about 2 nm) of the growing surface. After that, they were cleaned in an ultrasonic bath with ethanol and acetone for a few minutes. This is because a clean, smooth surface will improve the quality of the epitaxy, which is critical to mediate strain across the interface. The target was also polished to remove the surface layer from previous depositions. The substrates and the target were then placed in the vacuum chamber and the chamber was pumped down to a base pressure of  $\sim 10^{-5}$  Torr. Subsequently, the oxygen flow was controlled to achieve the desired partial pressure, which is 10 mTorr in this work, for deposition. The substrate was heated to the temperature of 750 °C at the same time and was maintained at this temperature during deposition. The laser pulse frequency, duration and energy density were set to achieve optimal thickness and quality of the film. The thicknesses of our  $\text{CoFe}_2\text{O}_4$  films were controlled to be in the range 200 nm to 400 nm. After deposition, the samples were cooled down in the chamber at a rate of 5 °C per minute in a 760 Torr oxygen atmosphere.

The structure and phase purity of the films were examined using a high-resolution X-ray diffractometer (Shimadzu). Surface morphology was imaged using an atomic force microscope (AFM) (Asylum Research MFP-3D) with Pt/Ir coated tips.

The piezoelectric and ferroelectric properties of the PMN-PT substrate were measured using a probe station with a commercial ferroelectric tester (Radiant Technology, Precision Premier) after depositing the  $\text{CoFe}_2\text{O}_4$  film to ensure that the high temperature deposition process has not degraded the substrate properties. Silver paste was coated on two sides of the substrate as electrodes. The sample was soaked in silicon oil during the measurement.

#### **4.2.2 The structure of $\text{CoFe}_2\text{O}_4$ thin film on PMN-PT single crystal substrate**

The X-ray  $\theta$ - $2\theta$  diffraction pattern of the sample is shown in Figure 4.5. Only peaks from the (001) planes of the PMN-PT substrate and  $\text{CoFe}_2\text{O}_4$  film are observed, indicating that there is no secondary phase in the film. The lattice parameter of PMN-PT is  $a=b=4.022 \text{ \AA}$ <sup>66</sup>, which is smaller than half of the pseudocubic bulk lattice parameter of  $\text{CoFe}_2\text{O}_4$   $a=8.392 \text{ \AA}$ <sup>65</sup>. The reported critical thickness for dislocation formation in this system is around 4 nm<sup>67</sup>. Since the thickness of our film is much larger than the critical value, we conclude that the mismatch strain should be relaxed in the film. The out-of-plane lattice parameter of  $\text{CoFe}_2\text{O}_4$  calculated from this diffraction data is  $8.365 \text{ \AA}$ , which is slightly smaller than the bulk value of  $8.392 \text{ \AA}$ . This indicates a possibility of a small tensile in-plane strain in the film.

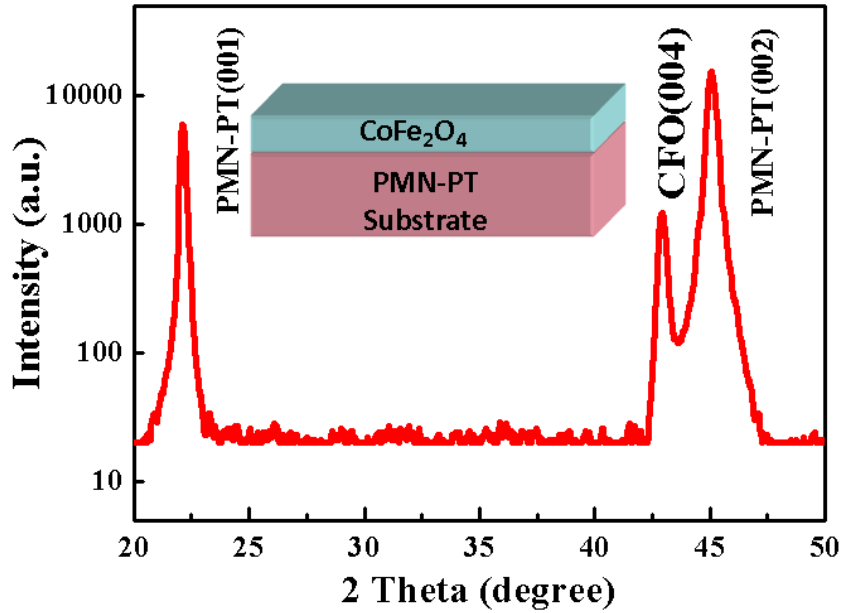


Figure 4.5: X-ray diffraction pattern of the as-grown  $\text{CoFe}_2\text{O}_4/\text{PMN-PT}$  heterostructure; the inset is the schematic description of the sample.

We have also conducted reciprocal space mapping around the (202) peak (Figure 4.6) to further investigate the crystal structure. The stronger peak is the (202) peak of the PMN-PT substrate. The other is from the  $\text{CoFe}_2\text{O}_4$  film. The in-plane lattice parameter of the  $\text{CoFe}_2\text{O}_4$  film calculated from this mapping is 8.405 Å. This lattice parameter is larger than the bulk value, confirming the existence of an in-plane tensile strain. We conclude that this strain could be due to the difference between the thermal coefficients of the film and substrate. (The coefficients of thermal expansion (CTE) of  $\text{CoFe}_2\text{O}_4$  and PMN-PT are  $11.8 \times 10^{-6}$  and  $8 \times 10^{-6}$ , respectively<sup>68,69</sup>.)



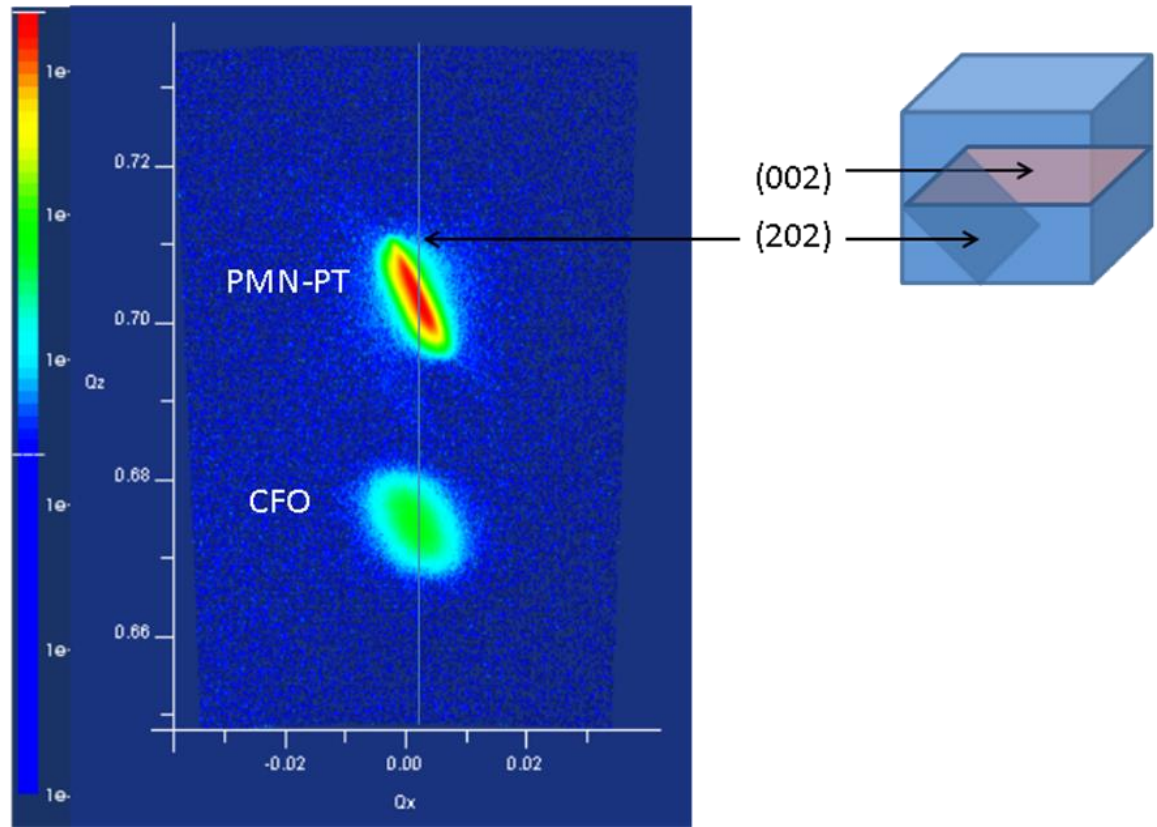


Figure 4.6: Reciprocal space mapping of the epitaxial  $\text{CoFe}_2\text{O}_4$  film on (001) - cut PMN-PT substrate around the (202) peak.

The high crystallinity and epitaxial structure were also confirmed by our TEM results. We prepared the cross-section PMN-PT/ $\text{CoFe}_2\text{O}_4$  samples in the following way: The substrate with  $\text{CoFe}_2\text{O}_4$  film was cut into several  $1 \times 5 \times 1.5\text{mm}$  pieces. Two of these pieces were glued together (with  $\text{CoFe}_2\text{O}_4$  film face to face) by epoxy. Then the cross-section of the sample was ground and polished to reduce the thickness to a very small value. After that, the sample was subjected to dimple and ion milling. Finally, an electron transparent area of the cross-section of PMN-PT substrate and  $\text{CoFe}_2\text{O}_4$  thin film was attained for TEM analysis.

Figure 4.7 are the cross-section view TEM images of the sample. It shows that the thickness of the  $\text{CoFe}_2\text{O}_4$  thin film is about 80 nm. There are some inhomogeneities in the film due to the processing damage. The selected area diffraction pattern reflects the average structure around the interface. As shown in Figure 4.7(b), there is a set of  $\text{CoFe}_2\text{O}_4$  spots in addition to the PMN-PT spots from the single crystal substrate, which indicates that the film follows the (100) direction of the substrate with slightly bigger lattice. The high resolution TEM image of the interface area is showed in Figure 4.7(c). It is noted that there is a very thin interface layer followed by pure  $\text{CoFe}_2\text{O}_4$  phase. The presence of the interface layer was not detected by high resolution XRD but that could be because it was too thin. The lattice parameters indicate that this epitaxial  $\text{CoFe}_2\text{O}_4$  film experiences a small tensile strain from the epitaxy with the substrate.

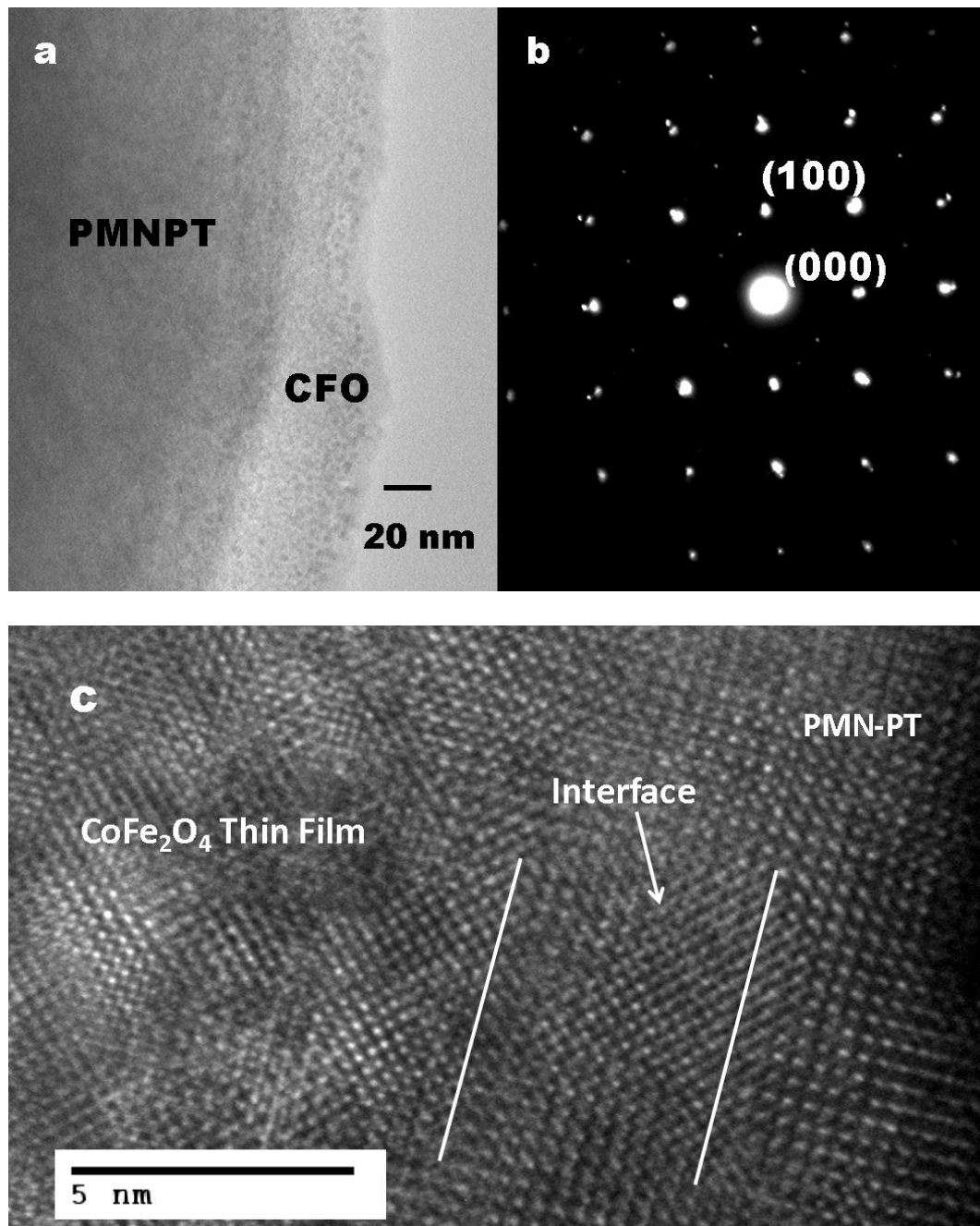


Figure 4.7: (a) Cross-section view TEM image taken from the PMN-PT/CoFe<sub>2</sub>O<sub>4</sub> sample. (b) Selected area diffraction pattern from the same sample. (c) High resolution TEM image of the interface area between the PMN-PT and CoFe<sub>2</sub>O<sub>4</sub>.

### 4.3 Electrical and Magnetic Properties of the CoFe<sub>2</sub>O<sub>4</sub> /PMN-PT Composite

#### 4.3.1 Ferroelectric properties of CoFe<sub>2</sub>O<sub>4</sub>/PMN-PT thin film composite

After depositing CoFe<sub>2</sub>O<sub>4</sub> films onto the PMN-PT substrate at high temperature, the ferroelectric hysteresis loop of the PMN-PT is checked again. It shows a square loop with a remnant polarization of  $P_r = 30 \mu\text{C}/\text{cm}^2$  as shown in Figure 4.8. There is no loss evident compared to the pure substrate. This confirms that the PMN-PT still retains its ferroelectric quality. It also implies that the high temperature deposition process of CoFe<sub>2</sub>O<sub>4</sub> film has not affected the ferroelectric property of the PMN-PT substrate. This standard hysteresis loop is important in this study because the subsequent loops obtained in other samples will be compared to this standard loop, particularly the critical points of this loop, such as the remnant polarization and coercivity.

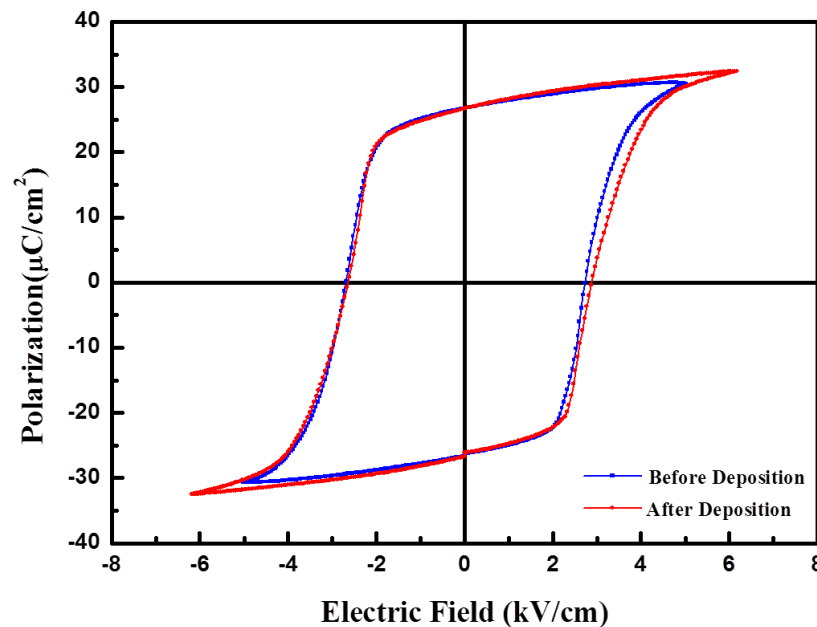


Figure 4.8: Polarization vs. electric field hysteresis loop of the PMN-PT substrate before and after CoFe<sub>2</sub>O<sub>4</sub> deposition.

#### 4.3.2 Piezoelectric properties of the PMN-PT after CoFe<sub>2</sub>O<sub>4</sub> deposition

The piezoelectric property of the substrate is shown in Figure 4.9: The strain vs. electric field hysteresis loop of the PMN-PT substrate before and after CoFe<sub>2</sub>O<sub>4</sub> deposition. A strain as large as 0.22% is generated under an electric field of 6 kV/cm, indicating that the  $d_{33}$  value is about 1490 pm/V. From this loop, we also notice that after applying the electric field, a remnant strain of about 0.13% remains even when the electric field becomes zero. This large remnence indicates that in later studies large electric fields needs not to be applied during the MFM scanning as the remanant field itself might be adequate. Such a large strain from the PMN-PT substrate shown here is expected to lead to significant change in the magnetic response of the CoFe<sub>2</sub>O<sub>4</sub> film through the converse magnetostrictive effect.

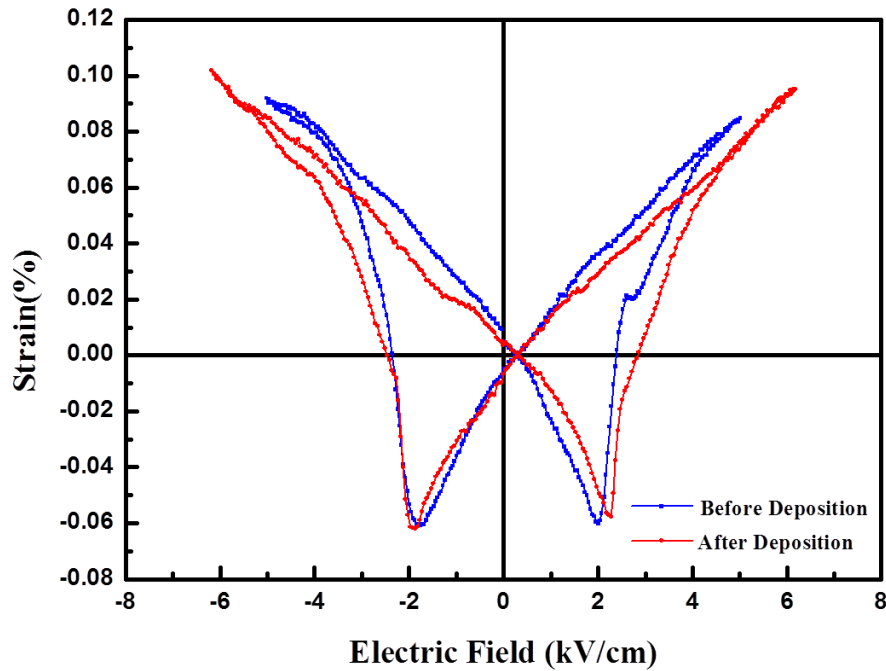


Figure 4.9: The strain vs. electric field hysteresis loop of the PMN-PT substrate before and after CoFe<sub>2</sub>O<sub>4</sub> deposition.

### 4.3.3 Magnetic properties of the $\text{CoFe}_2\text{O}_4$ /PMN-PT composite

The in-plane and out-of-plane magnetization-field (M-H) hysteresis loops along the  $\langle 100 \rangle$  and  $\langle 001 \rangle$  directions of the  $\text{CoFe}_2\text{O}_4$  film are shown in Figure 4.10: The in-plane and out-of-plane magnetization-field hysteresis loops of  $\text{CoFe}_2\text{O}_4$  film on PMN-PT. The saturation magnetization is about  $1.60 \times 10^5$  A/m, smaller than bulk value. A weak anisotropy is observed between the in-plane ( $\langle 100 \rangle$  direction) and out-of-plane ( $\langle 001 \rangle$  direction) magnetic responses, where the remanence and coercivity are a bit higher along the out-of-plane  $\langle 001 \rangle$  direction.

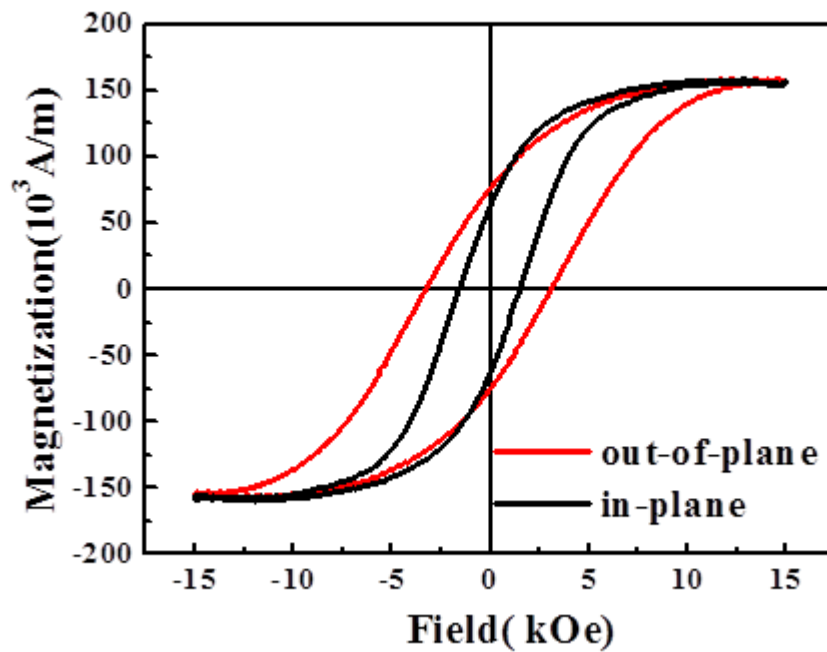


Figure 4.10: The in-plane and out-of-plane magnetization-field hysteresis loops of  $\text{CoFe}_2\text{O}_4$  film on PMN-PT.

## **4. 4 Magnetoelectric coupling in the $\text{CoFe}_2\text{O}_4$ /PMN-PT composite**

### **4.4.1 Strain effect on the magnetic domains of the $\text{CoFe}_2\text{O}_4$ film**

#### **Thermally-induced strain effect on the magnetic domains:**

First we look at the thermally induced strain effect on the magnetism of the  $\text{CoFe}_2\text{O}_4$  film. The sample was mounted on a heating stage in the AFM system. The topography and magnetic domain structures of the  $\text{CoFe}_2\text{O}_4$  film were taken respectively first and (the setup is shown in Figure 4.11 ). The images shown in Figure 4.12 are those of the sample before heating and these are used as the reference for subsequent images obtained at higher temperatures. Then the sample was heated to 250 °C which is higher than the phase transition temperature of PMN-PT single crystal ( $\sim 177^\circ\text{C}$  according to the study of Noheda et al)<sup>63</sup>. The sample was held at the high temperature for a few minutes, then cooled down to room temperature. The topography and magnetic domain structures of the  $\text{CoFe}_2\text{O}_4$  film were taken again at the same location, as shown in Figure 4.12. Note that some particles appear on the sample surface after the heat treatment, but the topographic features allow us to confirm that this is the same location on the sample.

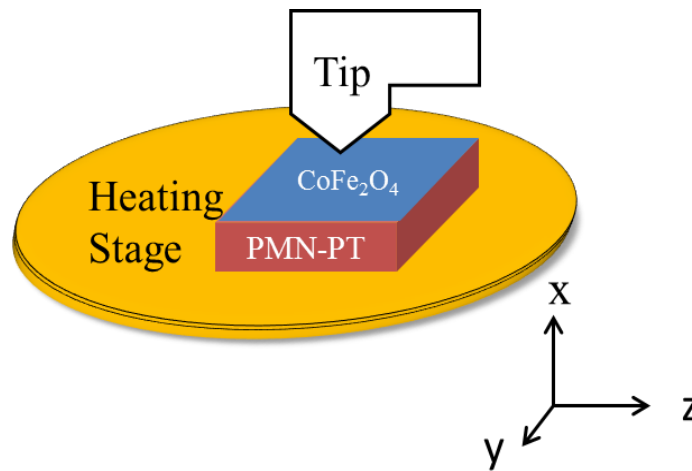


Figure 4.11: Schematic description of the experimental setup for plan view MFM imaging of the substrate on heating stage.

In the MFM images, the bright and dark regions represent repulsive (magnetization pointing up) and attractive (magnetization pointing down) magnetostatic forces between the tip and sample, respectively. Compare the MFM images of the film before and after heating (Figure 4.12). It is clear that the contrast increases after the heat treatment. More importantly, domain structure clearly changes at some locations. It indicates that the magnetism was affected during the heating and cooling cycle, likely due to the strain induced during the phase transition of the PMN-PT substrate upon the thermal cycle. However, such thermally-induced changes are not controllable since the ferroelectric/ferroelastic domain structures of the substrate after heating cannot be determined precisely. The results indicate that strain-mediated coupling exists in this system, but further experiments are needed to better understand the process.



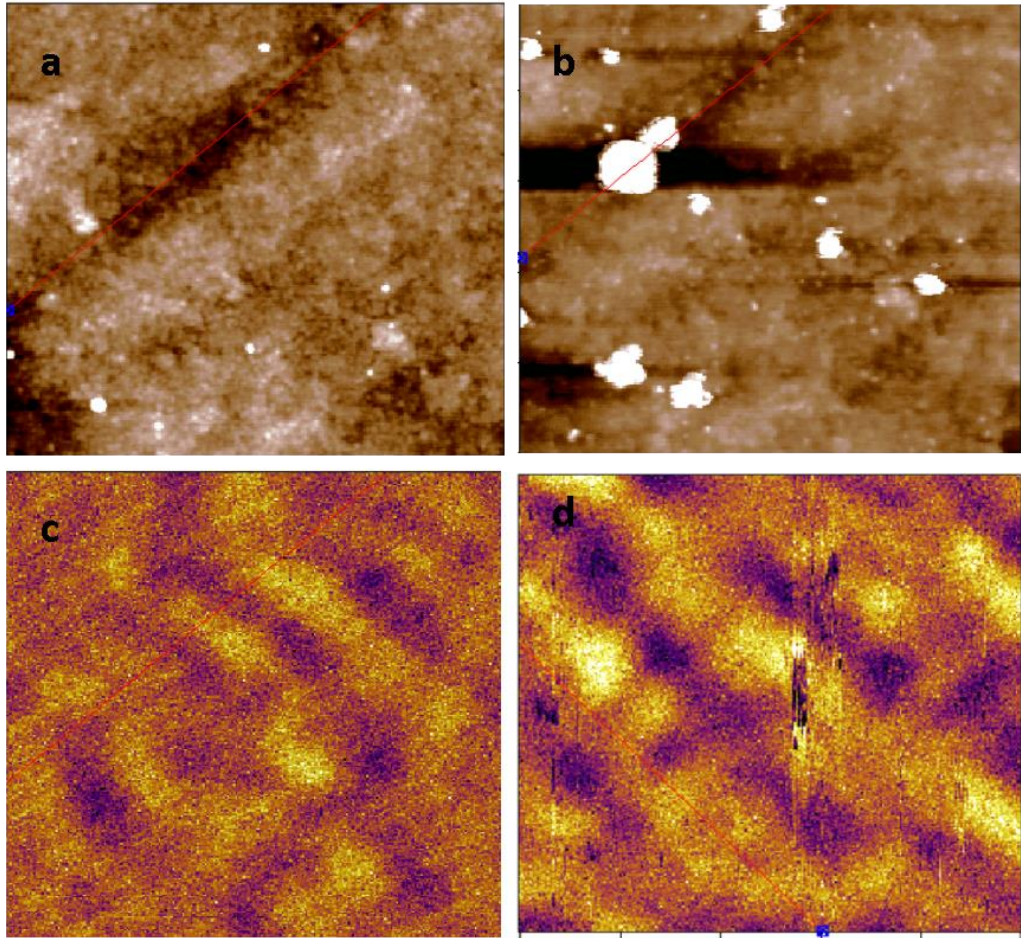


Figure 4.12: (a) and (c) Topography and magnetic domain structures of the  $\text{CoFe}_2\text{O}_4$  film before heating treatment, respectively. (b) and (d) The Topography and magnetic domain structures of the  $\text{CoFe}_2\text{O}_4$  film at the same location after heat treatment, respectively.

### Electric-field-induced strain effect on the magnetic domains:

To investigate the ME coupling in the  $\text{CoFe}_2\text{O}_4/\text{PMN-PT}$  system in a more controllable manner, we investigate the effects of electric-field-induced strain on the magnetic domains of the  $\text{CoFe}_2\text{O}_4$  film. The sample was first set up with the  $\text{CoFe}_2\text{O}_4$  thin film facing up for MFM scanning as shown in Figure 4.13. The as-deposited sample was cut into  $1\text{cm} \times 1\text{cm} \times 5\text{cm}$  strips. An external electric field was applied between the two sides of the strip through wires connected with silver paste.

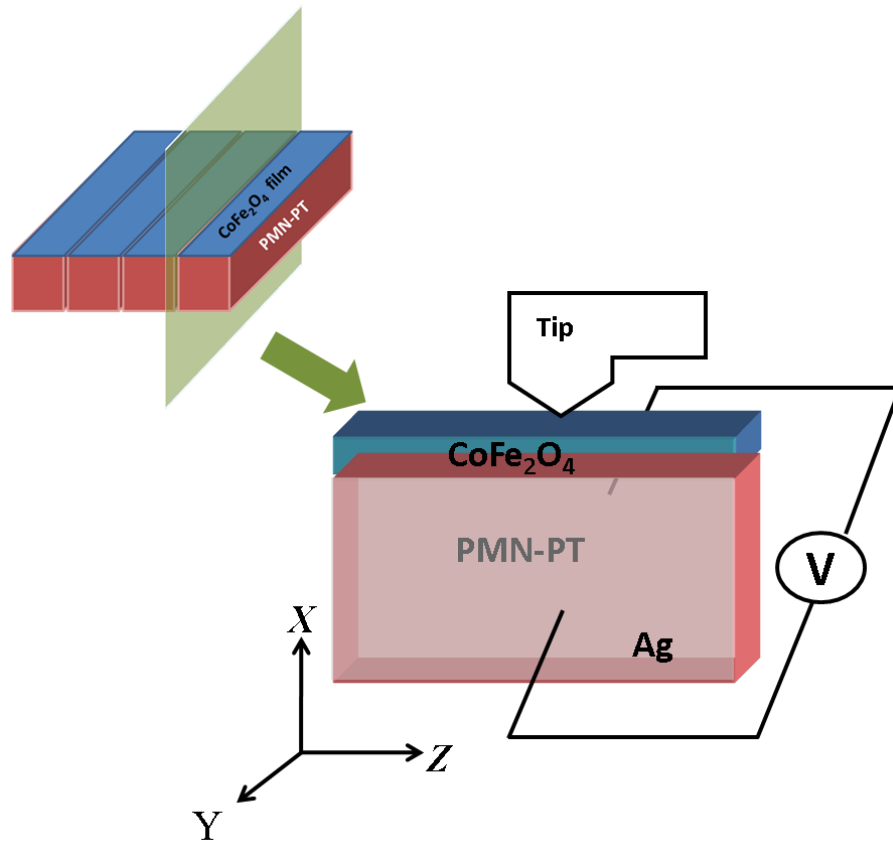


Figure 4.13: Schematic description of the experimental setup for plan view MFM imaging after various electric fields are applied to the substrate.

Before applying any electrical field to the substrate, the topography and magnetic domain images of the film were taken and shown in Figure 4.14. The topographic features would be used as the reference to relocate the MFM tip to the same position of the sample for magnetic domain imaging during the subsequent imaging.

Because of the large voltage needed to switch the polarization of the PMN-PT (1 cm thick in this case), the sample has to be immersed in Si oil, which prevents in-situ MFM imaging. We thus pick four critical points along the hysteresis loop for MFM domain imaging. First, an electric field of 9.2 kV/cm was applied to the PMN-PT substrate in the y direction to pole it to the saturation state. The field was then turned off and the substrate relaxed to the positive remnant state. The magnetic domain image at this point is shown in Figure 4.16(b). After that, a negative field of -4.6 kV/cm (close to the coercive field) was applied as shown in Figure 4.14(f), which should then depolarize the substrate. The magnetic domain structure was again obtained at the same position. Subsequently, the substrate was poled to the negative saturation state and relaxed. Finally, a positive bias equal to the coercive field was applied. After each field was applied, magnetic domain structures were obtained at the same location.

Comparing the MFM images shown in Figure 4.14, it is clear that little differences can be observed except for the initial state. Further examination reveals that, when applying the electric field, the PMN-PT is polarized along the y direction (Figure 4.13), leading to a tensile strain along this direction. The strain is transferred to the film through the interface.

However, since the PMN-PT crystal is only poled along the y direction, the anisotropy raised from the polarization will mostly exist between the y and z directions. The out-of-plane (x-direction) of the  $\text{CoFe}_2\text{O}_4$  film may not be affected. Although, the strain will generate some influence on the magnetization because of the negative magnetostrictive coefficient of  $\text{CoFe}_2\text{O}_4$ , this coupling effect could not be well reflected in the MFM images along the x direction. In order to better observe the magnetoelectric coupling effect, we must seek a different way to do the experiments. Therefore, we prepare the cross section samples, in which the z direction will be set for MFM scanning instead of x direction.

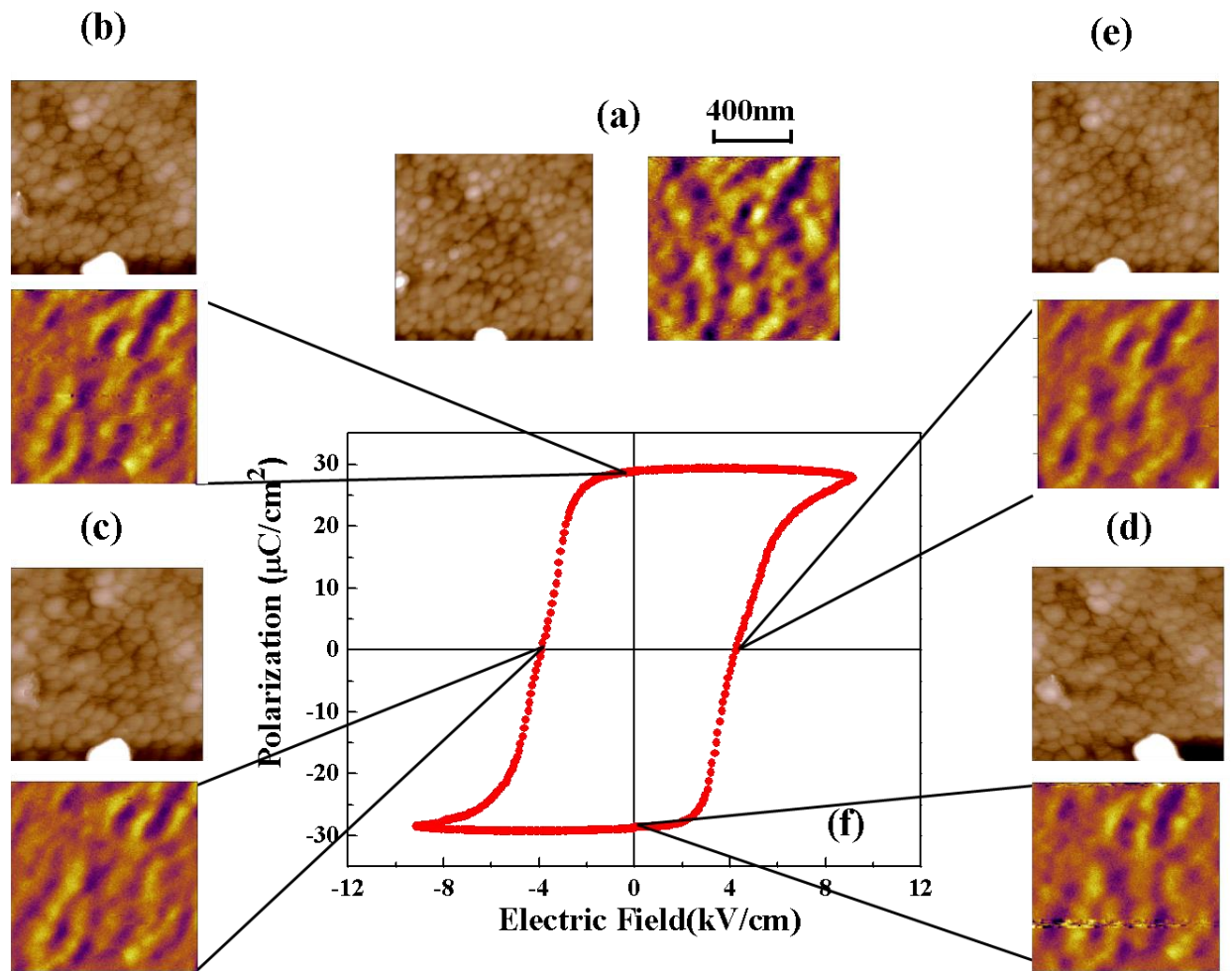


Figure 4.14: (a-e) Topography and magnetic domain structures looking from the x-axis of CoFe<sub>2</sub>O<sub>4</sub> thin film at different states of the ferroelectric switching of the PMN-PT substrate. (a) Initial state; (b) positive remnant state; (c) depolarized state; (d) negative remnant state and (e) depolarized state. (f) The polarization vs. electric field hysteresis loops of the PMN-PT substrate.

To further study the electrical-field-induced changes in the magnetic domain structures of CoFe<sub>2</sub>O<sub>4</sub>, cross section samples were prepared. First, plate shaped thin film composite samples were cut into some 1 mm wide strips. Secondly, two of these strips were picked and

glued together with the films face-to-face using epoxy. Thirdly, the side surface was polished. And lastly, the z (as shown in Figure 4.15) surface was finely polished for MFM study. The experimental setup is schematically shown in Figure 4.15. The sample was laid on the stage with z direction straight up and scanned the top surface using Co coated magnetic tips. The external voltage will be applied to the sample along the y direction.

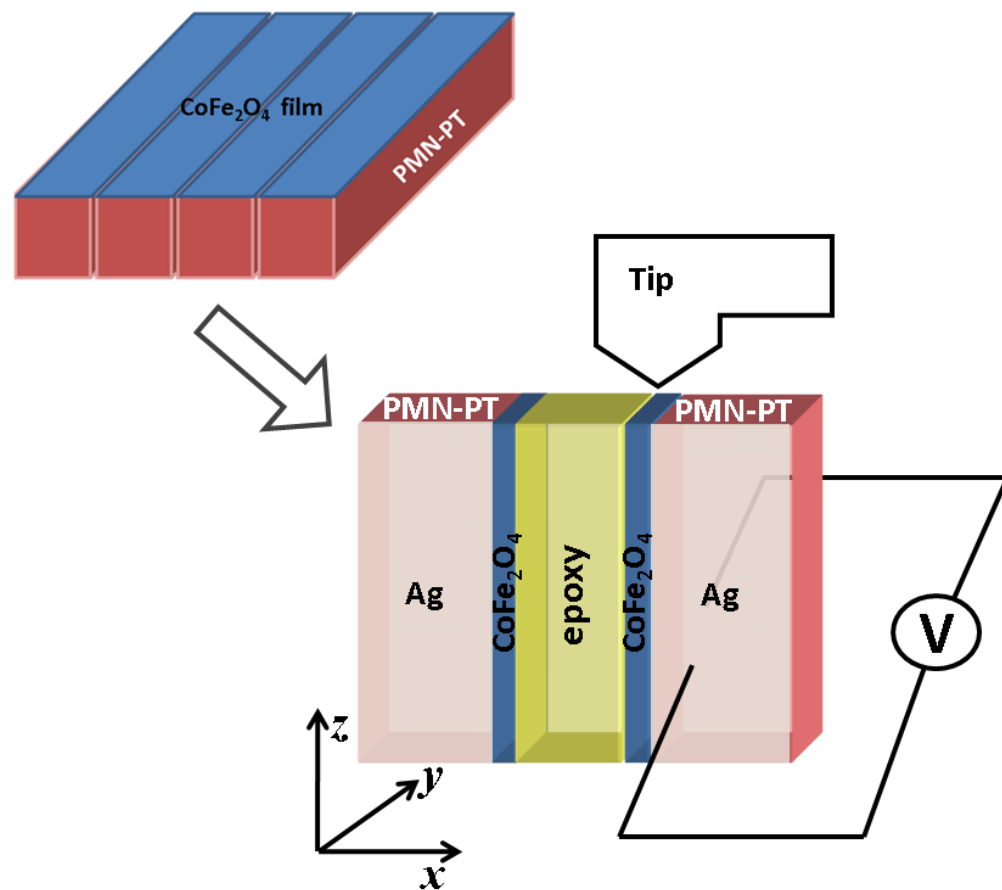


Figure 4.15: Schematic description of the experimental setup for cross section view measurements.

Like the previous experiment design, the topography and magnetic domain images of the cross section of the film were collected before applying the electrical field to the substrate. These images are shown in Figure 4.16(a). The interfaces between the epoxy, the  $\text{CoFe}_2\text{O}_4$  film and the PMN-PT substrate are clearly identifiable in the topography image: the left white part is the epoxy; the middle strip is the  $\text{CoFe}_2\text{O}_4$  film and the right part is identified as the PMN-PT substrate. Using this topographic feature as a reference, we can locate the MFM tip to the same location of the sample for magnetic domain mapping after applying electric fields to the substrate.

In this experiment, an electric field of 9.2 kV/cm was first applied to the PMN-PT substrate to pole it to the saturation state, and then relaxed to the positive remnant state. The magnetic domain image of the film was taken at the same location showing (Figure 4.16(b)) an enhanced contrast, indicating increased remnant magnetization along the tip direction. As we discussed above, the PMN-PT is polarized along the  $y$  direction after applying the electric field (Figure 4.15), leading to a tensile strain along this direction which is transferred to the film. Anisotropy will emerge between the  $y$  and  $z$  directions. Due to the negative magnetostrictive coefficient of  $\text{CoFe}_2\text{O}_4$ , the  $y$  direction would become a hard axis as compared with the  $z$  direction after the poling of the substrate (elongated, generating a tensile strain on the film along this direction). Hence, we can observe an enhancement in contrast along  $z$  direction as shown in Figure 4.16 (b). Subsequently, a negative electric field of -4.6 kV/cm (close to the coercive field as shown in Figure 4.16(f)) was applied to the PMN-PT substrate to depolarize it. The magnetic domain structure obtained is clearly altered again as shown in Figure 4.16 (c) where the contrast is reduced and domain structure

is changed at certain locations. By poling the substrate to the negative saturation state (apply -9.2 kV/cm field, Figure 4.16(d)), the magnetic domain contrast is altered again in Figure 4.16(d), becoming similar to that of the positively poled state of Figure 4.16(b). This is expected because the strain experienced by the  $\text{CoFe}_2\text{O}_4$  film at these remnant states is the same even though the substrate polarizations are in opposite directions. Finally, a positive bias equals to the coercive field was applied to the PMN-PT and returned the film magnetization to a state (Figure 4.16 similar to that indicated in Figure 4.16(c). This reversible ME coupling was repeatable in several samples. However, the changes to the domain contrast tend to diminish after several cycles of electrical poling. This could indicate a deterioration of the elastic coupling at the interface.



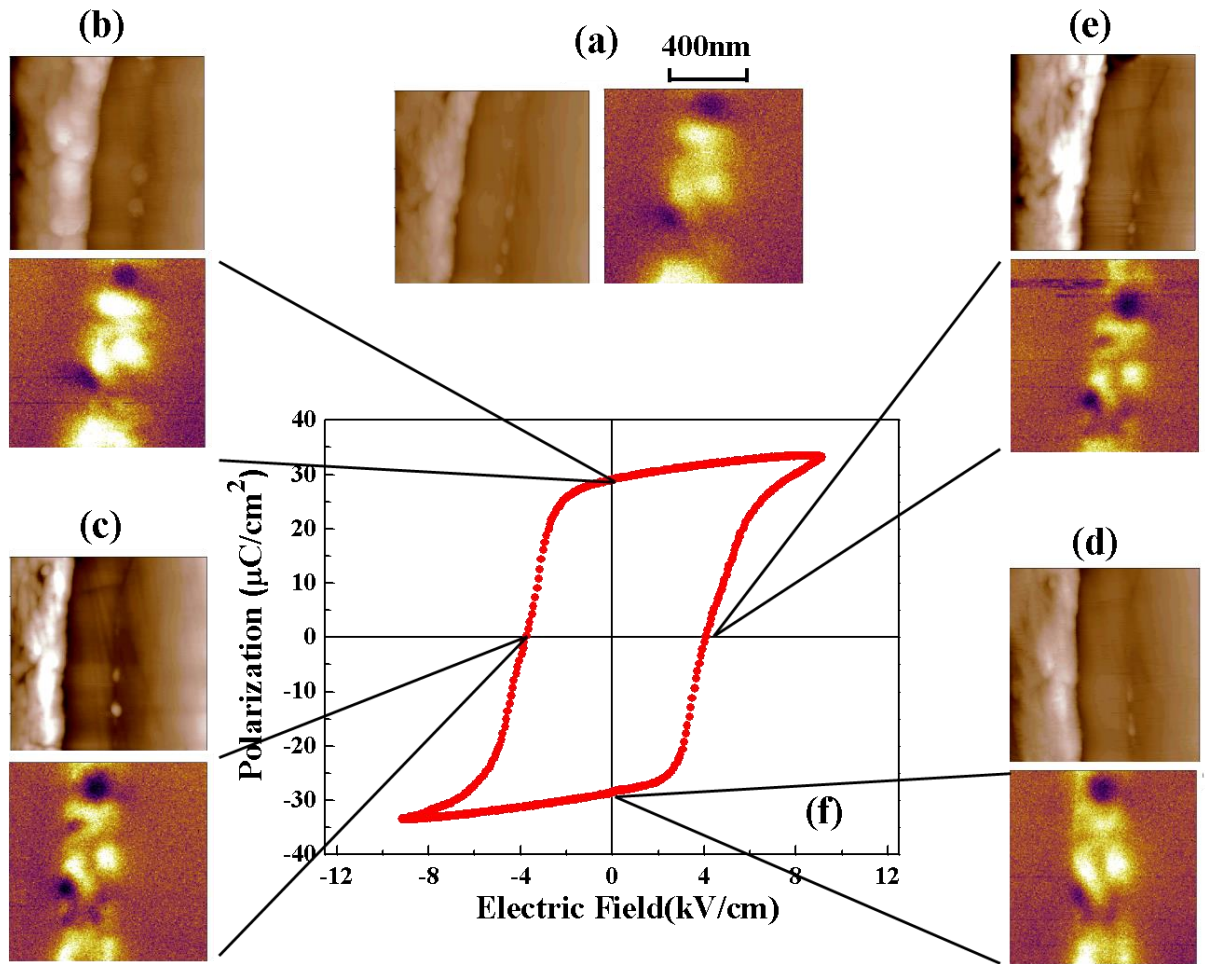


Figure 4.16: (a-e) Topography and magnetic domain structures of the cross section surface (z-axis) of  $\text{CoFe}_2\text{O}_4$  (The thin film thickness=200 nm) at different states of the ferroelectric switching of the PMN-PT substrate. (a) Initial state; (b) positive remnant state; (c) depolarized state; (d) negative remnant state and (e) depolarized state. (f) The polarization vs. electric field hysteresis loops of the PMN-PT substrate.

#### 4.4.2 Magnetoelectric coupling effect in the composite

To confirm the MFM observations and to correlate them with macroscopic magnetic property of the sample, we measured the M-H hysteresis loops after applying electric field to the substrate. A 1 mm  $\times$  5 mm strip of the sample was used. The substrate was poled in the y (with the short distance between the electrodes) direction as shown in Figure 4.17(a). Like in the previous experiments, the M-H curves were measured along all three directions under three conditions of the substrate: the initial state, the remnant state (Pr) after saturation, and the depolarized state. The results are shown in Figure 4.17(b) to (d).

Figure 4.17(d) shows the measurements along the z direction of this sample, which correspond to the MFM images shown in Figure 4.16. It's noted that there is small enhancement in the remnant magnetization when the PMN-PT substrate is at its remnant polarization state. Upon depolarization, the M-H loop almost returns to the initial curve in the z direction. This macroscopic magnetic response is consistent with the microscopic domain evolution under electric field displayed in Figure 4.16. Increased magnetization is exhibited together with enhanced contrast of magnetic domain pattern at remnant state. The M-H loops obtained along the x and y directions are shown in Figure 4.17(b) and (c). Note that the different polarization states of the substrate have negligible effect on the magnetic loops in the out-of-plane x direction. However, a significant effect on the magnetic loop was observed in the in-plane y direction at different polarization states compare to the other two directions. The different strain states reflected are consistent with the observed changes in the M-H loops along the three directions. Similar results were obtained when other samples were examined. Thus, these results are reproducible and reliable.

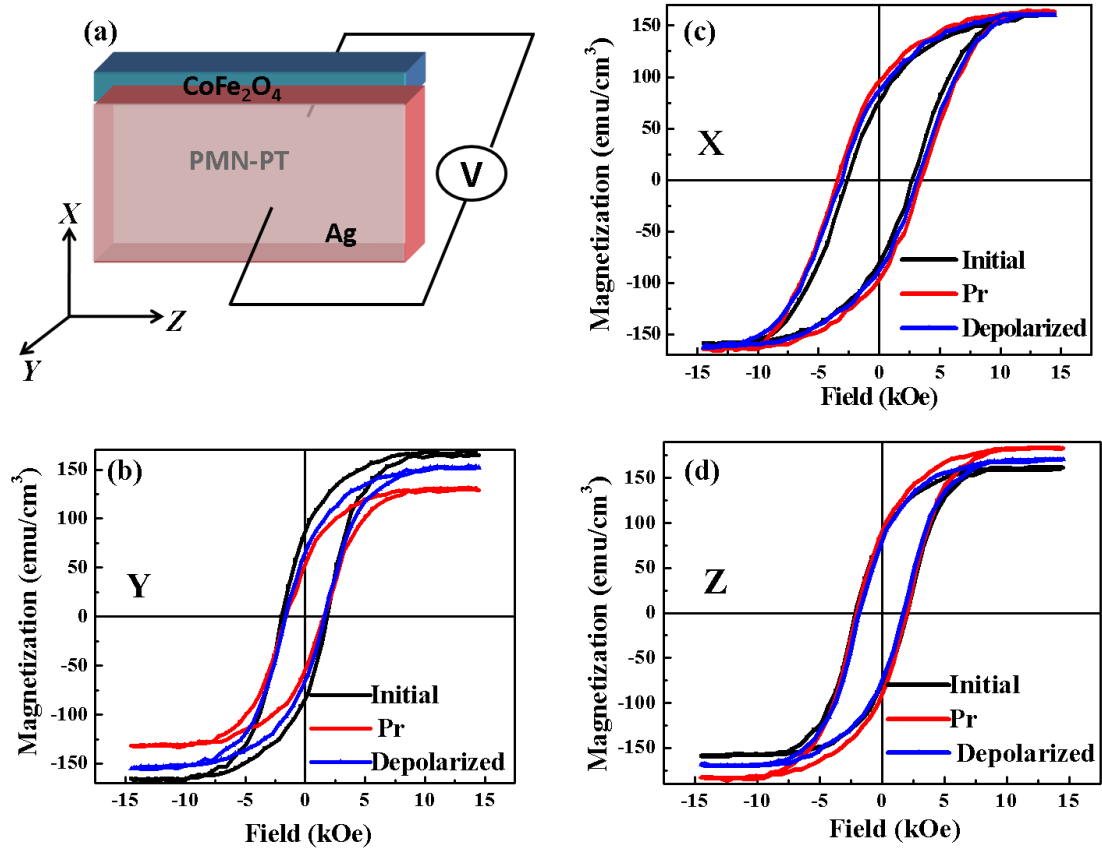


Figure 4.17: (a) Schematic description of the sample orientation. (b-d) The magnetization-field hysteresis loops of the  $\text{CoFe}_2\text{O}_4$  film on PMN-PT substrate along the x (b), y (c) and z (d) directions at different polarization states.

#### 4.4.3 Proposed model of magnetoelectric coupling effect in the composite

The results from MFM images and magnetization loops are all consistent with piezoelectric strain induced anisotropy change in the  $\text{CoFe}_2\text{O}_4$  film. For example, when an electric field is applied in y direction, the strain is generated in the PMN-PT substrate along y and z directions. The strain is transferred to the  $\text{CoFe}_2\text{O}_4$  film and causes corresponding changes in the remnant magnetization. As shown in Figure 4.16(b), the enhanced contrast of magnetic domains observed in MFM image along z direction view reflects an enhancement of the magnetization along this direction, which is confirmed by the M-H loops shown in the Figure 4.17(b).

The schematic diagram shown in Figure 4.18 describes the model qualitatively. The dot line blocks represent the initial state of the sample shape while the color filled ones represent the samples after electric field is applied. As shown in Figure 4.18(b), after applying the electric field, the electric dipoles of the single crystal are all aligned along the y direction from the initial state. The PMN-PT substrate is elongated along the y direction due to the piezoelectric effect and shrank in the z direction relatively. The resulting tensile strain in y direction is transferred to the  $\text{CoFe}_2\text{O}_4$  film through the epitaxial interface. Because of the negative magnetostrictive coefficient of  $\text{CoFe}_2\text{O}_4$ , this superposed strain in the y direction should bring about a corresponding decrease in the remnant magnetization. These proposed effects are confirmed by magnetic domain mapping and M-H measurements. When the depolarizing electric field close to the coercive field is applied, some of the electric dipoles turned to opposite direction in PMN-PT substrate as shown in Figure 4.18(d). The shape of the sample returns to the state which is close to the initial one. The stain induced with the

coupling effect also turn back to a state similar to the initial one. Since PMN-PT has a larger  $d_{33}$  than  $d_{31}$ , the strain and shape anisotropy generated along y direction is larger than that along z direction. Furthermore, the effect in  $\text{CoFe}_2\text{O}_4$  along x direction is even smaller than that along the z direction. From the remnant polarization state to the depolarized state, the evolution of the ME coupling induced effect in PMN-PT/  $\text{CoFe}_2\text{O}_4$  is repeated.

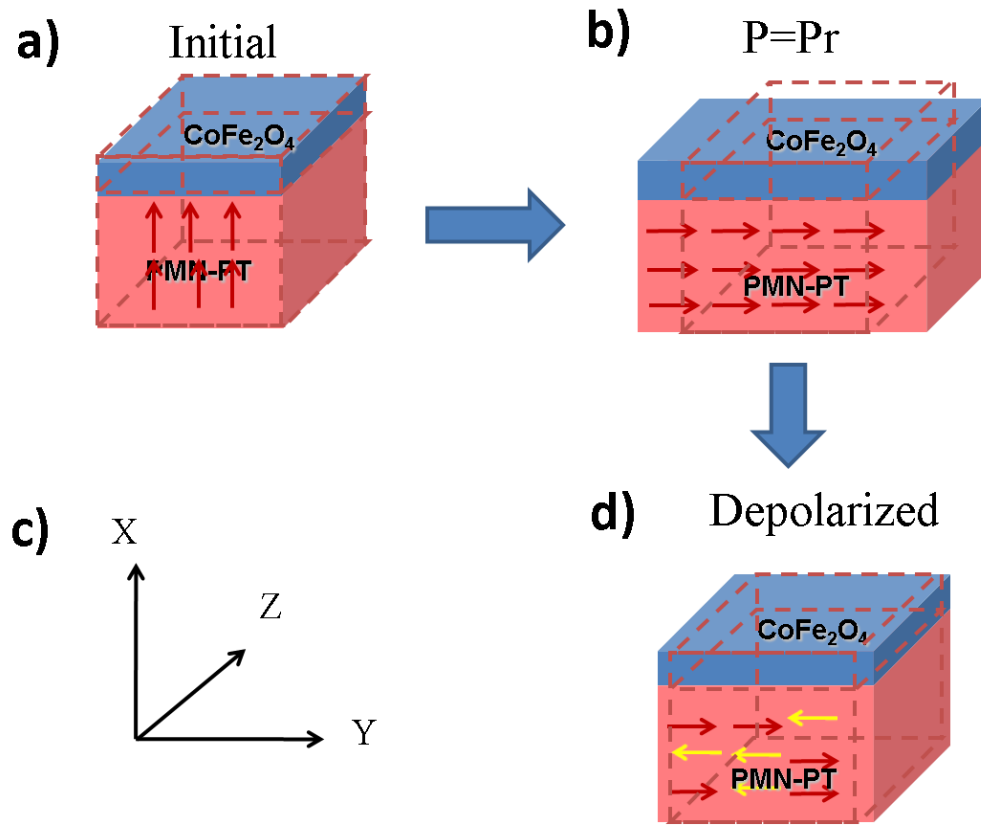


Figure 4.18: (a), (b) and (d) Schematic diagrams of proposed effect when the substrate is at different states along the P-E hysteresis loop. (c) The orientation of the sample with respect to the previous experiments.

## Chapter 5 : Summary and Future Work

In conclusion, we have designed, produced and investigated potential multiferroic composite systems where the substrate clamping effect has been eliminated. In the bulk composites BaTiO<sub>3</sub>-CoFe<sub>2</sub>O<sub>4</sub> (weight ratio 70%:30%) system, we synthesized and densified the samples using conventional sintering and SPS techniques. In the magnetic film on active piezoelectric substrate system, the ferrimagnetic CoFe<sub>2</sub>O<sub>4</sub> film was deposited on piezoelectric PMN-PT single crystal substrate by PLD. The structure and properties of these composite systems were investigated with particular emphasis on the mechanism of the ME coupling effect in the second system.

1. In the bulk composite BaTiO<sub>3</sub>-CoFe<sub>2</sub>O<sub>4</sub> system:

- Dense bulk multiferroic composites were produced through both conventional and SPS sintering at the temperature of 1200 °C and 1000 °C, respectively. Structural analyses and various characterizations showed that SPS is a superior method to obtain highly dense bulk composites without any interface reactions, quickly.
- The magnetic coercivity of the composite decreases while saturation magnetization increases after sintering. SPS samples consistently exhibit larger saturation magnetization than those sintered by conventional method. This is attributed to the lower porosity and the finer microstructure in SPS samples.

- Magnetic and ferroelectric characterizations clearly demonstrate the coexistence of magnetic and ferroelectric ordering in the bulk composite. However, the ferroelectric P-E loops were not well defined. Attempts to quantify ME coupling have not been successful, which could be attributed to the random orientation of the grains where the strain generated from one grain may get cancelled by the others.
2. In the  $\text{CoFe}_2\text{O}_4$  film on PMN-PT substrate system:
- High quality, magnetic  $\text{CoFe}_2\text{O}_4$  thin films were successfully grown on the piezoelectric PMN-PT single crystal substrates. The film epitaxy was confirmed by high-resolution XRD measurements. The out-of-plane lattice parameter of the  $\text{CoFe}_2\text{O}_4$  thin film is smaller than the bulk value which implies the existence of a small residual strain. This is likely caused by the difference in coefficients of thermal expansion between the two materials, the substrate and the film. No secondary phase was detected even after the high temperature deposition process.
  - The saturation magnetization of the  $\text{CoFe}_2\text{O}_4$  thin film is comparable to the bulk value. The residual strain doesn't seem to affect the saturation value but the remnant magnetization and coercivity are lower along the in-plane  $\langle 100 \rangle$  direction. The ferroelectric property of the substrate is well maintained after the film deposition. The large remnant strain induced by external electric field provides the possibility of testing the coupling effect without in-situ electric field.
  - To study the electric-field-control of magnetization, we apply external electric field to pole the PMN-PT substrate. The magnetic domain structure is obtained at different

polarization states of the PMN-PT, i.e., the positive saturation state, the negative depolarized state, the negative saturation state and the positive depolarized state). The cross-sectional view of domains reveals more obvious changes in domain contrast as seen in the MFM images than the plane view setting.

- To confirm and better understand the MFM observations, we also perform macroscopic M-H hysteresis loop measurements under the corresponding strain states of the substrate. Different polarization states of the substrate have negligible effect on the magnetic loops in the out-of-plane x direction while significant changes are observed in the in-plane y direction. The results are all consistent with piezoelectric strain induced anisotropy changes in the  $\text{CoFe}_2\text{O}_4$  film. As the electric field is applied to the PMN-PT substrate, the resulting strain transfers to the  $\text{CoFe}_2\text{O}_4$  film through the epitaxial interface. This strain is superposed on the residual strain and causes reversible changes in the magnetism of the  $\text{CoFe}_2\text{O}_4$ .

Our studies clearly demonstrate the existence of ME coupling in the multiferroic composite systems when the substrate clamping effect is eliminated. This has shed light on the strain mediated ME coupling mechanism in composites systems that have a ferroelectric and a magnetic components with a common interface, and offer valuable information for their potential applications.

Further studies can be directed in the following areas for a better understanding of the multiferroic composites.



1. Direct measurement of the ME coupling effect quantitatively.

We have demonstrated the electric-field-control of magnetism in the multiferroic composite by observing the magnetic domain changes under electric field. However, this technique can not reveal the ME coefficient. Direct measurements of this value, coupled with known materials constant can help us to better understand the strain-mediated ME coupling in composite systems.

2. The converse ME coupling effect in composite systems.

Previous studies on multiferroic systems, including this project, focused on electric field control of magnetism. The converse effect, magnetic field control of electric polarization, has attracted much less attention. However, for a complete understanding of the ME effect in composite systems, it is important that we obtain both coefficients. For such investigations, high quality substrates with large magnetostrictive coefficient will be needed.

In fact, we have fabricated some samples of such multiferroic composite by using commercial Terfenol-D bulk as the substrate and PVDF film as the FE component. Terfenol-D is a well-known magnetostrictive material and PVDF is a ferroelectric polymer that can be processed at low temperatures. In our preliminary study, the PVDF sol gel solution was coated on the polished Terfenol-D substrate surface, followed by drying and annealing in vacuum at 140 °C. We monitored the ferroelectric domain structures using PFM with magnetic field applied to the sample. However, no significant changes in the ferroelectric domains of PVDF were observed. This could be due to the low quality of the

film and interface. Much work is needed in the future. How to maintain the phase and properties of the Terfenol-D during the synthesis of PVDF with good ferroelectric response is the key.

## Reference

- 
- <sup>1</sup> Clark N.A., Lagerwall S.T.(1980).Submicrosecond Bistable Electro-Optic Switching in Liquid-Crystals. *Applied Physics Letters*, 36,899-901.
- <sup>2</sup> Eerenstein W., Mathur N.D., Scott J.F. (2006). Multiferroic and magnetoelectric materials. *Nature*, 442, 759-765.
- <sup>3</sup> Spaldin N.A. and Fiebig M. (2005).The renaissance of magnetoelectric multiferroics. *Science*, 309, 391-392.
- <sup>4</sup> Fiebig, M. (2005). Revival of the magnetoelectric effect. *Journal of Physics D-Applied Physics*, 38, 123-152.
- <sup>5</sup> Ryu J., Carazo A. V., Uchino K., Kim H. (2001). Magnetoelectric properties in piezoelectric and magnetostrictive laminate composites. *Japanese Journal of Applied Physics*. 40, 4948-4851.
- <sup>6</sup> Wang J., Neaton J. B., Zheng H. , Nagarajan V., Ogale S. B., Liu B., Viehland D., Vaithyanathan V., Schlom D. G., Waghmare U. V., Spaldin N. A., Rabe K. M., Wuttig M., and Ramesh R., (2003). Epitaxial BiFeO<sub>3</sub> multiferroic thin film heterostructures .*Science*, 299, 1719-1722.
- <sup>7</sup> Tan, S.Y., Shannigrahi, S. R., Tan, S. H., Tay, F.E.H. (2008). Synthesis and characterization of composite MgFe<sub>2</sub>O<sub>4</sub>/BaTiO<sub>3</sub> multiferroic system, *Journal of Applied Physics*, 103, 094105.
- <sup>8</sup> Liu M., Li X., Imrane H., Chen Y. (2007). Synthesis of ordered arrays of multiferroic NiFe<sub>2</sub>O<sub>4</sub>-Pb(Zr<sub>0.52</sub>Ti<sub>0.48</sub>)O<sub>3</sub> core-shell nanowires, *Applied Physics Letters*, 90, 152501.

- 
- <sup>9</sup> Suchtelen J V.(1972). Product properties: a new application of composite materials. *Philips Research Reports*, 27, 28-37.
- <sup>10</sup> Zhou, J.P., He H., Zhang S., Nan C.W. (2006). Dielectric, magnetic, and magnetoelectric properties of laminated  $\text{PbZr}_{0.52}\text{Ti}_{0.48}\text{O}_3/\text{CoFe}_2\text{O}_4$  composite ceramics. *Journal of Applied Physics*, 100, 094106.
- <sup>11</sup> Zhan S., Nan C. W., Zhang J., Ma J. and Li J.F. (2006). Magnetoelectric properties of multiferroic composites with pseudo-1-3-type structure. *Journal of Applied Physics*, 99, 124108.
- <sup>12</sup> Nagarajan, V., Prasertchoung S., Zhao T. , Zheng H. , Ouyang J. , Ramesh R. , Tian W. , Pan X. Q. , Kim D. M. , Eom C. B., Kohlstedt H. and Waser R. (2004). Size effects in ultrathin epitaxial ferroelectric heterostructures. *Applied Physics Letters*, 84, 5225.
- <sup>13</sup> Ortega, N., Bhattacharya P. , Katiyar R. S. , Dutta P. , Manivannan A. , Seehra M. S. , Takeuchi I. , Majumder S. B. (2006). Multiferroic properties of  $\text{Pb}(\text{Zr,Ti})\text{O}_3/\text{CoFe}_2\text{O}_4$  composite thin films. *Journal of Applied Physics*, 100, 126105.
- <sup>14</sup> Deng CY., Zhang Y., Ma J., Lin YH., and Nan CW., (2007). Magnetic-electric properties of epitaxial multiferroic  $\text{NiFe}_2\text{O}_4\text{--BaTiO}_3$  heterostructure. *Journal of Applied Physics*, 102,074114.
- <sup>15</sup> Li Z.Y., Wang J. G., Wang X. W., Wang Y., Zhu J. S., Wang G. H., Liu J.M. (2007). Magnetoelectric  $\text{CoFe}_2\text{O}_4\text{--Pb}(\text{Zr}_{0.52}\text{Ti}_{0.48})\text{O}_3$  composite films prepared by pulsed-laser deposit method. *Integrated Ferroelectrics*, 87, 33-41.
- <sup>16</sup> Zhang Y., Deng CY., Ma J., Lin YH.,Nan CW. (2008). Enhancement in magnetoelectric response in  $\text{CoFe}_2\text{O}_4\text{--BaTiO}_3$  heterostructure. *Applied Physics Letters*, 92, 062911.

- 
- <sup>17</sup> Deng CY., Zhang Y., Ma J., Lin YH., Nan CW. (2008).Magnetoelectric effect in multiferroic heteroepitaxial BaTiO<sub>3</sub>-NiFe<sub>2</sub>O<sub>4</sub> composite thin films. *Acta Materialia*, 56, 405-412.
- <sup>18</sup> Zheng H., Wang J., Lofland S. E., Ma Z., Mohaddes-Ardabili L., Zhao T., Salamanca-Riba L., Shinde S. R., Ogale S. B. Bai, F., Viehland D., Jia Y., Schlom D. G., Wuttig M., Roytburd A., and Ramesh R., (2004). Multiferroic BaTiO<sub>3</sub>-CoFe<sub>2</sub>O<sub>4</sub> nanostructures. *Science*, 303, 661-663.
- <sup>19</sup> Zheng, H., Wang J.,; Mohaddes-Ardabili L. , Wuttig M., Salamanca-Riba L., Schlom DG., Ramesh R. (2004).Three-dimensional heteroepitaxy in self-assembled BaTiO<sub>3</sub>-CoFe<sub>2</sub>O<sub>4</sub> nanostructures. *Applied Physics Letters*, 85, 2035-2037.
- <sup>20</sup> Li, J., Levin I., Slutsker J., Provenzano V., Schenck P. K., Ramesh R. , Ouyang J. and Roytburd A. L. (2005). Self-assembled multiferroic nanostructures in the CoFe<sub>2</sub>O<sub>4</sub>-PbTiO<sub>3</sub> system. *Applied Physics Letters*, 87, 072909.
- <sup>21</sup> Zheng, H., Zhan Q. Zavaliche F., Sherburne M., Straub F., Cruz MP., Chen LQ., Dahmen U., Ramesh R. (2006). Controlling self-assembled perovskite-spinel nanostructures. *Nano Letters*, 6, 1401-1407.
- <sup>22</sup> Zhan, Q., Yu R. , Crane S.P. , Zheng H. , Kisielowski C. , Ramesh R. (2006). Structure and interface chemistry of perovskite-spinel nanocomposite thin films. *Applied Physics Letters*, 89, 172902.
- <sup>23</sup> Robinson, J.T., Liddle J. A., Minor A., Radmilovic V., Yi D. O., Greaney Alex P., Long K. N., Chrzan D. C., Dubon O. D. (2005). Metal-induced assembly of a semiconductor island lattice: Ge truncated pyramids on Au-patterned Si. *Nano Letters*, 5, 2070.

- 
- <sup>24</sup> Czeschka F. D., Geprägs S., Opel M., Goennenwein S. T. B., Gross R. (2009). Giant magnetic anisotropy changes in  $\text{Sr}_2\text{CrReO}_6$  thin films on  $\text{BaTiO}_3$ , *Applied Physics Letters*, 95, 062508.
- <sup>25</sup> Lou J., Liu M., Reed D., Ren Y., Sun N. X. (2009). Giant Electric Field Tuning of Magnetism in Novel Multiferroic FeGaB/Lead Zinc Niobate–Lead Titanate (PZN-PT) Heterostructures. *Advanced Materials*, 21, 4711-4715.
- <sup>26</sup> Park J. H., Jeong Y. K., Ryu S., Son J. Y., Jang H. M. (2010). Electric-field-control of magnetic remanence of  $\text{NiFe}_2\text{O}_4$  thin film epitaxially grown on  $\text{Pb}(\text{Mg}_{1/3}\text{Nb}_{2/3})\text{O}_3 - \text{PbTiO}_3$ . *Applied Physics Letters*, 96, 192504.
- <sup>27</sup> Eerenstein W., Mathur N. D. and Scott J. F., (2006). Multiferroic and magnetoelectric materials. *Nature*, 442, 759-765.
- <sup>28</sup> Spaldin N. A., Cheong S.W. Ramesh R., (2010). Multiferroics: Past, present, and future, *Physics Today*, 63, 38-44.
- <sup>29</sup> Kopeliovich D., [www.substech.com](http://www.substech.com).
- <sup>30</sup> Sairam K., Sonber J.K., Murthy T.S.R.Ch., Subramanian C., Fotedar R.K., Nanekar P., Hubli R.C. (2014). Influence of spark plasma sintering parameters on densification and mechanical properties of boron carbide, *International Journal of Refractory Metals and Hard Materials*, 42,185-192.
- <sup>31</sup> MUNIR Z.A., ANSELMITAMBURINI U., OHYANAGI M. (2006). The effect of electric field and pressure on the synthesis and consolidation of materials: A review of the spark plasma sintering method, *Journal of Materials Science*, 41, 763–777.
- <sup>32</sup> Available: [http://en.wikipedia.org/wiki/Bragg's\\_law](http://en.wikipedia.org/wiki/Bragg's_law).

- 
- <sup>33</sup> Inaba K., Kobayashi S., Uehara K., Okada A., Reddy S. L., Endo T. (2013). High Resolution X-Ray Diffraction Analyses of (La,Sr)MnO<sub>3</sub>/ZnO/Sapphire(0001) Double Heteroepitaxial Films, *Advances in Materials Physics and Chemistry*, 3, 30348.
- <sup>34</sup> Williams D. B., Carter C. B., (1996). Transmission electron microscopy: a textbook for materials science.
- <sup>35</sup> Mayergoyz I. and Bertotti G. (2005). Hysteresis in Piezoelectric and Ferroelectric Materials, 3.
- <sup>36</sup> Stewart M., Cain M. G. and Hall D. A. (1999). Ferroelectric Hysteresis Measurement & Analysis, *NPL Report CMMT(A)152* .
- <sup>37</sup> Kwei, G.H., Lawson A. C., Billinge S. J. L., Cheong S. W. (1993). Structures of the ferroelectric phases of barium titanate. *Journal of Physical Chemistry*, 97, 2368-2377.
- <sup>38</sup> Zhu, Z.Y., Wang B., Wang H., Zheng Y., Li Q. K. (2007). The first-principles study of ferroelectric behaviours of PbTiO<sub>3</sub>/SrTiO<sub>3</sub> and BaTiO<sub>3</sub>/SrTiO<sub>3</sub> superlattices. *Chinese Physics*, 16, 1780-1785.
- <sup>39</sup> Safari, A., Panda R.K., Janas V.F. (1996). Ferroelectricity: Materials, characteristics & applications. 35-69.
- <sup>40</sup> Jang, J.W., Chung S. J., Cho W. J., Hahn T. S., Choi S. S. (1997). Thickness dependence of room temperature permittivity of polycrystalline BaTiO<sub>3</sub> thin films by radio-frequency magnetron sputtering. *Journal of Applied Physics*, 81, 6322-6327.
- <sup>41</sup> Ken, M.R. and L.K. Karen, (2003). Substrate effects on the ferroelectric properties of fine-grained BaTiO<sub>3</sub> films. *Journal of Applied Physics*, 94, 5982-5989.
- <sup>42</sup> Viswanathan, B., Murthy V. R. K. (1990). *Ferrite Materials*.

- 
- <sup>43</sup> Huang, W., Zhou L. X., Zeng H. Z., Wei X. H., Zhu J., Zhang Y., Li Y.R. (2007). Epitaxial growth of the CoFe<sub>2</sub>O<sub>4</sub> film on SrTiO<sub>3</sub> and its characterization. *Journal of Crystal Growth*, 300, 426-430.
- <sup>44</sup> Lisfi, A., Williams C.M., (2003). Magnetic anisotropy and domain structure in epitaxial CoFe<sub>2</sub>O<sub>4</sub> thin films. *Journal of Applied Physics*, 93, 8143-8145.
- <sup>45</sup> Li, Y.W., Hu Z. G., Yue F. Y., Yang P. X., Qian Y. N., Cheng W. J., Ma X. M., Chu J. H.(2008). Oxygen-vacancy-related dielectric relaxation in BiFeO<sub>3</sub> films grown by pulsed laser deposition. *Journal of Physics D-Applied Physics*, 41, 215403.
- <sup>46</sup> Liao M., Zhong X. L., Wang J.B., Zhou Y. C, Liao H. (2008). Effects of CoFe<sub>2</sub>O<sub>4</sub> content on the properties of nanoparticulate Bi<sub>3.15</sub>Nd<sub>0.85</sub>Ti<sub>3</sub>O<sub>12</sub>–CoFe<sub>2</sub>O<sub>4</sub> thin films. *Scripta Materialia*, 58, 715-718.
- <sup>47</sup> Martin L. W., Crane S. P., Chu Y. H., Holcomb M. B., Gajek M., Huijben M., Yang C. H., Balke N., Ramesh R. (2008). Multiferroics and magnetoelectrics: thin films and nanostructures. *Journal of Physics: Condensed Matter*, 20, 434220.
- <sup>48</sup> Lefki K., Dormans G. J. M. (1994). Measurement of piezoelectric coefficients of ferroelectric thin films. *Journal of Applied Physics*, 76, 1764-1769.
- <sup>49</sup> Park J. H., Shin H. H., Jang H. M. (2008). Quasi-intrinsic magnetoelectric coupling in multiferroic nanocomposite thin films. *Physical Review B*, 77, 212409.
- <sup>50</sup> Dix N., Muralidharan R., Warot-Fonrose B., Varela M., Snchez F., Fontcuberta J. (2009). On the strain coupling across vertical interfaces of switchable BiFeO<sub>3</sub>–CoFe<sub>2</sub>O<sub>4</sub> multiferroic nanostructures. *Applied Physics Letters*, 95, 062907.



- 
- <sup>51</sup> W. Eerenstein, M. Wiora, J. L. Prieto, J. F. Scott, and N. D. Mathur, (2007). Giant sharp and persistent converse magnetoelectric effects in multiferroic epitaxial heterostructures. *Nature Mater.* 6, 348-351.
- <sup>52</sup> Park J. H., Jeong Y. K., Ryu S., Son J. Y., Jang H. M. (2010). Electric-field-control of magnetic remanence of  $\text{NiFe}_2\text{O}_4$  thin film epitaxially grown on  $\text{Pb}(\text{Mg}_{1/3}\text{Nb}_{2/3})\text{O}_3 - \text{PbTiO}_3$ . *Applied Physics Letters*, 96, 192504.
- <sup>53</sup> Yang J. J., Zhao Y. G., Tian H. F., Luo L. B., Zhang H. Y., He Y. J., Luo H. S. (2009). Electric field manipulation of magnetization at room temperature in multiferroic  $\text{CoFe}_2\text{O}_4/\text{Pb}(\text{Mg}_{1/3}\text{Nb}_{2/3})_{0.7}\text{Ti}_{0.3}\text{O}_3$  heterostructures. *Applied Physics Letters*, 94, 212504.
- <sup>54</sup> Thiele C., Dör K., Bilani O., Rödel J., Schultz L. (2007). Influence of strain on the magnetization and magnetoelectric effect in  $\text{La}_{0.7}\text{A}_{0.3}\text{MnO}_3/\text{PMN-PT}(001)$  ( $\text{A}=\text{Sr}, \text{Ca}$ ) . *Physics Review B*, 75, 054408.
- <sup>55</sup> Liu M., Obi O., Lou J., Stoute S., Cai Z., Ziemer K., Sun N. X. (2009). Strong magnetoelectric coupling in ferrite/ferroelectric multiferroic heterostructures derived by low temperature spin-spray deposition. *Journal of Physics D: Applied Physics*, 42, 045007.
- <sup>56</sup> Taniyama T., Akasaka K., Fu D., Itoh M. (2009). Artificially controlled magnetic domain structures in ferromagnetic dots/ferroelectric heterostructures. *Journal of Applied Physics*. 105, 07D901.
- <sup>57</sup> Zhang S., Zhao Y. G., Li P. S., Yang J. J., Rizwan S., Zhang J. X., Seidel J., Qu T. L., Yang Y. J., Luo Z. L., He Q., Zou T., Chen Q. P., Wang J.W., Yang L. F., Sun Y., Wu Y. Z., Xiao X., Jin X. F., Huang J., Gao C., Han X. F., Ramesh R. (2012). Electric-Field Control of Nonvolatile Magnetization  $\text{Co}_{40}\text{Fe}_{40}\text{B}_{20}/\text{Pb}(\text{Mg}_{1/3}\text{Nb}_{2/3})_{0.7}\text{Ti}_{0.3}\text{O}_3$  Structure at Room Temperature. *Physical Review Letters*, 108, 137203.

- 
- <sup>58</sup> Liu M., Obi O., Lou J., Chen Y., Cai Z., Stoute S., Espanol M., Lew M., Situ X., Ziemer K. S., Harris V. G., Sun N. X. (2009). Giant Electric Field Tuning of Magnetic Properties in Multiferroic Ferrite/Ferroelectric Heterostructures, *Advanced Functional Materials*, 19, 1826–1831.
- <sup>59</sup> Srinivasan G., De Vreugd C. P., Bichurin M. I., Petrov V. M. (2005). Magnetoelectric interactions in bilayers of yttrium iron garnet and lead magnesium niobate-lead titanate: Evidence for strong coupling in single crystals and epitaxial films. *Applied Physics Letters*, 86, 222506.
- <sup>60</sup> Kim J., Ravindranath V., Shin S. (2007). Effect of an electric field-induced stress on the magnetic properties of amorphous Terfenol-D films deposited on PMN-PT single crystal substrates. *Physica Status Solidi (a)*, 204, 4202-4205.
- <sup>61</sup> Geprags S., Brandlmaier A., Opel M., Gross R., Goennenwein S. T. B. (2010), Electric field controlled manipulation of the magnetization in Ni/BaTiO<sub>3</sub> hybrid structures. *Applied Physics Letters*, 96, 142509.
- <sup>62</sup> Wang P., Luo H., Pan X., Li D., Yin Z. (2001). Dielectric and piezoelectric properties of PMN-PT single crystals grown by Bridgman method, *In: 12th IEEE International Symposium on Applications of Ferroelectrics*, 2, 537-541.
- <sup>63</sup> Noheda B., Cox D. E., Shirane G. (2002). Phase diagram of the ferroelectric-relaxor (1-x)PbMg<sub>1/3</sub>Nb<sub>2/3</sub>O<sub>3</sub>-xPbTiO<sub>3</sub>. *Physics Review B*, 66, 054104.
- <sup>64</sup> Bai F., Li J., Viehland D. (2004). Domain hierarchy in annealed (001)-oriented Pb (Mg<sub>1/3</sub>Nb<sub>2/3</sub>) O<sub>3</sub> - x% PbTiO<sub>3</sub> single crystals, *Applied Physics Letters*, 85, 2313.

- 
- <sup>65</sup> Thang P. D., Rijnders G., Blank D. H. A. (2007). Stress-induced magnetic anisotropy of CoFe<sub>2</sub>O<sub>4</sub> thin films using pulsed laser deposition. *Journal of Magnetism and Magnetic Materials*, 310, 2621–2623.
- <sup>66</sup> Jiang X., Tang F., Wang J. T., Chen T.P. (2001). Growth and properties of PMN–PT single crystals. *Physica C: Superconductivity*, 364, 678–685.
- <sup>67</sup> Axelsson A. K., Aguesse F., Spillane L., Valant M., McComb D.W., Alford N. M. (2011). Quantitative strain analysis and growth mode of pulsed laser deposited epitaxial CoFe<sub>2</sub>O<sub>4</sub> thin films. *Acta Materialia*, 59, 514–520.
- <sup>68</sup> Bi Z. H., Zhu J. H., Batey J. L. (2010). CoFe<sub>2</sub>O<sub>4</sub> spinel protection coating thermally converted from the electroplated Co–Fe alloy for solid oxide fuel cell interconnect application. *Journal of Power Sources*, 195, 3605–3611.
- <sup>69</sup> Tang Y., Chen L., Zhao X., Jin W., Luo H., (2006). Anisotropic thermal expansion and phase transitions in Pb(Mg<sub>1/3</sub>Nb<sub>2/3</sub>)O<sub>3</sub>-0.3PbTiO<sub>3</sub> single crystals, *Physica B*, 382, 205–208.